

Fundamental Study on Polymer Flocculation Behavior in Saline Solutions

by

Shanshan Wang

A thesis submitted in partial fulfillment of the requirements for the degree of

Master of Science

In

Materials Engineering

Department of Chemical and Materials Engineering

University of Alberta

© Shanshan Wang, 2014

Abstract

In this work, the influence of solution salinity on settling performance of both commercial polymeric flocculant Magnafloc 1011(MF) and synthesized polymer flocculant Chitosan-graft-Polyacrylamide (chi-g-PAM) was systematically investigated. The effect of MgCl_2 on the settling performance of MF was carried out on a model clay (i.e. kaolinite). High concentration of Mg^{2+} was found to increase the initial settling rate (ISR) and decrease the supernatant turbidity. Surface forces apparatus (SFA) and quartz crystal microbalance with dissipation (QCM-D) were applied to investigate the molecular and surface interactions of kaolinite particles and polymer, which suggested that the better settling behaviors in MgCl_2 solutions as compared to that in Milli-Q water was mainly due to the different polymer-particle interactions and polymer conformations. Chitosan-grafted-Polyacrylamide (chi-g-PAM) was successfully synthesized and characterized. For the flocculation of chi-g-PAM on kaolinite suspensions, high concentrations of NaCl and CaCl_2 reduce the ISR but lead to clear supernatant as compared to that in Milli-Q water. The complementary measurements by zeta potential analyzer, QCM-D, SFA and atomic force microscopy (AFM) demonstrate that high solution salinity conditions can affect the surface charge property of kaolinite particles and polymer configuration, therefore weaken the polymer-particle interaction and polymer adsorption, resulting in poor chi-g-PAM flocculation performance.

Acknowledgement

I want to convey my sincere gratitude to my supervisors, Dr. Hongbo Zeng and Dr. Qingxia (Chad) Liu for their guidance and support for my research study and life in University of Alberta.

I want to give my special thanks to Dr. Hongbo Zeng for each advice, criticism, and encouragement on experiment design, data analysis, paper writing and presenting. Without those, I could not grow from a green hand to a qualified research student. Research experience in Dr. Zeng's group will be my precious memory in my life.

With great industry experience and research knowledge, Dr. Chad Liu inspired me with creative ideas about tailing project. As a responsible supervisor, he treated my safety in lab as the most important in every situation. I was deeply impressed by his careful and rigorous attitude toward research and work.

I am also thankful for the kind help from my group members. Dr. Bin is expert in polymer science and I benefited a lot from the valuable suggestions from him about my project. Yaguan, Ling and Jun helped me with SFA experiments and project design. Without your help, I can't accomplish all the work in my project.

Finally, I want to give my greatest thanks to my mother and father for raising me up and supporting me no matter what happens. Besides, my endless love goes to my boyfriend, An, who companied with me during my hardest time and encouraged me to be strong.

Table of Content

Chapter 1 Introduction	1
1.1 Saline water application in mineral processing	1
1.2 Tailings management in saline water	3
1.3 Coagulation and flocculation.....	4
1.4 Flocculants and surface interactions.....	6
1.4.1 Flocculants types	6
1.4.2 Surface interactions: Hydrogen bonding.....	7
1.4.3 Surface interactions: Van der Waals force.....	8
1.4.4 Surface interactions: Electrostatic force and electrostatic double layer...	9
1.4.5 Other interactions: Steric repulsion and bridging effect	12
Chapter 2 Experimental Techniques	14
2.1 Quartz crystal microbalance with dissipation monitoring (QCM-D).....	14
2.1.1 Introduction of QCM-D	14
2.1.2 Working principle of QCM-D.....	15
2.2 Surface force apparatus (SFA)	17
2.2.1 Development of surface force apparatus.....	17
2.2.2 Multiple beam interferometry (MBI) technique.....	21

2.2.3 Surface force measurement using the SFA	22
2.3 Zetasizer Nano	24
2.3.1 General introduction of Zetasizer Nano	24
2.3.2 Zeta potential measurement	25
2.3.3 Dynamic light scattering (DLS)	26
2.3.4 Molecular weight measurement	27
2.4 Electron beam evaporation system #1 (Gomez)	28
2.5 Atomic force microscopy	29
Chapter 3 The study of MgCl₂'s Effect on Enhancing Magnafloc 1011 Flocculation on the Model Clay	31
3.1 Introduction	31
3.2 Materials and experimental methods	34
3.2.1 Materials	34
3.2.2 Settling test	35
3.2.3 Surface force measurement	36
3.2.4 Measurement of the hydrodynamic radii of the MF in salt solutions	39
3.2.5 Adsorption measurement of the MF on the model clay surfaces using QCM-D	39
3.3 Results and discussion	40

3.3.1 Evaluation of MF settling performance on kaolinite suspension in MgCl ₂ solutions.....	40
3.3.2 Interactions between MF and model clay surfaces measured by SFA... 45	
3.3.3 Conformation measurements by the dynamic light scattering (DLS)... 51	
3.3.4 Adsorption of MF on model clay surface measured by QCM-D..... 53	
3.3.5 The mechanism of interactions between MF and model clay particle (surface)..... 58	
3.4 Conclusion..... 61	
Chapter 4 Molecular and Surface Interactions between Chitosan-g-Polyacrylamide Polymer Flocculant and Kaolinite Particles: Impact of Salinity..... 63	
4.1 Introduction..... 63	
4.2 Materials and Methods..... 66	
4.2.1 Materials..... 66	
4.2.2 Synthesis of chi-g-PAM..... 67	
4.2.3 Polymer characterization..... 67	
4.2.4 Flocculation experiments..... 68	
4.2.5 Polymer adsorption test by QCM-D..... 69	
4.2.6 Surface force measurements in aqueous solutions by SFA..... 70	
4.2.7 AFM imaging..... 71	

4.3 Results and Discussion	71
4.3.1 Characterization of chi-g-PAM.....	71
4.3.2 Settling tests using chi-g-PAM	76
4.3.3 Zeta potential of kaolinite particles in suspension	79
4.3.4 QCM-D Study on chi-g-PAM adsorption.....	81
4.3.5 Surface force measurements.....	88
4.3.6 The morphology of chi-g-PAM adsorption on mica.....	91
4.3.7 Interaction model between chi-g-PAM and kaolinite particles.....	92
4.4 Conclusions	95
Chapter 5 Summary and Future work.....	97
5.1 Summary.....	97
5.2 Future work	99
5.2.1 MF 1011 flocculation future study.....	99
5.2.2 Chi-g-PAM flocculation future study	100
References.....	102

List of Tables

Table 1.1. Major earth surface water resource ¹	1
Table 1.2. Salt concentration of saline tailings samples	4
Table 1.3. Proposed size classification	5
Table 1.4. Classification of inorganic and organic polymers	7
Table 2.1. Zetasizer Nano models and measurement specifications	25
Table 3.1. Properties of Magnafloc 1011	34
Table 3.2. Key parameters of force-distance profil results	50
Table 3.3. Hydrodynamic radii of MF in solutions of different MgCl ₂ concentration.....	53

List of Figures

Figure 1.1. PAM force measurement by AFM device.....	8
Figure 1.2. Schematic of electrostatic double layers of a negative charged particle surface.	12
Figure 1.3. The schematic of adsorbed polymer chains in solution.	13
Figure 2.1. The schematic of QCM-D setup.....	15
Figure 2.2. The schematic of sensor crystal structure.	16
Figure 2.3. The layers built-up of the silica and alumina sensors.	17
Figure 2.4. The schematic of SFA 2000 main components.....	19
Figure 2.5. The schematic of the SFA setup.....	20
Figure 2.6. A typical FECO of two back-silvered mica sheets in contact in air.	20
Figure 2.7. Force-distance profile in normal force measurement.....	24
Figure 2.8. The schematic of a typical zeta potential measurement cell.	26
Figure 2.9. Light intensity fluctuation of two samples: larger particles (top) and smaller particles (bottom).....	27
Figure 2.10. Weight averaged molecular weight (Mw) measurement procedure by SLS technique.....	28
Figure 2.11. Electron beam evaporation system.....	29
Figure 2.12. Schematic of AFM imaging mechanism.....	30
Figure 3.1. The schematic of the settling test procedure	36
Figure 3.2. The schematic of the setup of SFA 2000.	38

Figure 3.3. The initial settling rate of 5 wt% kaolinite suspension as a function of MF dosage at pH 7.5 prepared by Milli-Q water (▼), 0.01 M (■), 0.1 M (●) and 1 M (▲) MgCl ₂ solutions.	41
Figure 3.4. The turbidity of the supernatant of 5 wt% solid kaolinite suspension prepared with 0.01 M (■), 0.1 M (●) and 1 M (▲) MgCl ₂ solutions after 18 hrs-settling versus MF dosage at pH 7.5.....	43
Figure 3.5. Settling images of the kaolinite suspensions prepared in Milli-Q water (left) and 0.01 M MgCl ₂ solution (right) with different MF dosages: A 25 ppm; B 50 ppm; C 75 ppm; D 100 ppm after 18 hrs-settling at pH 7.5.	43
Figure 3.6. The zeta potential values of kaolinite particles in the supernatant of 5 wt% solid kaolinite suspension prepared with 0.01 M (■), 0.1 M (●) and 1 M (▲)MgCl ₂ solution after 18 hrs-settling at pH 7.5 as a function of MF dosage.	44
Figure 3.7. The normalized force-distance profiles between two mica surfaces in 5 ppm MF prepared by (a) Milli-Q water, (b) 0.01 M MgCl ₂ ; (c) 0.1 M MgCl ₂ and (d) 1 M MgCl ₂ after 30 min incubation at pH 7.5.	47
Figure 3.8. The normalized force-distance profiles between two alumina surfaces in 5 ppm MF prepared by (a) Milli-Q water; (b) 0.01 M; (c) 0.1 M and (d) 1 M MgCl ₂ after 30 min incubation at pH 7.5.....	49
Figure 3.9. Adhesion energy between mica surfaces and alumina surfaces in MF solution in the presence of 0.01 M, 0.1 M and 1 M MgCl ₂ solutions.....	51

Figure 3.10. Time course of Δf and ΔD for the MF adsorption on silica sensor in Milli-Q water.	54
Figure 3.11. Time course of Δf and ΔD for the MF adsorption on silica sensor in 0.01 M $MgCl_2$	54
Figure 3.12. Time course of Δf and ΔD for the MF adsorption on silica sensor in 0.1 M $MgCl_2$	55
Figure 3.13. Time course of Δf and ΔD for the MF adsorption on silica sensor in 1 M $MgCl_2$	55
Figure 3.14. Time course of Δf and ΔD for the MF adsorption on alumina sensor in Milli-Q water.	56
Figure 3.15. Time course of Δf and ΔD for the MF adsorption on alumina sensor in 0.01 M $MgCl_2$	57
Figure 3.16. Time course of Δf and ΔD for the MF adsorption on alumina sensor in 0.1 M $MgCl_2$	57
Figure 3.17. Time course of Δf and ΔD for the MF adsorption on alumina sensor in 1 M $MgCl_2$	58
Figure 3.18. Schematic of the interaction of MF with silica and alumina surfaces in Milli-Q and $MgCl_2$ solution.	61
Figure 4.1. The schematic of polymerization process of chi-g-PAM.....	73
Figure 4.2. FTIR Spectra of (A) chitosan, (B) chi-g-PAM, and (C) PAM.....	74

Figure 4.3. Pictures on the stability of the solutions of (a) chi-g-PAM, (b) chitosan and (c) chitosan & PAM mixture under various pH conditions: (A) pH 5, (B) pH 7, (C) pH 8, (D) pH 9, and (E) pH 11..... 76

Figure 4.4. ISR for the settling of 5 wt % kaolinite suspension under different dosages of chi-g-PAM in Milli-Q water (■), 0.01 M (▲), 0.1 M (▼) and 1 M (●) of NaCl (left) and CaCl₂ (right) solutions at pH ~7.0 78

Figure 4.5. Turbidity of kaolinite suspension supernatant after settling 18 hrs at pH ~7.0 in Milli-Q water (■), 0.01 M (▲), 0.1 M (▼) and 1 M (●) NaCl (left) and CaCl₂ (right) solutions. 79

Figure 4.6. Zeta potential of kaolinite particles in the suspension supernatant after settling for 18 hrs at pH ~7.0 in Milli-Q water (■), 0.01 M (▲), 0.1 M (▼) and 1 M (●) NaCl (left) and CaCl₂ (right) solutions. 80

Figure 4.7. Change of frequency Δf and dissipation ΔD associated with the adsorption of chi-g-PAM on QCM-D silica sensors in Milli-Q water and saline solutions at pH ~7.0: (a) Milli-Q water, (b) 0.01 M NaCl, (c) 0.1 M NaCl and (d) 1 M NaCl. 83

Figure 4.8. Change of frequency Δf and dissipation ΔD associated with the adsorption of chi-g-PAM on QCM-D silica sensors in saline solutions at pH ~7.0: (a) 0.01 M CaCl₂, (b) 0.1 M CaCl₂, (c) 1 M CaCl₂. (d) Mass of polymer layer adsorbed on silica sensors under various solution conditions. 84

Figure 4.9. Change of frequency Δf and dissipation ΔD associated with the adsorption of chi-g-PAM on QCM-D silica sensors in Milli-Q water and saline solutions at

pH ~7.0: (a) Milli-Q water, (b) 0.01 M NaCl, (c) 0.1 M NaCl and (d) 1 M NaCl..... 87

Figure 4.10. Change of frequency Δf and dissipation ΔD associated with the adsorption of chi-g-PAM on QCM-D alumina sensors in saline solutions at pH ~7.0: (a) 0.01 M CaCl₂, (b) 0.1 M CaCl₂, (c) 1 M CaCl₂. (d) Mass of polymer layer adsorbed on alumina sensors under various solution conditions. 88

Figure 4.11. Typical force-distance profiles between mica surfaces in 5 ppm chi-g-PAM solutions at pH ~7.0 in: (a) Milli-Q water, (b) 1 M NaCl, (c) 1 M CaCl₂ and (d) adhesion force result. 91

Figure 4.12. Topographic AFM images of 50 ppm chi-g-PAM adsorbed on mica substrates in (a) Milli-Q water, (b) 1 M NaCl and (c) 1 M CaCl₂. The images were taken on dried samples in air. 92

Figure 4.13. Schematic of chi-g-PAM structure after grafting polymerization. 93

Figure 4.14. Proposed interaction model of chi-g-PAM and negatively charged kaolinite particle surfaces in: (a) Milli-Q water, and (b) salt solutions. (c) Illustration of symbols..... 95

List of Acronyms

AC	Alternating current
AFM	Atomic force microscope
CD	Charge density
Chi-g-PAM	Chitosan-grafted polyacrylamide
DLS	Dynamic light scattering
DLVO	Derjaguin and Landau and Verwey and Overbeek
FECO	Fringes of Equal Chromatic Order
FTIR	Fourier transform infrared
H-PAM	Hydrolyzed polyacrylamide
ISR	Initial settling rate
MBI	Multiple beam interference
MF	Magnafloc
M _w	Molecular weight
NTU	Nephelometric turbidity units
PAA	Polyacrylic acid

PAM	Polyacrylamide
PB	<i>Poisson-Boltzmann</i>
PEO	Polyethylene Oxide
PVP	Polyvinyl pyridine
QCM-D	Quartz crystal microbalance with dissipation monitoring
SFA	Surface force apparatus
VDW	Van der Waals

List of Symbols

A	Hamaker constance, J
C	Coefficient in the atom-atom pair potential
c	Concentration
$\Delta D_{applied}$	Distance that moved by micrometers, m
ΔD_{means}	Actual distance, m
ΔD_{jump}	Jump distance, m
ε_0	Permittivity of the vacuum, F/m
ε_r	Relative permittivity
Δf	Frequency change
ψ	Electrostatic potential, mV
ζ	Zeta-potential, mV
n	Resonance number of the sensor
K	Optical constant
k	Spring constant, N/m

k_B	Boltzmann constant
κ	Debye parameter, m^{-1}
κ^{-1}	Debye length, m
H	Liquid dynamic viscosity, Pa·s
P	Bulk/surface density
R, r	Radius of spherical particle, m
R_θ	Rayleigh ratio
R_g	Radius of gyration, m
R_H	Hydrodynamic radius, m
S	Distance, m
T	Absolute temperature, K
M	Medium refractive index
μ_{mica}	Mica refractive index
X	Gap between the point and surface, m
Z	Ion valency

Chapter 1 Introduction

1.1 Saline water application in mineral processing

Water plays a critical role in economy and industry development. The growing demand for water usage in the following years cannot be fully satisfied due to the limited water supplies. The serious water pollution and contamination problems put the situation even worse. The main water resources on earth surface are shown in Table 1.1. From the table, it clearly shows that 96.5% of the water resource is in the oceans and only 2.5% is fresh water.

Table 1.1. Major earth surface water resource¹

Water Recourse	Percent of Total Water (%)	Mean Residence Time of Water
Oceans, seas, bays	96.5	2500 years
Ice caps, glaciers	1.74	9700 years
Groundwater (Fresh)	0.76	1400 years
Groundwater (Saline)	0.93	1400 years
Ground ice and permafrost	0.022	10000 years
Lake (Fresh)	0.007	17 years
Lake (Saline)	0.007	17 years
Atmosphere	0.001	8 days
Swamps	0.0008	5 days
Rivers	0.0002	16 days
Biological water	0.0001	4 hours

Totals	100	—
--------	-----	---

Usually, for mineral industry, some mining ores located even in remote places which have less access to fresh water. To solve the water scarcity problem, seawater has been considered as an alternative in mineral processing industry. Meanwhile, by using recycled processing water (seawater or fresh water), electrolytes were found to accumulate in closed water circuits in flotation plants (flotation paper). However, the influence of saline water chemical properties, e.g. ionic strength in mineral processing application is still under research.

Technically, it is possible to desalinate saline water into fresh water for mineral processing. In 2009, it was reported the ‘reverse osmosis technique’ could turn sea water into drinking water.² However, it brings two major problems: (1) it will highly increase the cost for obtaining the processing water; (2) large amount of high concentration salt solutions may cause environment pollutions^{3,4}. Actually, it is not necessary to get rid of saline water, actually, it has been found that electrolyte in processing water is found to help with particle-bubble attachment in mineral flotation process⁵. But the chemistry composition of saline water is complicated and the influence of each single component (such as Na^+ or Ca^{2+}) on particle-particle interaction is still under investigation. Besides, saline water was also found helpful in mineral flotation.⁶ The research on salinity in flotation under various conditions is still carrying on.

1.2 Tailings management in saline water

Tailings, as the materials left over after separation, sorting in mineral processing, often contain large amount of fine particles.⁷ Those fine particles are so stable in water that it will take decades for them to settle down. Thus tailings are often transported as the form of slurry with large water content.

The tailings slurry is then pumped to the tailings impoundment area and water is recycled back to the plant. In order to shorten the recycle span of processing water and retrench the impoundment area, many methods have been taken to improve the dewatering efficiency. Adding flocculant is found effective an effective method in solid-liquid separation,⁸ but flocculation in saline water increases the complexity of the system. In the sample of saline tailings, the amount of Na^+ , Mg^{2+} , K^+ and Ca^{2+} is quite significant compared to the sample in fresh water tailings (Table 1.2). The metal ions can influence the particle's surface properties and change the interaction mechanisms between flocculant and particles. But up till now, less fundamental research has been done on flocculant-particles interactions in saline solutions.

Table 1.2. Salt concentration of saline tailings samples.

Sample ions	Vancouver sea water (ppm)	Saline tailings measured (ppm)	Supernatant of saline tailings (ppm)	Supernatant of prepared fresh water tailings (ppm)
Na	6367	4900	5832	141
Mg	997	987	701	7.87
K	297	350	275	12.5
Ca	632	750	679	11.4

1.3 Coagulation and flocculation

In mineral tailings, without any treatment, it takes decades for fine tailings to settle.⁹ Fine particle (size <4.4 μ m) is one of the serious problems in tailings treatment. Usually, it carries negative charge and has high surface area.¹⁰ Due to the small mass, it is difficult for particles to overcome the energy barrier in between, which leads to the stable particles suspension. Because of high surface area, it disperses homogeneously and fast in water and can adsorb large amount of chemicals. In 1985, Sivamohan and Forssberg proposed the classification of particles size which has been shown in Table 1.3.

10

Table 1.3. Proposed size classification.

Classification	Size
Super colloids	< 0.2 μm
Colloids	< 1 μm
Ultrafines	< 5 μm
Very fines	< 20 μm
Fines	< 100 μm
Intermediates	< 500 μm
Coarse	\geq 500 μm

According to the table, we find that size of fine particles in tailings are closed to the colloids. To better understand the properties of the suspended fine particles, colloidal system is often used as the model to study the interaction between particles in solution. In order to break the stable particle suspension state, some chemicals are added to change the surface properties of the colloidal particles, and then particles can form aggregates. Usually, coagulation and flocculation are used to describe the destabilisation process.¹¹ Coagulation and flocculation are sometimes considered synonymously in certain conditions but there exists some differences between them.

In coagulation, a chemical agent with opposite charge was added to cause charge neutralisation with suspended particles, which disturbs stable colloidal system. When those particles are neutralized, it is easier for them to stick together. In coagulation, the structure of agglomerates is spongy with compact but loosely bounds. Coagulation is usually the first step in mineral wastewater treatment.

Flocculation usually refers to the situation that when high MW polymer flocculant forms bridges or adsorbs on particles surfaces through collision. In this mechanism, segments of the polymer are bound to one particle, at the same time, loops and free chains extend into solution and attach to neighbouring particles, which increases in the size of the aggregated flocs. To avoid breaking aggregates, flocculants are usually mixed with colloidal particles gently. By sedimentation or filtration, flocs can be separated with suspension.

1.4 Flocculants and surface interactions

1.4.1 Flocculants types

According to different chemical properties, flocculants can be divided into inorganic and organic flocculants. For the inorganic flocculant, aluminium and ferric salts are commonly used.¹² But due to its limited application in industry, the organic flocculant find its stage nowadays in various areas and polymer is the most widely used organic flocculants in wastewater treatment¹³, mineral tailings settlement¹⁴, paper making¹⁵ and etc.. Compared to the inorganic flocculant, the polymeric flocculant shows the following major advantages: (1) Polymer flocculant can be further modified according to the properties of different colloid suspension;¹² (2) It can effectively separate fine particles with water by forming larger and stronger bridging flocs. According to the polymer charge property, polymeric flocculants can be further classified into three groups: anionic, cationic and non-ionic flocculants (shown in Table 1.4).

Table 1.4. Classification of inorganic and organic polymers.

Flocculants type		Examples
Inorganic flocculants		Al, Fe salt
Organic flocculants	Anionic	Hydrolyzed polyacrylamide (H-PAM); Polyacrylic acid (PAA)
	Cationic	Chitosan, Polyvinyl pyridine (PVP)
	Non-ionic	Polyacrylamide (PAM), Polyethylene Oxide (PEO)

For the polymer flocculant, the molecular weight (Mw) and the charge density (CD) (in the case of polyelectrolytes) are essential characteristics to the flocculation performance. Typical MW ranges from several thousands to millions Da. Usually, polymer with high MW always has large effective size in solution. For polyelectrolytes, CD is determined by the proportion of ionized segments on the polymer chain. The ionization degree depends on both segment type and solution pH.¹⁶

1.4.2 Surface interactions: Hydrogen bonding

In polymer-aid flocculation, colloidal particles stability or aggregation is normally related to polymer adsorption and polymer layer structures changing on the particle surfaces.^{17, 18} Studying the surface interactions between polymer chains and particles surfaces is essential in order to understand the polymer attachment properties. These intermolecular and surface forces include, hydrogen bonding, van der Waals force, electrostatic force, etc..

Hydrogen bonding is a kind of electromagnetic attraction between polar molecules, ranging from the very strong, comparable with covalent bonds, to the very weak, comparable with van der Waals forces.¹⁹ The size of electron-depleted *H* atom is very

small, and other electronegative atoms X (O^- , N^- and F^-) can bond with H and form the $X^- - H^+$ groups, thus hydrogen bond is depicted by $-X^- \cdots H^+$. It is often used to explain the uncharged polymer flocculants adsorption on particles surfaces, such as polyacrylamide (PAM). In 2002, the force of single PAM molecule adsorption on mica was measured by AFM (shown in Figure 1.1) and it was found that hydrogen bonding was the main reason that caused PAM adsorbing on silicate surface.²⁰

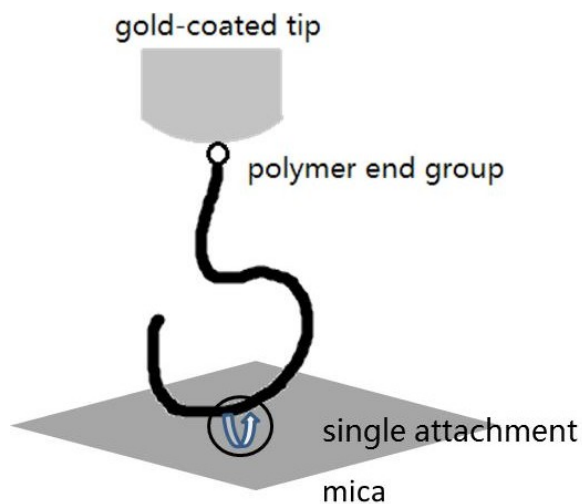


Figure 1.1. PAM force measurement by AFM device.

1.4.3 Surface interactions: Van der Waals force

Van der Waals (VDW) force, which is named after Dutch scientist Johannes Diderik van der Waals, is the sum of the attractive or repulsive forces between molecules (dipoles) or between parts of the same molecule²¹. VDW interactions include three kinds of contributions: dipole-dipole interactions (Keesom force), dipole-induced dipole interactions (Debye force) and instantaneous induced dipole-induced dipole interactions (London dispersion force). It is believed that VDW forces exist between all atoms and

molecules. It is not as strong as ionic bonds and covalent bonds and the magnitude of VDW forces decrease dramatically as the distance (D) between surfaces increases. For example, VDW force between two atoms is proportional to $-D^{-7}$. The VDW interactions depend on the geometries of interacting surfaces as well. For two flat parallel surfaces, separated by a distance of D , the VDW forces full expression is

$$F = -\frac{A}{6\pi D^3} \quad (1.1)$$

where A is a constant for a given substance, called the Hamaker constant which is defined as $A = \pi^2 C \rho_1 \rho_2$,²² C is the coefficient in the atom-atom pair potential and ρ_1 and ρ_2 are the numbers of atoms per unit volume in the two bodies. For two spherical particles, the VDW forces can be expressed as

$$F = -\frac{AR_1R_2}{6(R_1 + R_2)D^2} \quad (1.2)$$

where R_1 and R_2 are the radii of the two spherical particles

1.4.4 Surface interactions: Electrostatic force and electrostatic double layer

Electrostatic force is always considered in electrolytes flocculation situation. Usually, electrostatic attraction exists between charged polymer segments and opposite charged particle surfaces and it is extremely important in facilitating adsorption of polyelectrolytes.²³ Sometimes, the electrostatic repulsion between the same charged segments of polymer could lead to a more stretched polymer structure in solutions. Whereas, in high salinity solutions, the electrostatic repulsion can be screened due to the

combination between charged segments and the free salt ions in solutions, thus thicker polymer layer can be found on the surfaces.²⁴

However, interactions between two charged surfaces in electrolyte solutions are much more complicated. In this system, the charge surface is usually covered with cloud of ions and the structure is called *electrostatic double layer* (EDL) whose schematic is shown in Figure 1.2. The surface charge creates an electrostatic field and the surface charge is balanced by the equal opposite charged ions net. A layer of the immobile counter ions are adsorbed on the charged particle surface and the electric potential decreases linearly as the distance increases within the so-called *Stern layer* regime. However, some other mobile counter ions diffuse and form an atmosphere closed to the surface, which is known as *Diffuse layer*. In this layer, counter ions obey *Poisson-Boltzmann* (PB) distribution:

$$\frac{d^2\psi}{dx^2} = -\frac{ze\rho}{\varepsilon_0\varepsilon} = -\frac{ze\rho_0}{\varepsilon_0\varepsilon} e^{-\frac{ze\psi}{kT}} \quad (1.3)$$

where ψ is the electrostatic potential, x is the gap between the ion and surface, ρ is the counter ion density, z is the valence of the ion, ε_0 and ε are the permittivity of vacuum and dielectric constant respectively, k is the Boltzmann constant and T is the absolute temperature. Combining PB equation with boundary conditions, a linearized Poisson-Boltzmann equation can be expressed as:

$$\psi = \psi_0 e^{-\kappa x} \quad (1.4)$$

where κ is called *Debye parameter*, a constant that determined by the electrolyte composition and temperature.²⁵ According to the equation, potential decays exponentially with the distance from the charged surface and the constant κ^{-1} has a length dimension which is defined as *Debye length* or called as electric double layer thickness.

However, surface potential ψ_0 is impossible to be measured experimentally, therefore we use zeta-potential (ζ) to study the surface potential property. Zeta-potential locates on the shear plane, which is very closed to the surface potential. Since it can be measured by many commercial instruments, it is always considered as an important characteristic of colloidal particles. By measuring the zeta-potential (ζ), the electrophoretic mobility μ_e can be calculated by Helmholtz-Smoluchowski (HS) equation :

$$\mu_e = \frac{\varepsilon\zeta}{\eta} \quad (1.5)$$

where ε is the electric permittivity of the medium and η is the liquid dynamic viscosity. This equation is valid when the particles size is larger than 0.1 μm . For the nanometer-scale particles ($\kappa a < 0.1$, a is the particle radius), electrophoretic mobility μ_e can be decided by Hückel equation:

$$\mu_e = \frac{2\varepsilon\zeta}{3\eta} \quad (1.6)$$

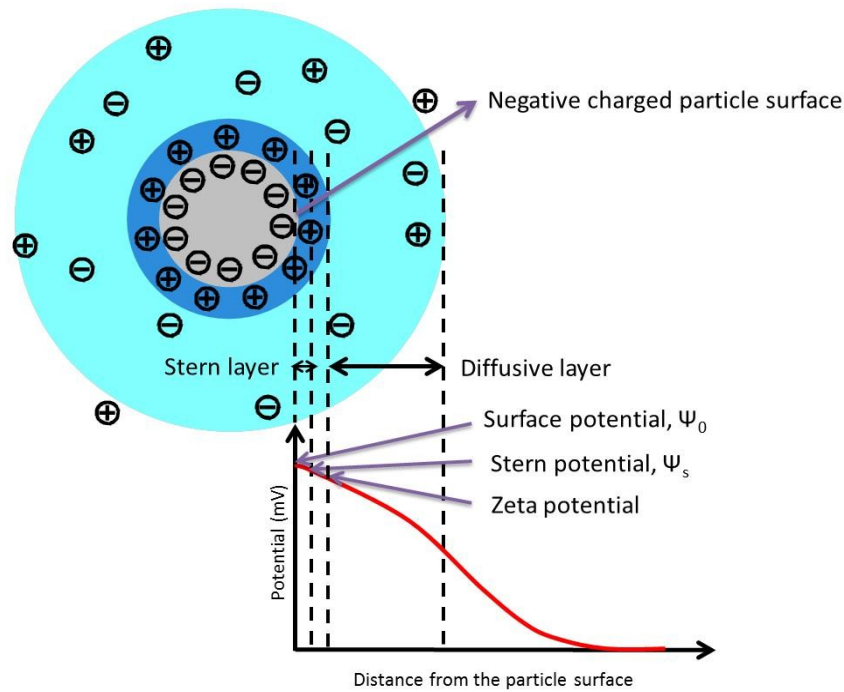


Figure 1.2. Schematic of electrostatic double layers of a negative charged particle surface.

1.4.5 Other interactions: Steric repulsion and bridging effect

Besides the interactions that discussed above, there are some other repulsive or attractive interactions that exist in polymer-polymer and polymer-particles systems. When the two polymer-covered surfaces come together, the outer polymer segments on both surfaces will overlap and they may repel each other because of the unfavorable entropy associated with structure compressing, which is called *steric repulsion*. However, *bridging effect* refers to that if the polymer coverage on both particles are not much, the free chains can form long loops or tails on the each other particle surfaces, increasing attractive forces between colloid particles. Usually, the interactions between polymer-covered surfaces depend on polymer structure, molecular weight, solution property and etc.²⁶

The polymer state on the surface in solution depends on its coverage. In ideal solution (θ -solution), there is no interactions between polymer segments and under this condition, the molecular radius approximately equals to *radius of gyration* R_g . Γ represents the coverage that is the number of grafted chains per unit area

$$\Gamma = 1/s^2 \quad (1.7)$$

where s is the mean distance between polymer anchoring points on the surfaces. For low coverage ($s > R_g$), there is no overlap with adjacent chains and each chain interacts with the other surface independently and those polymers are in *mushroom regime*. If the coverage is high ($s \ll R_g$), the layer thickness is larger than R_g and polymers are in *brush regime*.

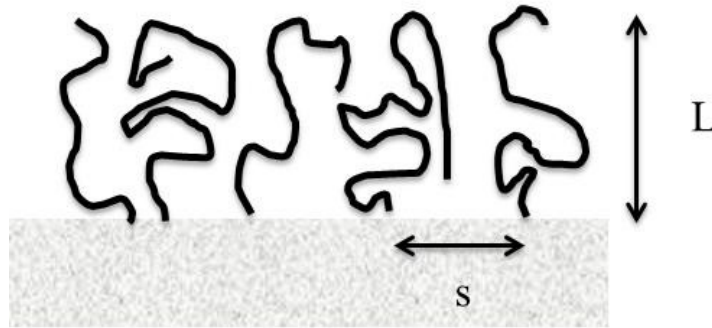


Figure 1.3. The schematic of adsorbed polymer chains in solution.

In real situation, the interactions are much complex. Polymer chains adsorb and desorb at the same time on the surface and they are in the thermal motion. Experimentally, there are many ways to study the polymer structure and surface interaction forces covered with polymer chains. The forces between polymer-covered surfaces are usually studied by surface force apparatus (SFA)²⁷.

Chapter 2 Experimental Techniques

2.1 Quartz crystal microbalance with dissipation monitoring (QCM-D)

2.1.1 Introduction of QCM-D

QCM-D is a powerful device to study the polymer adsorption kinetics on solid-liquid interfaces and adsorbed polymer structures.²⁸ The start of this technique can go back to late 19th century, when the piezoelectric effect was discovered and put into application. In 1959, Sauerbrey found the linear relation between resonance frequency change (Δf) and mass of the piezoelectric quartz crystal change (Δm) and proposed the Sauerbrey equation²⁹:

$$\Delta m = C \frac{\Delta f}{n} \quad (2.1)$$

where C is the constant related to the physical properties of the quartz and n is the resonance number of the sensor. Since it is easy to measure the small frequency change, it is then possible to calculate the mass changes on the sensors in a nano-scale. In 1980s, this technique found itself a wider application in many areas, such as molecular interaction and protein adsorption. However, Sauerbrey equation is valid only when the mass is rigid and no slip happens in the attachment. For the viscoelastic material, it is important to take the energy dissipation (the mechanical losses) into consideration. The dissipation factor is defined as the ratio between energy dissipated during the oscillation when energy stored in the oscillation system:

$$D = \frac{1}{Q} = \frac{E_{Dissipated}}{2\pi E_{Stored}} \quad (2.2)$$

With further development, QCM-D enables real-time accurate measurements of both mass and structural properties of molecular layers.

2.1.2 Working principle of QCM-D

In my project, Q-Sense E4, the second generation of QCM-D device, was used to analyse the polymer adhesion and structure changing and its schematic is shown in Figure 2.1. The instrument has four removable flow modules, each holding one chamber. The flow modules can be used in individual or parallel configuration to satisfy different measurement needs. In each chamber, the sensor crystal is mounted in the chamber with the crystal side parallelling to the lowering of the housing. Usually, specific sensor crystal is prepared or coated.

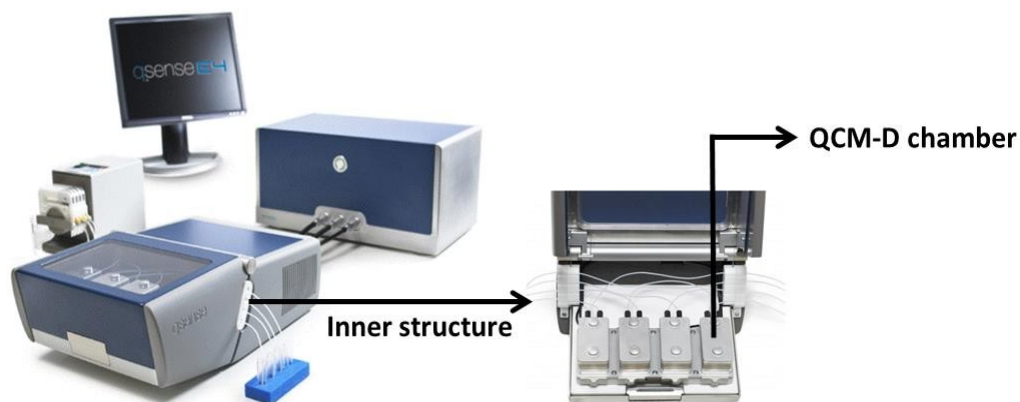


Figure 2.1. The schematic of QCM-D setup.

The structure of a typical sensor crystal is shown in Figure 2.2. Usually, it consists of a quartz disc and electrodes which are evaporated on both sides of the quartz disc. To

strengthen the adhesion effect, a gold layer with a chromium underlayer was coated on the surface. When it is inserted in a flow module, the active side (Figure 2.2 left) will contact with the sample and the changes of sensor surface properties will be analyzed by the QCM-D instrument.

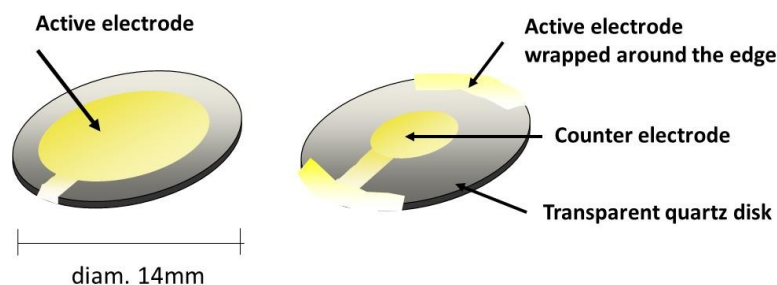


Figure 2.2. The schematic of sensor crystal structure.

When alternating current (AC) is added to the circuit, due to the quartz piezoelectric properties, the sensor crystal will cause the oscillation. As the mass that adsorbed on the sensor surface increases, the resonance frequency will decrease. By introducing a small resistor into the circuit, the dissipated energy can be recorded and calculated.³⁰

In my project, to study the adsorption properties on the silica sheet and alumina sheet of kaolinite particles, silica (SiO_2) and alumina (Al_2O_3) sensors were used to simulate the two surfaces. The structure of the two sensors are shown in Figure 2.3.

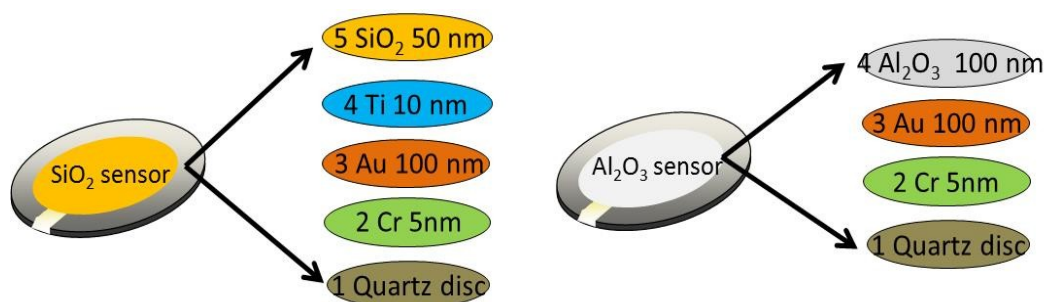


Figure 2.3. The layers built-up of the silica and alumina sensors.

2.2 Surface force apparatus (SFA)

2.2.1 Development of surface force apparatus

SFA is short for the surface force apparatus and it is a powerful device to measure the intermolecular interactions between two surfaces: such as physical forces³¹, electrostatic force³², hydrophobic interactions^{33, 34} and etc.³⁵⁻³⁷.

In 1969, the first SFA device was described by Tabor and Winterton in which the surface forces could be measured between the distance as low as 5-30 nm with a 3×10^{-10} m distance resolution³⁸. Multiple beam interferometry (MBI) was the first time to be applied in this device to measure jump distance. It was then possible to measure the force in air between mica or modified mica surfaces.

Based on the early version SFA, SFA Mk I was developed by Israelachvili and Adams in 1976 to expand the force measurement into the aqueous phase³⁹. By using a motor driven micrometer and a piezoelectric crystal to control the mica surface movement, the surface distance can be measured in the ångstrom level. Within ten years after this, SFA Mk II, described by Israelachvili, came into application as an improvement of SFA Mk I to enable more studies on interfacial phenomena⁴⁰. In order to improve strength and

prevent the surfaces from rotating, a double-cantilever spring was used to replace the single cantilever spring. Besides, they also added 'friction device' into Mk II to allow friction force measurement with the upper surface to be moved in the lateral direction.

To satisfy the requirement of system complexity and stability, SFA Mk III was developed and tested by Israelachvili and McGuiggan in 1985-1989⁴¹. Mk III was more compatible with the force measurement in liquid system. The range of the measurement distance was also increased from ångstrom to the millimeter level.

Although SFA Mk III is very table and functional, there are still some drawbacks to limit its application. SFA 2000 was designed with fewer parts and it is much easier to produce, operate and clean. The schematic of the main components of SFA 2000 is shown in Figure 2.4. The main components of this device are micrometers, the main stage with central single-cantilever spring and the lower and the upper disk holders. There are four main controls: the coarse and medium controls are driven by the micrometer, the fine control is manipulated by a motor and the ultra-fine control which can move the upper surface is combined with piezoelectric device.

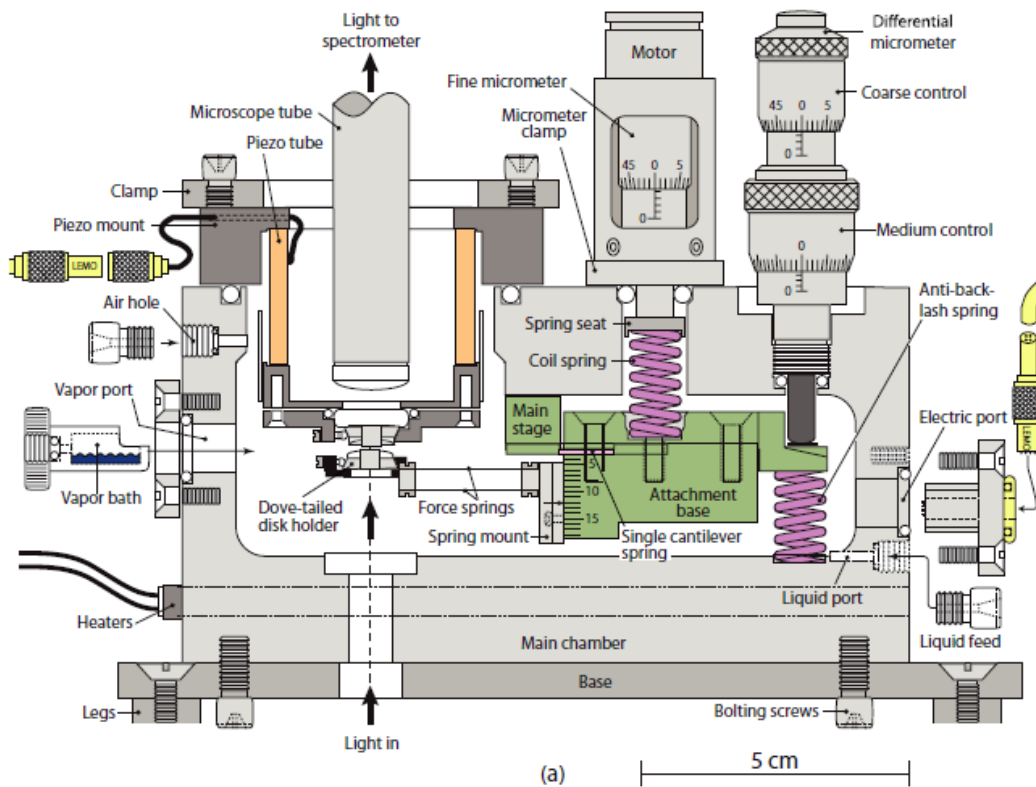


Figure 2.4. The schematic of SFA 2000 main components

The schematic of the SFA setup is shown in Figure 2.5. The basic principal is that when light comes through the two opposite curved cylindrical disks (usually, silver-coated mica was glued on the disks) and goes the spectrometer slit, the fringes of equal chromatic orders (FECO) are generated⁴² and recorded by video camera. A change of the optical path between the two surfaces modifies the interference shape and the fringes of equal chromatic order (FECO) will be shifted in wavelength (shown in Figure 2.6⁴³). The wavelengths information can be used to calculate the gap layer distance and the layer refractive index.

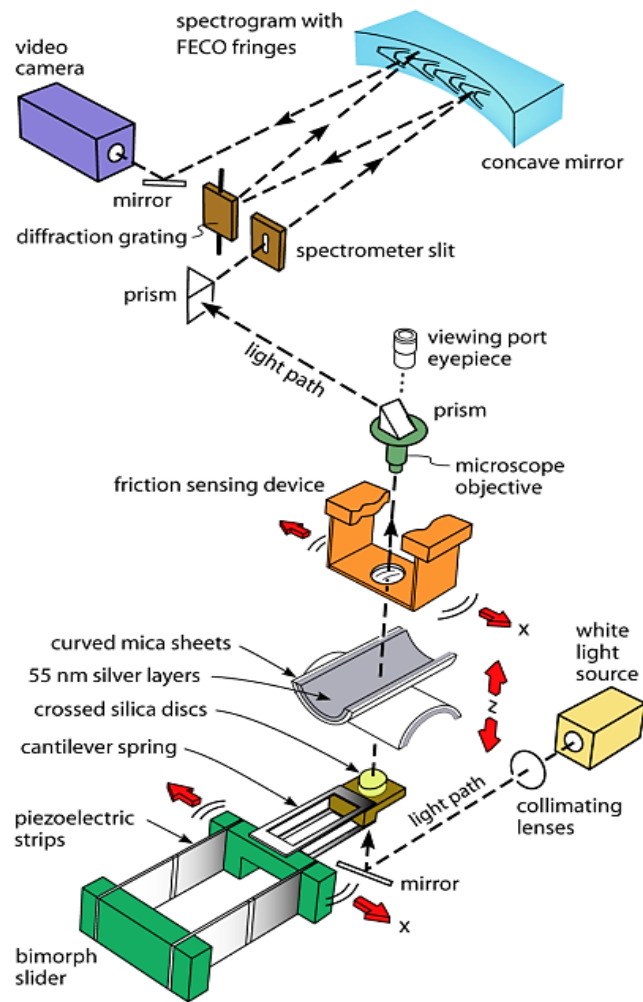


Figure 2.5. The schematic of the SFA setup

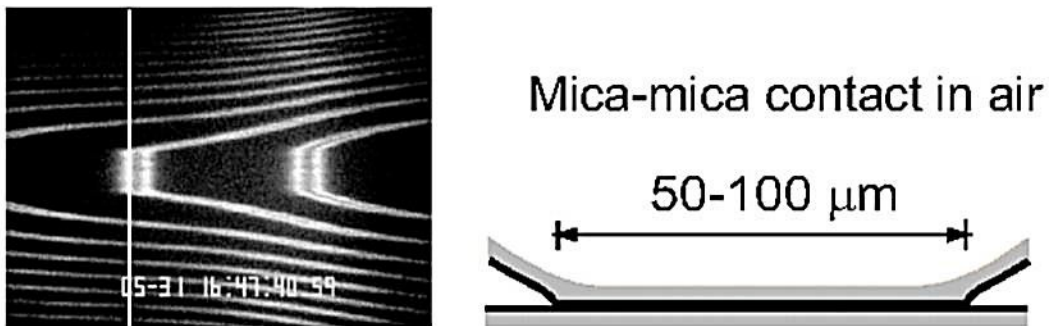


Figure 2.6. A typical FECO of two back-silvered mica sheets in contact in air.

2.2.2 Multiple beam interferometry (MBI) technique

MBI device is used to study the absolute surface separation distance and surface shape^{44, 45}. Usually, cylindrical disks with mica glued on are mounted into the chamber to simulate the sphere-flat geometry. When the light coming through the disks surfaces, it may reflect back and forth in between the silver layers and Newton's rings are created near the closest points of the two surfaces. When the transmitted light is coming through the spectrometer, a set of discrete wavelengths can be visible on the screen, which is called the fringes of equal chromatic order (FECO). If the two surfaces contact with each other without medium in between, the mica thickness can be determined by the wavelength of the n th order fringe, λ_n^0 ($n=1, 2, 3, \dots$), and the fringe order is determined by

$$n = \frac{\lambda_{n-1}^0}{\lambda_{n-1}^0 - \lambda_n^0} \quad (2.3)$$

where λ_{n-1}^0 is the next fringe at higher wavelength. If there is a gap with distance D between the two mica surfaces, the fringes shifts are related to the refractive index of the medium in the gap and the original contact points^{44, 46}:

$$\tan\left(\frac{2\pi\mu D}{\lambda_n^D}\right) = \frac{2\bar{\mu} \sin\left[\pi\left(1 - \frac{\lambda_n^0}{\lambda_n^D}\right) / \left(1 - \frac{\lambda_n^0}{\lambda_{n-1}^0}\right)\right]}{(1 + \bar{\mu}^2) \cos\left[\pi\left(1 - \frac{\lambda_n^0}{\lambda_n^D}\right) / \left(1 - \frac{\lambda_n^0}{\lambda_{n-1}^0}\right)\right] \pm (\bar{\mu}^2 - 1)} \quad (2.4)$$

If n is the odd order fringe, then + is taken, similarly, if n is the even order fringe, – sign is used. The refractive is decided by $\bar{\mu} = \frac{\mu_{\text{mica}}}{\mu}$, where μ_{mica} is the refractive index of mica at λ_n^D , and μ is the medium refractive index. If the separation within the two surfaces is less than 30 nm, the equation (2.4) can be reduced into two expressions:

$$D = \frac{nF_n(\lambda_n^D - \lambda_n^0)}{2\mu_{\text{mica}}} \text{ (when } n \text{ refers to odd order fringe) (2.5)}$$

$$D = \frac{nF_n(\lambda_n^D - \lambda_n^0)\mu_{\text{mica}}}{2\mu^2} \text{ (when } n \text{ refers to even order fringe) (2.6)}$$

where F_n is a correction factor that compensates for refractive index dispersion and phase change of the reflection.

2.2.3 Surface force measurement using the SFA

2.2.3.1 Mica sheet preparation

Mica is the most common material that used as the substrates in SFA experiments. Usually, a piece of thick Ruby Muscovite mica will be cleaved several times by hand to get surface-smooth and step-free mica sheets with a thickness around 1-5 μm . Then they are cut with a hot platinum wire and deposited on a mica backing sheet. The upper sides of the mica surfaces (opposite to the back sheet) will be coated with silver to increase the light refraction.

Before the surface force experiments, silver-coated fresh mica sheet will be peered from the backing sheet and glued on two curve silica disks. Then the disks will be

carefully mounted into the SFA chamber. Any harm or dust on the mica surface is detrimental to the experiment.

2.2.3.2 The basic mechanism of force measurement

The normal force change can be calculated according to the Hooke's law:

$$\Delta F = k(\Delta D_{\text{applied}} - \Delta D_{\text{meas}}) \quad (2.7)$$

where k is the spring constant, $\Delta D_{\text{applied}}$ is the distance that moved by micrometers, and ΔD_{meas} is the actual distance that measure by MBI technique (shown in Figure 2.7).

When $\frac{\partial F(D)}{\partial D} > k$, the lower surface will have a quick jump toward or away from the contact point on upper surface. By measuring the jump distance ΔD_{jump} , adhesion force can be calculated by:

$$F_{\text{adhesion}} = k \times \Delta D_{\text{jump}} \quad (2.8).$$

If we divide the adhesion force by the radius R of the curved cylindrical disks, we can calculate the interaction energy per unit area between two flat surfaces by using the Derjaguin approximation⁴⁷, which is:

$$W_{\text{flat}}(D) = \frac{F_{\text{curved}}(D)}{2\pi\sqrt{R_1R_2}} = \frac{F_{\text{curved}}(D)}{2\pi R} \quad (2.9)$$

when $R_1 = R_2 = R$.

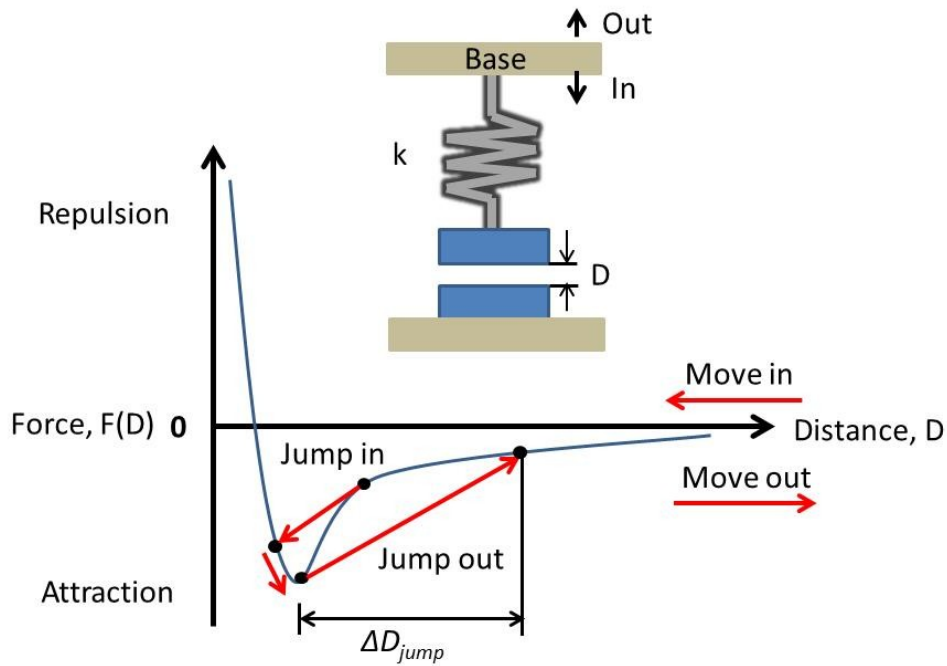


Figure 2.7. Force-distance profile in normal force measurement

2.3 Zetasizer Nano

2.3.1 General introduction of Zetasizer Nano

Generally, Zetasizer Nano is very useful in measuring the particle size, zeta potential and molecular weight in wide range. Coupled with Zetasizer Nano software, particle characteristics can be easily measured and analyzed at the same time. Combined with different accessories, Zetasizer Nano is also able to perform the microrheology measurement, autotitration measurement (if it contains an MPT-2 accessory) and trend measurement. The range of the particle sizes for different measurement are different according to the model of Zetasizer Nano series, some of which have been described in Table 2.1.

Table 2.1. Zetasizer Nano models and measurement specifications.

Zetasizer Nano model	Size range maximum (diameter)	Size range for Zeta potential (diameter)	Molecular weight range
S	0.3nm to 10 μm	–	342 Da to 2×10^7 Da
Z	–	3.8 nm to 100 μm	–
ZS	0.3nm to 10 μm	3.8 nm to 100 μm	342 Da to 2×10^7 Da
S90	0.3nm to 5 μm	–	342 Da to 2×10^7 Da
ZS90	0.3nm to 5 μm	3.8 nm to 100 μm	342 Da to 2×10^7 Da
Nano ZSP	0.3nm to 10 μm	3.8 nm to 100 μm	342 Da to 2×10^7 Da

2.3.2 Zeta potential measurement

Zeta potential has been defined in Chapter one that is the potential that locates at the boundary of slipping plane. Since the real surface potential is impossible to measure, zeta potential indicates the potential stability of the colloid system. When an electric field is added across the electrolyte, charged particles will travel to the opposite electrode direction whereas the viscous forces will oppose this movement. When the two forces reach the equilibrium, the particles can move at a constant velocity. In this instrument, electrophoretic mobility of the particle is measured and converted into zeta potential. The dip cell used for zeta potential measurement is shown in Figure 2.8. Normally, we choose DTS1070 cell for the zeta potential measurement for every single sample. It should be noted that during measurements, electrolytes are moving towards their opposite electrodes, which will polarize the field in the sample making it non-homogenous. Usually, a pausing time (i.e. 3 minutes) can be set up between the measurements to avoid this problem.

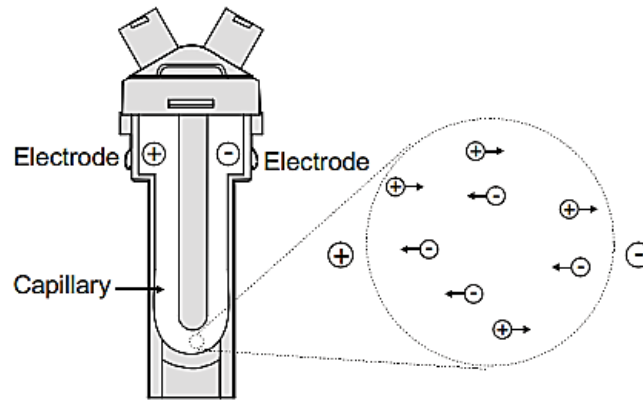


Figure 2.8. The schematic of a typical zeta potential measurement cell.

2.3.3 Dynamic light scattering (DLS)

By illuminating the particles a laser, dynamic light scattering is able to measure the time dependent fluctuation in the intensity of the light which is scattered by the particles in Brownian motion. In solutions, small particles move more quickly while large particles move more slowly. The relationship between the size of the particle and moving velocity can be defined by Stokes-Einstein equation:

$$D = \frac{k_B T}{6\pi\eta r} \quad (2.10)$$

where D is the diffusion constant; k_B is the Boltzman's constant, T is the absolute temperature, η is viscosity and r is the radius of the spherical particle. As the particles move around, the scattered light will cause the bright and dark areas to grow and diminish in intensity. By measuring the rate of fluctuation, the particle size can be calculated by the Zetasizer Nano software (shown in Figure 2.9²⁰).

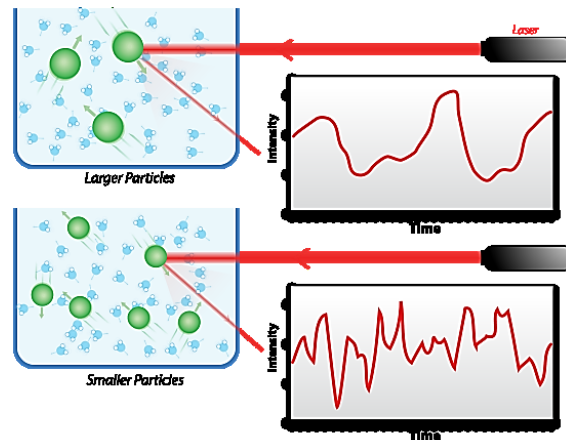


Figure 2.9. Light intensity fluctuation of two samples: larger particles (top) and smaller particles (bottom).

2.3.4 Molecular weight measurement

In Zetasizer Nano device, molecular weight can be determined by a technique called Static Light Scattering (SLS). It is a useful and non-invasive measurement to study the molecules behavior in solutions. Similar with the theory of DLS, sample molecules are also illuminated by the laser light but SLS measures the intensity of scattered light instead of time dependent fluctuations. The intensity of light scattered over a period of time (e.g. 10 to 30 seconds) is accumulated for a number of concentrations of the sample and the intensity of scattered light is proportional to the weight average molecular weight (Mw) and the concentration of the particle.

Usually, the background solvent and gradient concentrations of the sample are prepared. The intensity of the scattered light (KC/R_θ , where K is optical constant, C is concentration of the sample and R_θ is the Rayleigh ratio) of various concentrations is compared with the scattering produced from the standard solvent. The weight averaged

molecular weight can be determined from the intercept at zero concentration, where $KC/R_\theta = 1/M_w$ and M_w is expressed in Daltons (or g/mol) (shown in Figure 2.10).

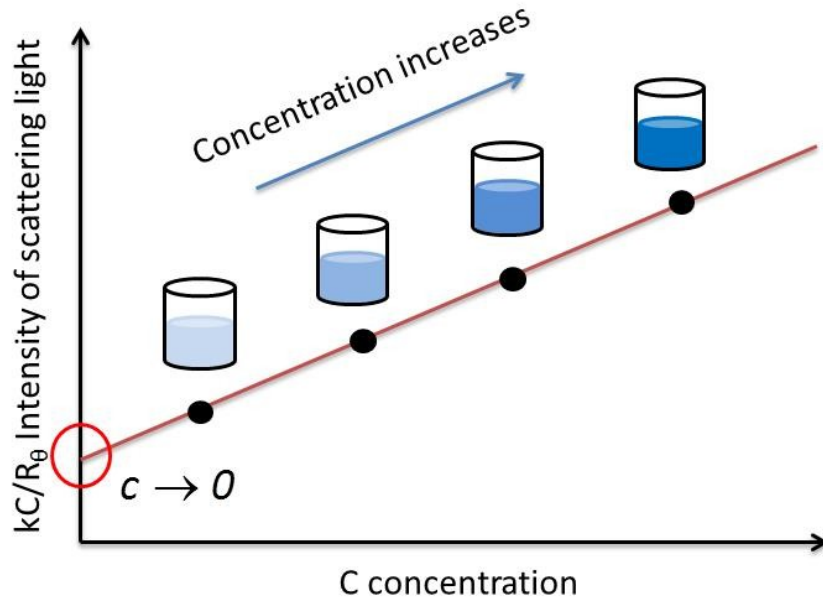


Figure 2.10. Weight averaged molecular weight (M_w) measurement procedure by SLS technique.

2.4 Electron beam evaporation system #1 (Gomez)

Electron beam evaporation system (shown in Figure 2.11) is a form of physical vapor deposition in which a target anode is bombarded with an electron beam given off by a charged tungsten filament under high vacuum. The electron beam causes the atoms from the target to transform into the gaseous phase. These atoms then precipitate into the solid form, coating everything in the vacuum chamber (within line of sight) with a thin layer of the anode material. This systems are ideal for depositing metals, oxides, magnetic materials and dielectrics in applications such as nanotechnology, optics, microscopy, MBE, functional and decorative coatings.



Figure 2.11. Electron beam evaporation system.

2.5 Atomic force microscopy

High-resolution scanning probe technique was developing rapidly in the early 1980s. The first commercial atomic force microscopy (AFM) was first introduced in 1989. It is the one of the most advanced tools for surface force measurement, studying topography with atomic resolution⁴⁸.

There are three modes of AFM: contact mode, non-contact mode and tapping mode, usually, in order not to damage the sample surface tapping mode is widely used in imaging. In the atomic force microscopy tapping mode, a cantilever with a sharp probe at the end is attached to an actuator (a piezo). The height of the cantilever is controlled by the Z-piezo. According to the input voltage, the cantilever can oscillate according to the signal and drive the cantilever to oscillate in turn. The oscillating cantilever contacts the

sample intermittently, which decreases the possibility of surface damage. When the tip comes closed to the surface the sample, due to Hooke's law, forces between the tip and sample lead to deflection of the cantilever. When the tip scans over the surface, the height of the cantilever is adjusted up or down to keep the deflection constant. Thus, the height data is traced with Z-piezo position. The topographic image of the sample can be obtained by plotting the deflection of the cantilever versus its position on the sample. The schematic of AFM imaging mechanism is briefly shown in Figure 2.12.

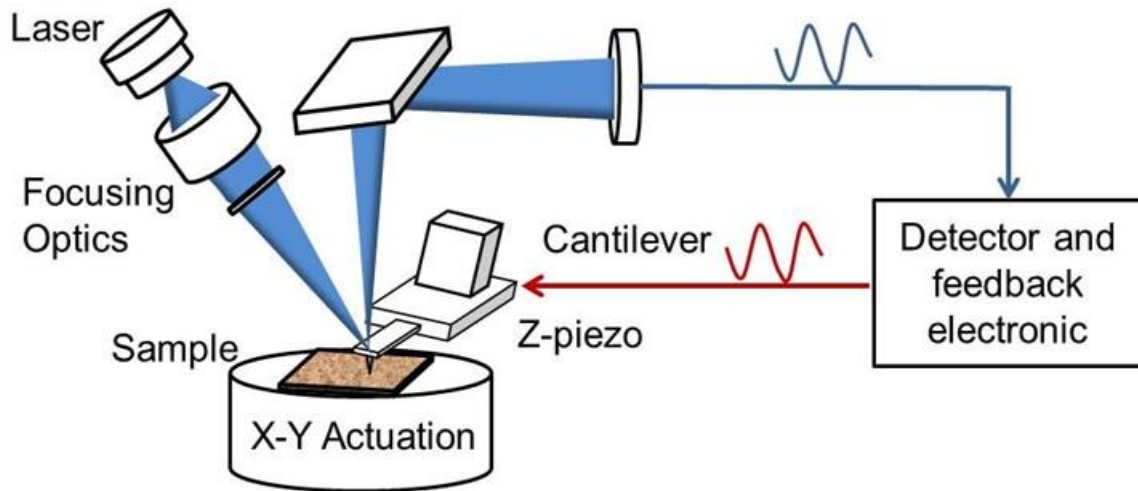


Figure 2.12. Schematic of AFM imaging mechanism

Chapter 3 The study of MgCl_2 's Effect on Enhancing Magnafloc 1011 Flocculation on the Model Clay

3.1 Introduction

Fresh water represents a major component in the mineral processing operations.^{49,}
⁵⁰ However, mines in many countries are facing water restriction, which is becoming a critical issue in global mineral industry. An urgent demand is in great need for increasing water recycling and reuse, or alternative water resource, e.g. high saline water, sea water. However, in 1989, the negative effects of increasing usage of the recycle water was investigated and inorganics (Ca^{2+} , Mg^{2+}) was found to accumulate dramatically in recycle water for Niobec ore.⁵¹ Recently, the influence of high salinity has always been considered in interactions between particles in tailing treatment. In saline solution, the compressed electric double-layer repulsion will inhibit the further approaching of charged particles, thus aggregation between particles is difficult to achieve simply by Brownian motion.⁵² The effect of salinity on particle-particle interactions under various conditions has been well explained by DLVO (Derjaguin and Landau, Verwey and Overbeek) theory.⁵³ According to the theory, with the addition of flocculants or coagulants, electrostatic repulsion between particles can be overcome by syncretic interactions from hydrogen bonding, van der Waals attractions and electrostatic attraction.⁵⁴

Among commercial flocculants, anionic polyelectrolytes have wide applications in mineral processing^{55, 56}, papermaking⁵⁷ and waste water treatment⁵⁸. With excellent flocculation capability, anionic polyelectrolytes enables to form large flocs by binding particles and enhance particle flocculation.⁵⁹ But introducing of anionic polyelectrolytes into colloid particle system brings challenge to understand the mechanism of flocculation. To comprehend the process systematically, many parameters have been investigated so far, such as pH and ionic strength of the tailings, flocculant molecule weights (MWs), charge densities (CDs) and flocculant dosage.⁶⁰⁻⁶⁴ In terms of ionic strength, divalent cations (Ca^{2+} , Mg^{2+}) have been reported to enhance the anionic polyelectrolyte-mediate flocculation by reducing electrostatic repulsion between anionic polyelectrolytes and negatively charged surfaces of the suspended particles. The settling of the Syncrude tailings treated by Percol 204 (anionic PAM with 30% CD) was dramatically improved by addition of 0.008 mol/L Ca^{2+} or Mg^{2+} ions, which was contributed to the enhanced bridging effect between flocculant molecules and particles in divalent medium.⁶⁵ Besides, 1 mM Ca^{2+} or Mg^{2+} were found to enhance the adsorption of PAM on the particle surfaces by studying on kaolinite suspensions treated by anionic PAMs in NaCl, CaCl_2 and MgCl_2 solutions.⁵⁴ Divalent cations not only decreased the negative zeta potential but also greatly increased the maximum anionic PAM adsorption capacity by reducing the electrostatic repulsion between the anionic PAM molecules and kaolinite particles.⁶⁶ In a previous work by Yaguan Ji and his coworkers, the settling performance and surface interactions between anionic PAM flocculant and kaolinite particles under high salinity conditions (i.e. NaCl and CaCl_2) were systematically studied.⁶⁷ It was found that the

presence of high concentrations of NaCl and CaCl₂ could increase the initial settling rate of kaolinite suspensions, which reduced the repulsion forces between the solid particles and also induced hydrogen bonding (between solid surface and polymer flocculant). But the properties of interactions between anionic polyacrylamide and alumina or silica groups in MgCl₂ solutions have not been fully studied in details. Even though many mechanism models have been proposed to correlate the settling behavior and molecular interactions, only a few sophisticated microscopic techniques have been probed into this field. For example, atomic force microscope (AFM) has been applied to measuring the single polymer loop length distribution⁶⁸ and desorption force of H-PAM molecules on silica, mica and bitumen surfaces⁶⁹. The adsorption characteristics of PAMs on anisotropic basal plans of kaolinite was investigated by Quartz Crystal Microbalance with Dissipation (QCM-D).⁷⁰ Dynamic Light scattering (DLS) enables to determine the hydrodynamic radius of a novel polymeric hydrogel synthesized by grafting synthetic polyacrylamide chains onto HPMC backbone (HPMC-g-PAM).⁷¹ Surface Force Apparatus (SFA), a powerful molecular force probe for determining surface-surface interaction forces,^{72, 73} has not yet been applied in understanding interactions between anionic PAM flocculant and silica and alumina surfaces⁷⁴.

High molecular weight Magnafloc 1011 and kaolinite in this work were chosen as model anionic flocculant and model clay respectively to study the interactions between flocculant molecules and particle surfaces in MgCl₂ solutions. Initial settling rate (ISR) and turbidity were considered as evaluation criteria for the settling performance. The molecular interactions between MF and the basal plane/edge surface of kaolinite were

studied by SFA and QCM-D, combining with turbidity, zeta-potential and DLS. A comprehensive understanding of flocculation mechanism between anionic flocculant and particles in divalent ion solution was finally proposed.

3.2 Materials and experimental methods

3.2.1 Materials

Kaolinite of high-purity was obtained from Acros Organics to prepare model clays tailings (particle size range~1.45 to 22.9 μm , D_{50} ~5.75 μm , ρ ~2.60 kg/dm^3). The anionic polyacrylamide Magnafloc 1011 was purchased from Ciba Specialty Chemicals Basel (Switzerland), the properties of which are shown in Table 3.1. Polymer stock solution was prepared at concentration of 1000 ppm in Milli-Q water (Resistivity ~ 18.2 $\text{M}\Omega\cdot\text{cm}$) and stabilized for two days prior to use. MgCl_2 (Certified ACS, Fisher Scientific Canada) solutions were prepared by adding salts in the Milli-Q water to a required concentration. Analytical-grade KOH and HCl (0.01 M - 1 M) (Fisher Scientific Canada) were used to adjust the solution pH.

Table 3.1. Properties of Magnafloc 1011.

Polymer	Structure	Molecular weight (unit)	Charge density (%)	Segment length (nm)
Magnafloc 1011		1.75×10^7	27	0.304

3.2.2 Settling test

The settling test procedure was reported in details elsewhere⁷⁵. The schematic of the settling test setup is shown in Figure 3.1. 0.01 M, 0.1 M and 1 M MgCl₂ solutions were prepared in the 1000 mL volumetric flasks. Model tailings were prepared at kaolinite/Milli-Q water or kaolinite/ MgCl₂ solution at weight ratio of 1:20 in a 2 L beaker. 5 wt% kaolinite suspensions were prepared and stirred at low agitation speed overnight. In each test, 90 mL in total of slurry sample was collected by the pipet (Eppendorf Easupet Motorized Pipet, Fisher, US) from three different positions (Figure 3.1(b)) of the bulk solution under 500-600 rpm and transferred into a 250 mL standard beaker. Afterwards, each collected sample was stirred under 600 rpm for 2 minutes to achieve well dispersed suspension, and designated amount of MF flocculant stock was added into the collected sample under agitation at 300 rpm. Agitation was stopped immediately after adding polymer flocculant. After mixing, the slurry sample was transferred into a 100 mL graduate cylinder to observe the settling performance. The cylinder was inversed five times and the mudline (defined as interface between suspensions and sediments⁷⁶) was monitored as a function of settling time to obtain the settling curves. The initial settling ratio (ISR) was defined as the slope early linear line. After settling for 18 hrs, the turbidity and zeta potential of the supernatant were measured by Micro-100 Turbidity Meter (Fisher, US) and zeta potential analyzer (Nano Zetasizer, Malvem).

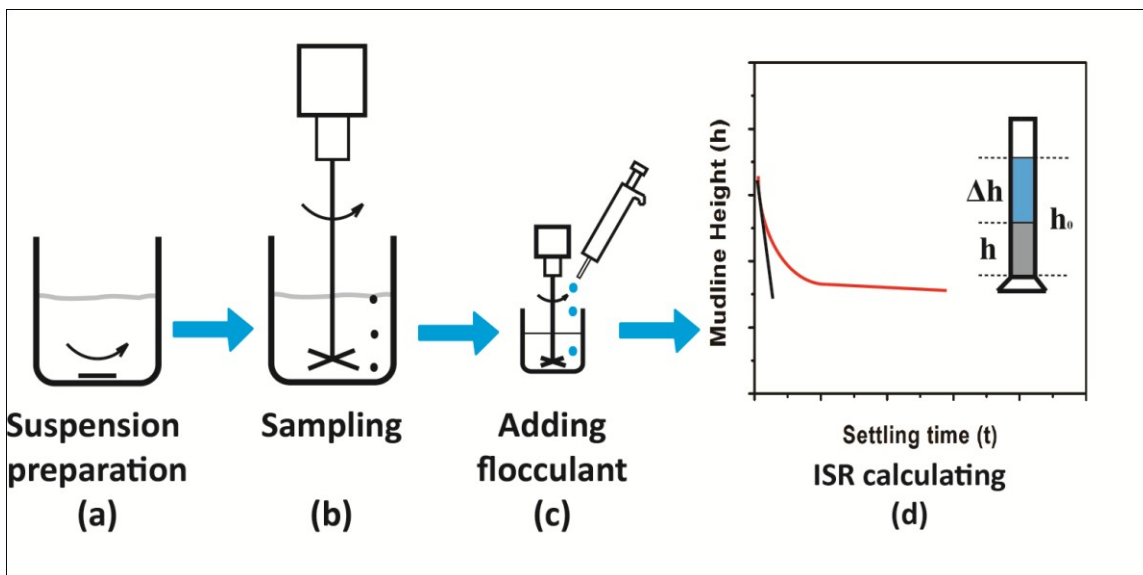


Figure 3.1. The schematic of the settling test procedure

3.2.3 Surface force measurement

SFA has been widely used in measuring physical forces between surfaces, such as van der Waals, electrostatic forces, adhesion and bio-specific interaction, etc.⁷⁷⁻⁸⁰ In this study, the interactions between model clay surfaces (i.e. mica and alumina) with the medium of MF stock solution with salt addition were determined by the SFA 2000 (Surforce LLC, Santa Barbara, CA, USA) which is coupled with Multi-Beam Interferometry (MBI) technique. The schematic of the setup for SFA 2000 is shown in Figure 3.2.

A detailed description on the SFA experiments was reported elsewhere.⁷⁸ Basically, a thin mica sheet (1-5 μm thick) was coated with a semi-reflective layer of silver (~ 50 nm thick) to obtain multiple beam interference fringes of equal chromatic order (FECO). Surface separation distance D , surface geometry and deformation can be determined by FECO in situ and in real time. A thin silver-coated mica sheet was glued onto a

cylindrical silica disk (radius $R=2$ cm). The prepared silica disks pair was mounted into the SFA chamber in a cross-cylinder geometry, which was locally equivalent to a sphere of radius R interacting with a flat surface or two sphere of radius $2R$ when the separation of the two surfaces was much smaller than R . With this arrangement, the measured force between two cylindrical surfaces $F(D)$ can be converted to interaction energy per unit area between two flat surfaces $W(D)$ by the Derjaguin approximation : $F(D) = 2\pi RW(D)$. Normal forces between the two surfaces were measured by moving the lower surface supported on a double-cantilever ‘force springs’ towards the upper surface by a distance $\Delta D_{applied}$. The actual distance, ΔD_{meas} , was measured by MBI in real time. The change in the force ΔF between the surfaces, when they came to rest at a separation distance D , was calculated from the deflection of the cantilever spring by, $\Delta F(D) = k (\Delta D_{applied} - \Delta D_{meas})$, where k is the spring constant. When $\partial F(D)/\partial D$ is greater than the spring stiffness, there is a mechanical instability that causes the lower surface to jump either toward or away from the upper surface during the approaching or separation process, respectively.

In 1994, forces between alumina surfaces of single-crystal sapphire platelets in salt solutions were successfully measured by SFA.⁸¹ In this study, alumina surface (~ 20 nm thick film), was coated by method of Electron Beam Evaporation on surface of mica sheet to represent the alumina component in mineral particle. Mica surface was used to simulate the silica basal plane. During a typical force measurement, the polymer salt solution was first filtrated by a Millex-AA Filter Unit (pore size ~ 0.8 μm , EMD Millipore) and then injected between the mica surfaces or alumina surfaces incubating for 30 mins. The normalized force-distance profiles F/R vs. D were then obtained by an initial

approach to a “hard wall” followed by separation of the two surfaces. The hard wall in this study was defined as thickness of confined polymers which barely changed with increasing the normal load or pressure using mica-mica or alumina-alumina as the reference. The mica-mica or alumina-alumina reference ($D=0$) was determined at the adhesive contact between mica surfaces or alumina surfaces in air.

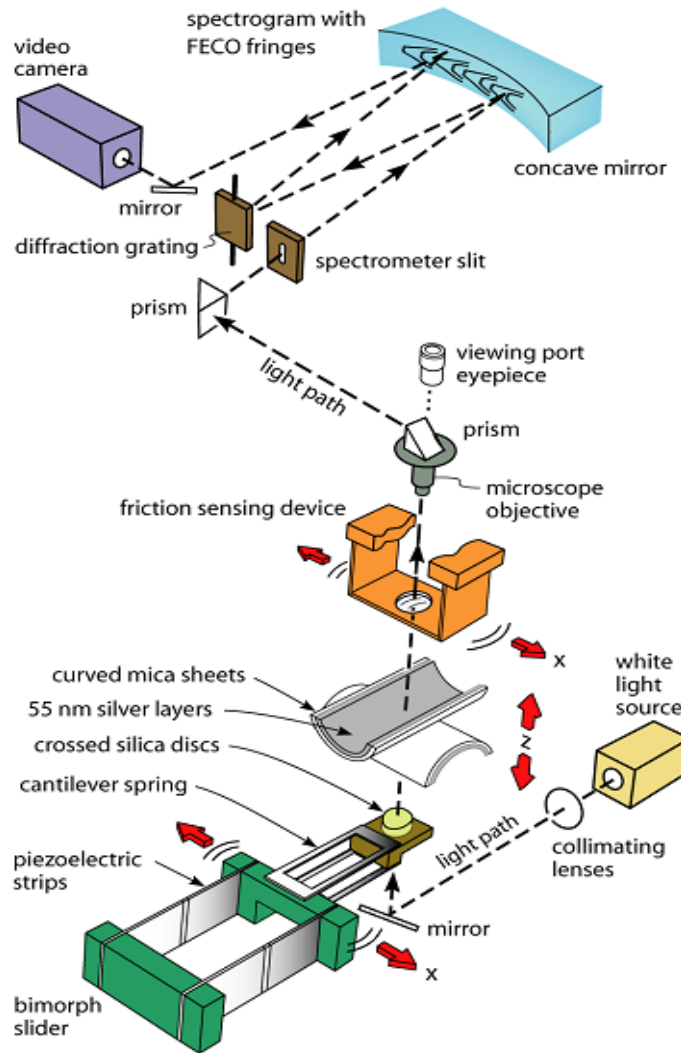


Figure 3.2. The schematic of the setup of SFA 2000.

3.2.4 Measurement of the hydrodynamic radii of the MF in salt solutions

Dynamic light scattering (DLS) was used to determine the molecular conformation of MF in bulk MgCl₂ solutions. An ALV/CGS-3 Platform based Goniometer System was used to determine the hydrodynamic radius (R_H) of MF molecules in solution, which is defined as the radius of a hypothetical hard sphere that diffuses with the same speed as the polymer molecule under the test condition. 50 ppm MF in 0.01 M, 0.1 M and 1 M MgCl₂ solutions were filtrated by a Millex-AA Filter Unit (pore size ~0.8 μ m, EMD Millipore) to remove possible impurities before the measurement.

3.2.5 Adsorption measurement of the MF on the model clay surfaces using QCM-D

To fully understand the MF 1011 adsorption properties on anisotropic basal planes of kaolinite particle, QCM-D, a powerful technique was applied to provide adsorption of polymer at solid-liquid interfaces and the conformation of the adsorbed polymer layers²⁸. QCM-D enables real-time, label-free investigation of molecular adsorption and/or interactions on various solid sensor surfaces and the conformation of the adsorbed polymer layers. Basic principle about this technique has been reported by other literatures^{82, 83}. Principally, resonance frequency (Δf) and energy dissipation (ΔD) of QCM-D sensors are monitored simultaneously to determine the adsorbed mass and structural stiffness properties of the adsorbed layers respectively. The decrease of frequency indicates the accumulating of polymer layer on the sensor surface. A stiffer adsorbed layer generates less change in dissipation while a viscoelastic layer that incorporates solvent molecules leads to a larger dissipation.

Silica and alumina sensors were used in this study as models of these two distinct surfaces in the kaolinite particles.²⁸ All the polymer stock solutions were adjusted to pH ≈ 7.5 before the experiment. Background solution (pure MgCl_2 solution) was introduced into the QCM-D system which was recorded at first as a baseline where Δf and ΔD are defined as zero. Then the polymer solution was pumped over the QCM-D sensor and Δf and ΔD were recorded in real-time. After the Δf and ΔD reached equilibrium, each chamber was rinsed by background solution to remove any unbound polymers. The final Δf and ΔD values and the associated kinetics analysis data were very useful to understand the MF adsorption quantity and polymer conformation on the sensor surfaces in MgCl_2 solutions with various concentrations.

3.3 Results and discussion

3.3.1 Evaluation of MF settling performance on kaolinite suspension in MgCl_2 solutions

3.3.1.1 Initial settling rate (ISR)

The ISR of the 5 wt% kaolinite suspension as a function of MF dosage in MgCl_2 solutions with different concentrations at pH 7.5 is shown in Figure 3.3. Without flocculant addition, ISR in all MgCl_2 concentration range solutions were nearly 0 m/hr, which indicated addition of MgCl_2 could not cause flocculation and aggregation in kaolinite suspension. Meanwhile, in the Milli-Q water, the ISR values in all MF dosage range were all less than 1 m/hr and gel-like suspension was observed to prevent the formation of large flocs under high MF dosages. The ISR increased sharply with increasing MF dosage from 25 ppm in all the cases and then reached maximum at certain

MF dosage in different cases. For 0.01 M MgCl_2 , the settling rate increased to the maximum of 120 m/hr at dosage of 50 ppm and decreased with further addition of MF. Similar tendency was observed in 0.1 M MgCl_2 case. The maximum ISR of suspension in 1 M MgCl_2 was about 170 m/hr at MF dosage of 75 ppm. The maximum ISR shifted to higher MF dosage as salt concentration increased from 0.01 M to 1 M, indicating that in high MgCl_2 concentration solution, kaolinite settling consumed great amount of MF to achieve the maximum ISR. The existence of Mg^{2+} enhanced the MF flocculation in kaolinite suspension, which might be due to the high concentration Mg^{2+} could accelerate reducing electrostatic repulsion between negatively charged suspended particles and building bridges between MF molecules and particle surfaces.

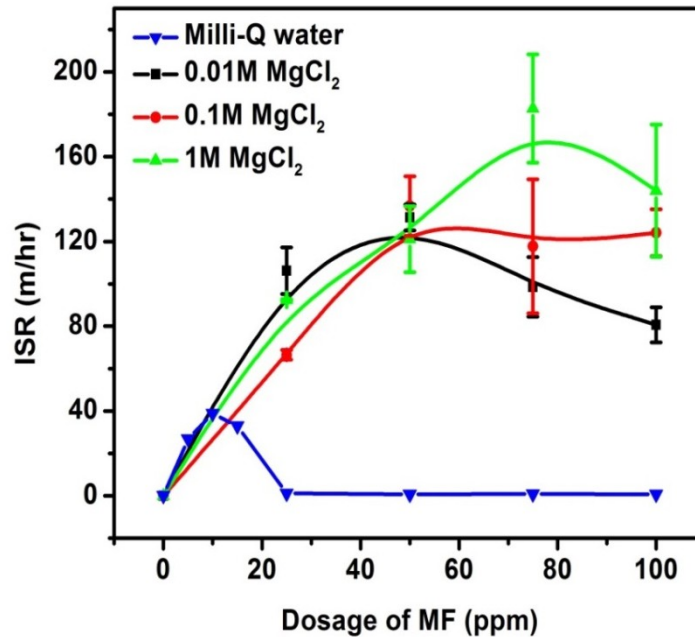


Figure 3.3. The initial settling rate of 5 wt% kaolinite suspension as a function of MF dosage at pH 7.5 prepared by Milli-Q water (▼), 0.01 M (■), 0.1 M (●) and 1 M (▲) MgCl_2 solutions.

3.3.1.2 Turbidity of the supernatant

The turbidity of the supernatant of kaolinite suspension after settling for 18 hours as a function of MF dosage at different concentrations of MgCl_2 solutions is shown in Figure 3.4. Turbidity reflects the clarity degree of supernatant and it is an important indicator of good flocculation. Lower supernatant turbidity indicates a better flocculation effect. The pictures of the settling results in kaolinite/Milli-Q water and 0.01 MgCl_2 solutions were shown in Figure 3.5. The milk-like supernatants in all samples were due to large quantity of stably suspended kaolinite particles. The turbidity of the supernatant in kaolinite/Milli-Q suspension was out of the detective range of turbidity meter, thus was not shown in Figure 3.4. However, on contrast, the turbidity in the MgCl_2 solution of different concentrations were rather, around 3~5 Nephelometric Turbidity Unites (NTU). Comparing turbidity in each case, various MF dosages did not have significant effect on turbidity of the supernatant. Besides, the concentration of MgCl_2 also showed negligible influence on the turbidity of the supernatant of the kaolinite suspensions.

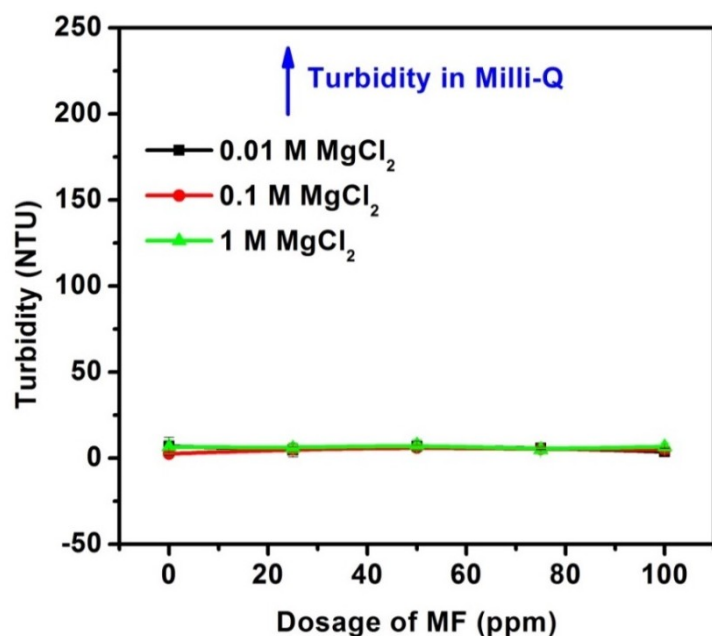


Figure 3.4. The turbidity of the supernatant of 5 wt% solid kaolinite suspension prepared with 0.01 M (■), 0.1 M (●) and 1 M (▲) MgCl₂ solutions after 18 hrs-settling versus MF dosage at pH 7.5.

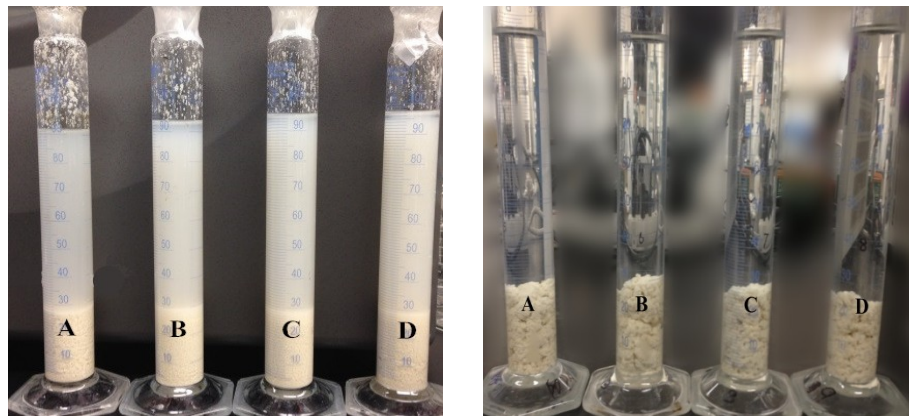


Figure 3.5. Settling images of the kaolinite suspensions prepared in Milli-Q water (left) and 0.01 M MgCl₂ solution (right) with different MF dosages: A 25 ppm; B 50 ppm; C 75 ppm; D 100 ppm after 18 hrs-settling at pH 7.5.

3.3.1.3 Zeta potential of the kaolinite particles in the supernatant

The zeta-potential of the kaolinite supernatants in different concentrations of MgCl₂ solutions as a function of MF dosage after 18 hrs-settling is shown in Figure 3.6.

In Milli-Q water, due to the anomalous surface conductance, the zeta potential results were not shown in Figure 3.6. Zeta potential in each MgCl_2 concentration maintained at a stable value at various MF dosages, thus the effect of addition of MF was insignificant in this case. From 0.01 M to 0.1 M, by increasing MgCl_2 concentration, the zeta potential decreased from -15 mV to -8 mV. Similar trend of zeta potential of the kaolinite particles in supernatant in CaCl_2 system have been reported by Mpofu et al⁶⁰ in 2003. By further increasing MgCl_2 concentration from 0.1 M to 1 M, the zeta potential was converted from -8 mV to +3 mV, which could be explained by the excess of hydrolyzed magnesium ions.⁸⁴

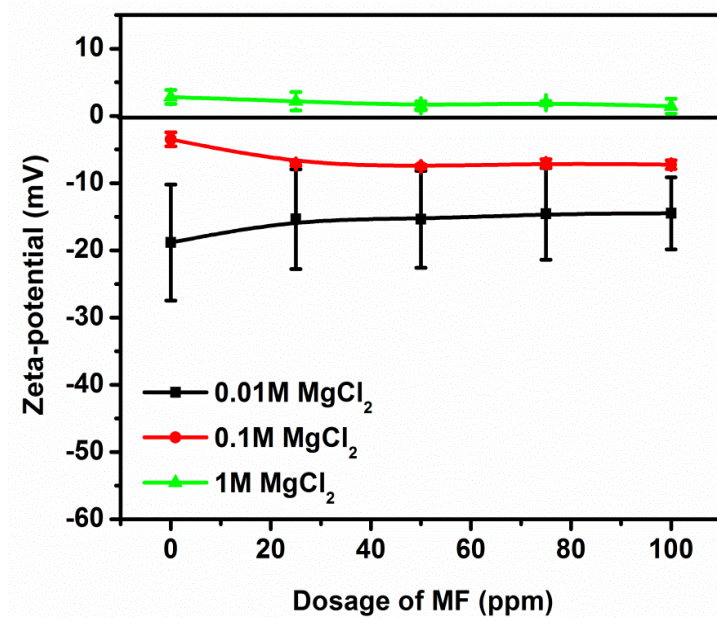
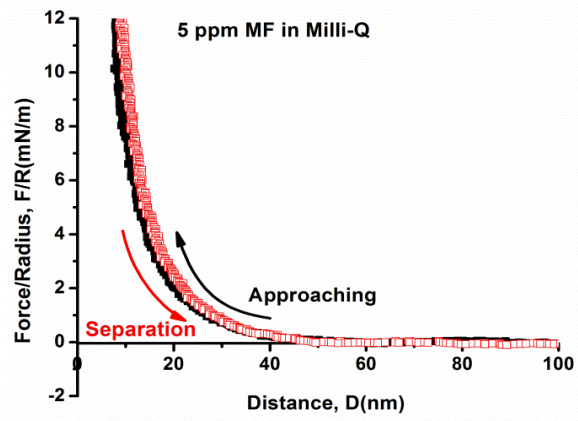


Figure 3.6. The zeta potential values of kaolinite particles in the supernatant of 5 wt% solid kaolinite suspension prepared with 0.01 M (■), 0.1 M (●) and 1 M (▲) MgCl_2 solution after 18 hrs-settling at pH 7.5 as a function of MF dosage.

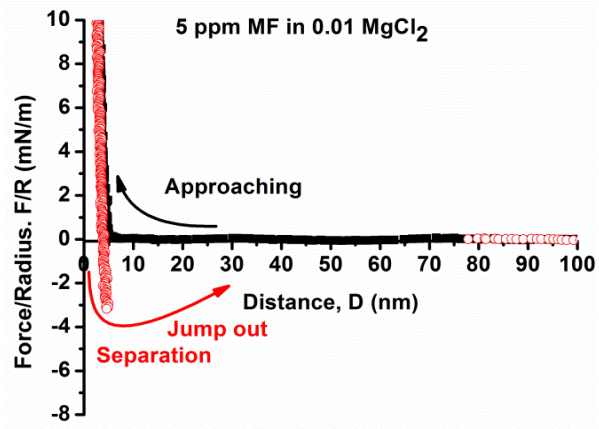
3.3.2 Interactions between MF and model clay surfaces measured by SFA

3.3.2.1 Interactions between mica surfaces with MF in between

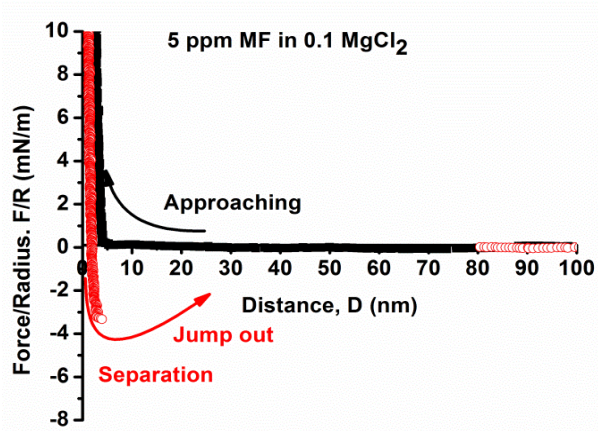
The force profiles between two mica surfaces with 5 ppm MF in Milli-Q and in MgCl_2 solutions with various concentrations after 30 mins of incubation are shown in Figure 3.7. Figure 3.7 (a) shows that pure repulsion existed between mica surfaces in 5 ppm MF Milli-Q solution during both approaching and separation processes. This might be due to the steric repulsion between MF chains absorbed on the opposing mica surfaces. In Milli-Q water, electrostatic repulsive force between negatively charged segments of MF led to more extended and stretched MF chains absorbed on the mica, which hindered the further approaching of the two surfaces. When the two mica surfaces were approaching each other, repulsion force was generated when the distance between two surfaces was around 60.0 nm and confined polymer thickness was ~ 7.8 nm. Figure 3.7 (b), (c) and (d) indicate that existence of MgCl_2 influenced the interaction force between mica surfaces. For the 0.01 M MgCl_2 case, attraction was observed during the separation process. Compared with the results in Milli-Q water, the initial force distance decreased to ~ 20 nm and confined polymer thickness was reduced to 2.2 nm. Further increasing the MgCl_2 concentration to 1 M, both initial force distance and confined polymer thickness decreased gradually, meanwhile, attraction during separation process in each condition increased from 3.2 mN/m to 7.1 mN/m.



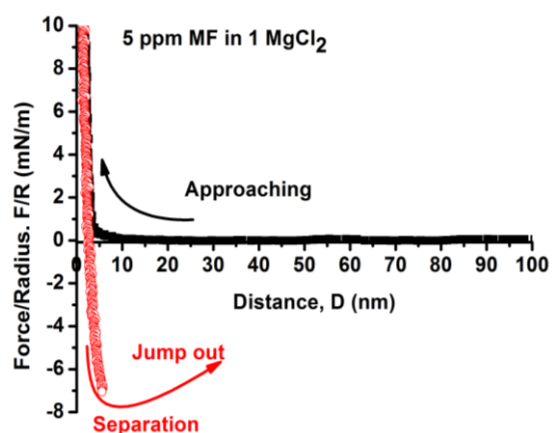
(a)



(b)



(c)



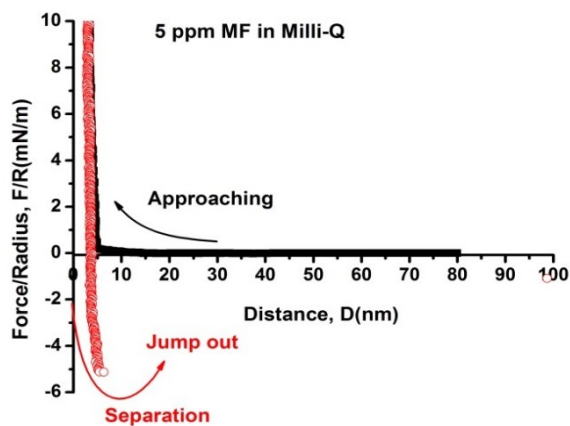
(d)

Figure 3.7. The normalized force-distance profiles between two mica surfaces in 5 ppm MF prepared by (a) Milli-Q water, (b) 0.01 M MgCl_2 ; (c) 0.1 M MgCl_2 and (d) 1 M MgCl_2 after 30 min incubation at pH 7.5.

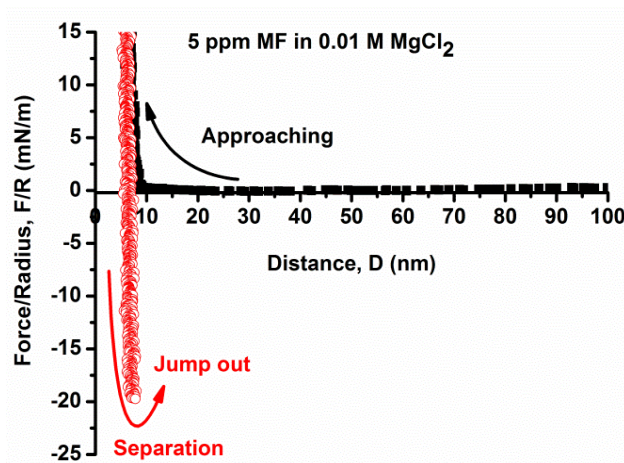
3.2.2.2 Interactions between alumina surfaces with MF in between

The force-distance profiles between alumina surfaces in MF solutions are shown in Figure 3.8. Adhesion force between alumina surfaces in MF/Milli-Q water solution could be mainly due to the electrostatic attractive force between positive charged alumina surface and negatively charged MF segments. In 0.01 M MgCl_2 solution, a stronger attraction force was observed (Figure 3.8 (b)). The adhesion force then decreased from $F_{ad}/R \sim -20$ mN/m to $F_{ad}/R \sim -16$ mN/m between two alumina surfaces in 5 ppm MF with increasing MgCl_2 concentration from 0.01 M to 1 M. Meanwhile, the confine polymer thickness also decreased from 9.5nm to 3.5 nm. It is noted that the MF molecules and Mg^{2+} contributed to the attraction between the alumina surfaces from several aspects: (1) electrostatic interaction between negatively charged $-\text{COO}^-$ groups and positively charged alumina surfaces as well as hydrogen bonding between confined MF molecules and alumina surfaces leading to bridging attraction, (2) interaction between Mg^{2+} and -

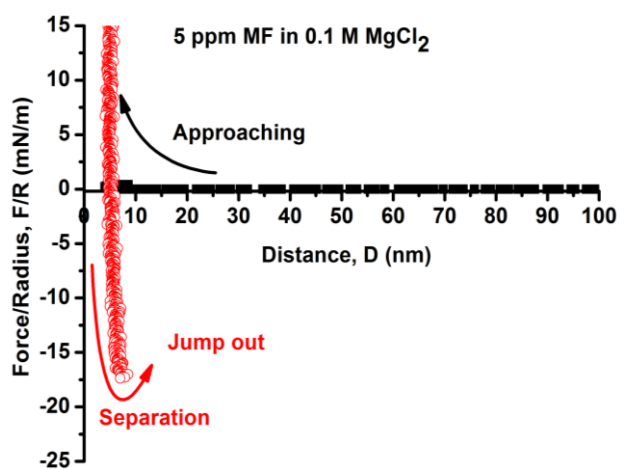
COO⁻ groups on adsorbed MF chains resulting in the bridging attraction between -COO⁻ groups. The adhesion force decreasing tendency could be due to acrylate-Mg-acrylate complexation, leaving less unbonded acrylate groups adsorbing on alumina. Compared with the adhesion force between silica surfaces, apparently, Mg²⁺ has a more significant impact on enhancing bridging adhesion between MF and alumina surface. The key parameters (confined polymer thickness, initial interaction distance, adhesive force) obtained under all conditions in both cases (mica and alumina) are summarized in Table 3.2.



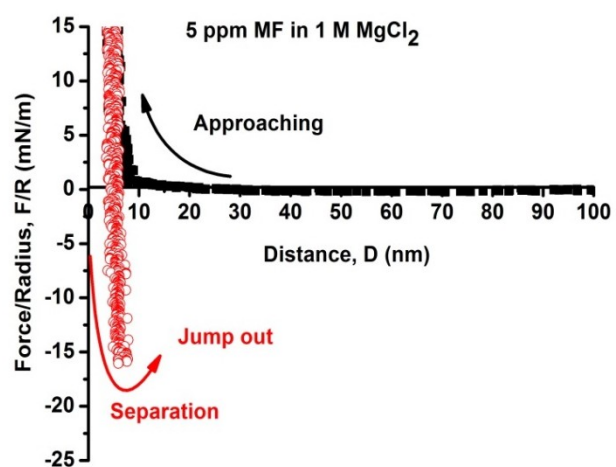
(a)



(b)



(c)



(d)

Figure 3.8. The normalized force-distance profiles between two alumina surfaces in 5 ppm MF prepared by (a) Milli-Q water; (b) 0.01 M; (c) 0.1 M and (d) 1 M MgCl_2 after 30 min incubation at pH 7.5.

Table 3.2. Key parameters of force-distance profil results.

Surfaces	Solution	Confined polymer thickness (nm)	Initial force distance (nm)	Adhesive force (mN/m)
Mica-mica	Milli-Q	7.8±0.9	60.0±4.9	N/A
	0.01 M MgCl ₂	2.2±0.4	20.1±3.9	-3.2±0.1
	0.1 M MgCl ₂	1.5±0.7	19.2±1.7	-3.6±0.8
	1 M MgCl ₂	1.3±0.4	18.9±1.9	-7.1±0.1
Alumina-alumina	Milli-Q	2.8±0.1	6.6±0.4	-5.6±0.4
	0.01 M MgCl ₂	9.5±0.4	12.4±0.7	-20.5±1.6
	0.1 M MgCl ₂	4.3±0.2	10.8±1.3	-17.4±0.4
	1 M MgCl ₂	3.9±0.2	9.5±5.6	-16.1±0.5

The adhesion measured above between two curved mica surfaces and between two curved alumina surfaces in the presence of MF in different MgCl₂ concentrations could be correlated to the adhesion energy between two flat substrates via the Equation shown below. Based on the *Johnson-Kendall-Roberts (JKR) theory*^{85, 86}, W_{ad} is the adhesion energy and F_{ad}/R is the normalized adhesion force from SFA measurements.

$$W_{ad} = -\frac{F_{ad}}{1.5\pi R}$$

The adhesion energy between two curved mica surfaces and between two curved alumina surfaces in the presence of MF with various concentrations MgCl₂ is summarized in Figure 3.9.

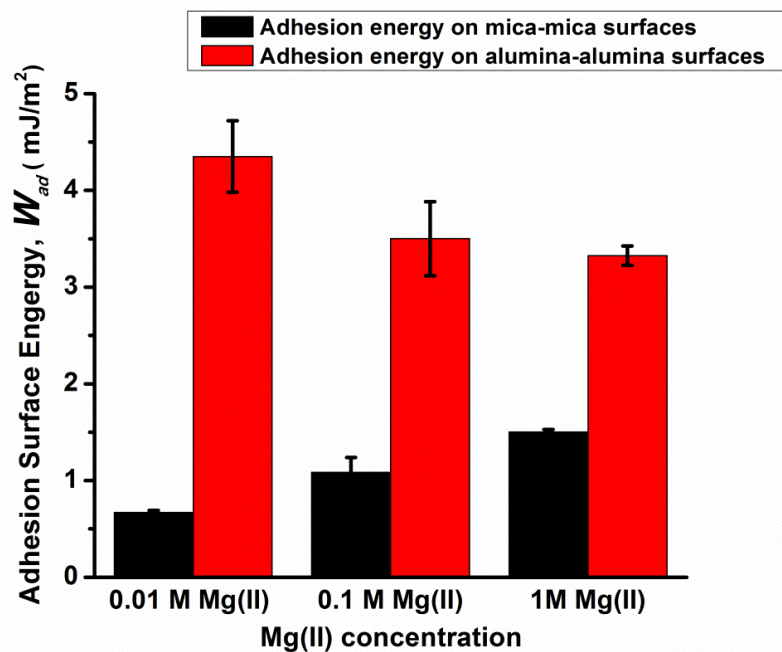


Figure 3.9. Adhesion energy between mica surfaces and alumina surfaces in MF solution in the presence of 0.01 M, 0.1 M and 1 M $MgCl_2$ solutions.

Figure 3.9 shows that the adhesion for mica-mica with MF in between increased with increasing the concentration of Mg^{2+} . For alumina-alumina case, the adhesion energy decreased with increasing the divalent cation concentrations, which might be due to the weakened electrostatic attraction between positively charged alumina and negatively charged MF at high salt concentrations.

3.3.3 Conformation measurements by the dynamic light scattering (DLS)

To understand the impacts of Mg^{2+} on the conformation of MF molecules and its correlation with the force measurements results, the hydrodynamic radii (R_H) of MF molecules in $MgCl_2$ solutions were measured, as shown in Table 3.3. It was found that the R_H of MF molecules decreased from 364 nm in Milli-Q water to 60 nm in 0.01 M

MgCl₂ solution. By further increasing the salt concentration from 0.01 M to 0.1 M and 1 M led to a growth of R_H from 60 nm to 92 nm. To better understand the polymer structure changing, the gyration radius $R_g=101.3$ nm and Flory radius $R_f = 474$ nm of MF were calculated according to the following theoretical equations.

$$R_g = l \times \sqrt{\frac{M_n / M_0}{6}}$$

R_g is the effective polymer radius in ideal solvent and there is no interaction between each segment. R_f is used to describe the polymer radius in good solvent, in which inner-segment repulsion leads to the expanded structure. In Milli-Q water, the hydrodynamic radius located between R_g and R_f , suggesting Milli-Q water is a good solvent for MF and the electrostatic repulsion between carboxylate groups increased the polymer radius. This repulsion, then, was screened because of the electrostatic attraction between Mg²⁺ and acrylate groups by adding MgCl₂, which could explain the decrease of radius from 364 nm to 60 nm. With higher salt concentration, by compressing the electrostatic repulsion force, inter-segment hydrogen bonding was favorable. Synergistic effect of electrostatic force and hydrogen bonding resulted in the aggregation of MF in high salt solution.

Table 3.3. Hydrodynamic radii of MF in solutions of different MgCl₂ concentration.

Salt concentration	Hydrodynamic radius (R_H , nm)
Milli-Q water	364.0
0.01 M MgCl ₂	60.0
0.1 M MgCl ₂	68.0
1 M MgCl ₂	92.0

3.3.4 Adsorption of MF on model clay surface measured by QCM-D

The change of frequency and dissipation of MF adsorption on silica sensors are shown in Figure 3.10 to Figure 3.13. From Figure 3.10, it is easy to find that MF did not show good adsorption ability on the silica sensor in Milli-Q water. In MgCl₂ solution, adsorption of MF on silica sensors was observed in all three concentrations. The frequency change associated with the adsorption of MF on silica changed from -13 Hz to -17 Hz when increasing the MgCl₂ concentration from 0.01 M to 1 M. In 0.01 M MgCl₂ solution, a relatively larger increase in dissipation shift ($\Delta D \sim 5.8 \times 10^{-6}$) indicated the formation of loose layer of MF polymer on the silica surface. In the solution with high ion strength, the dissipation shift decreased to 2.6×10^{-6} (Figure 3.13), which suggested that a solid MF layer was formed in 1M MgCl₂ solution and it may due to the abundant anchoring bridging sites between MF and the sensor surfaces⁵⁴. However, interestingly, the adsorption of MF did not reach equilibrium even after 8000 seconds of

test for all the three MgCl_2 concentrations studied here. In order to remove the unbounded MF, the sensor was rinsed with the background solution.

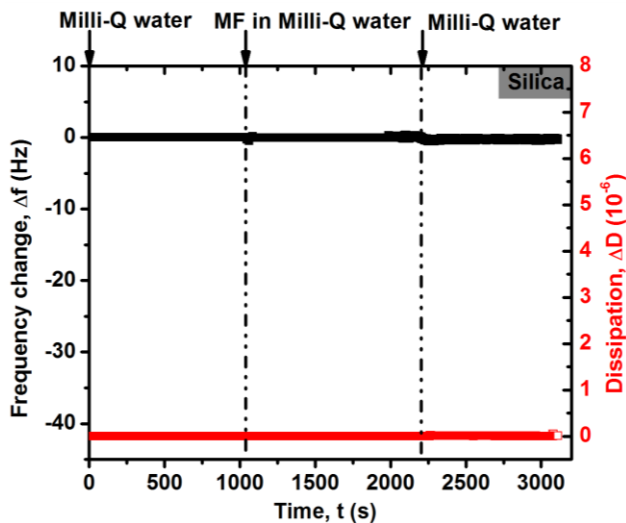


Figure 3.10. Time course of Δf and ΔD for the MF adsorption on silica sensor in Milli-Q water.

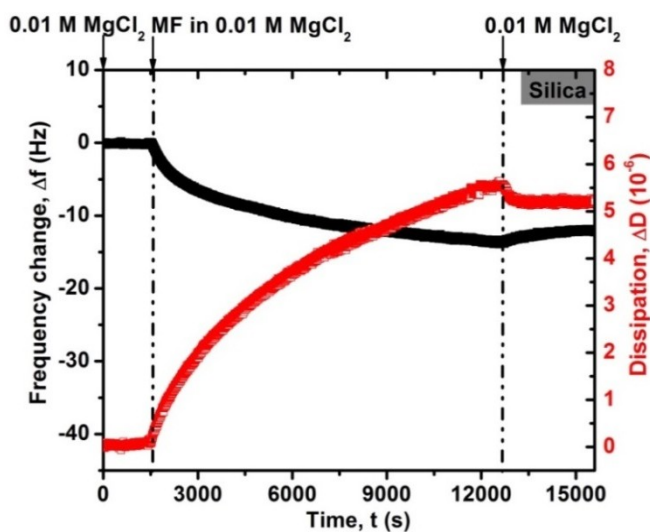


Figure 3.11. Time course of Δf and ΔD for the MF adsorption on silica sensor in 0.01 M MgCl_2 .

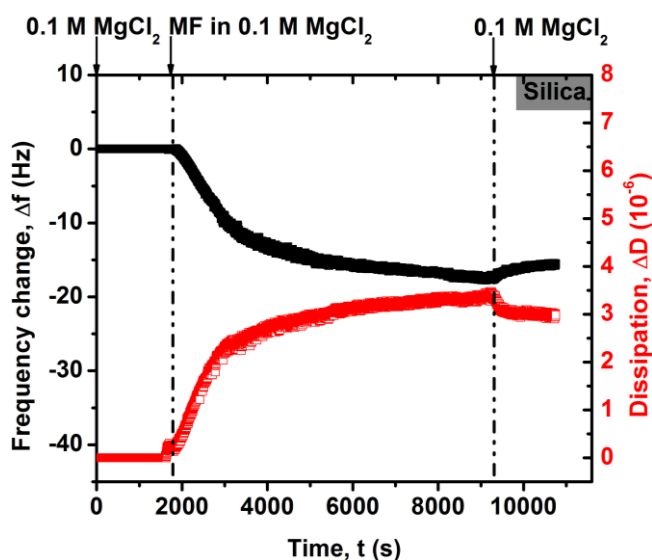


Figure 3.12. Time course of Δf and ΔD for the MF adsorption on silica sensor in 0.1 M MgCl_2 .

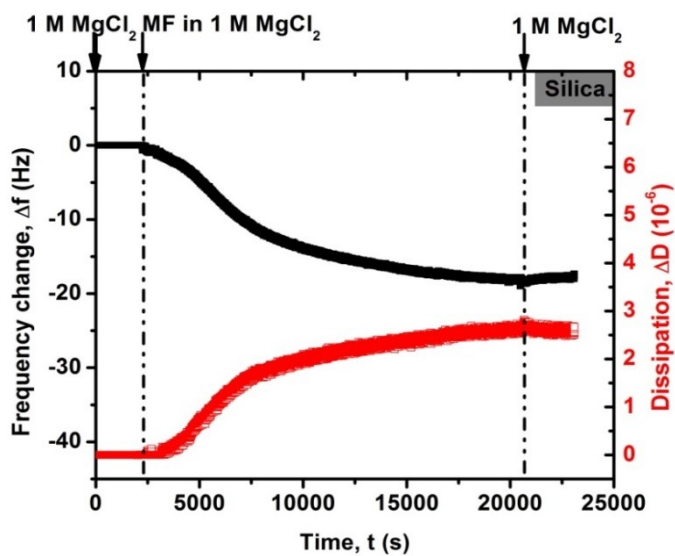


Figure 3.13. Time course of Δf and ΔD for the MF adsorption on silica sensor in 1 M MgCl_2 .

Dissipation and frequency changes after adsorption of MF on the alumina sensors in Milli-Q and MgCl_2 solutions are shown in Figure 3.14 to Figure 3.17. The frequency shift stayed around -25 Hz when MgCl_2 concentration increased from 0.01 M to 1 M. The equilibrium (plateau) of both frequency and dissipation shift for the alumina sensor

case could be achieved at the beginning of the adsorption process which did not change significantly upon rinsing with the background solution, which was quite different with the results for the silica sensors (Figure 3.15 to Figure 3.17). The QCM-D results for the adsorption of MF in MgCl_2 solutions suggested that the adsorption between MF molecules and alumina surface were relatively more stable and rapid than that between MF molecules and silica surface. The QCM-D results suggested that interaction between MF molecules and silica surface. The QCM-D results suggested that interaction between MF molecules and silica was weaker than that between MF and alumina.

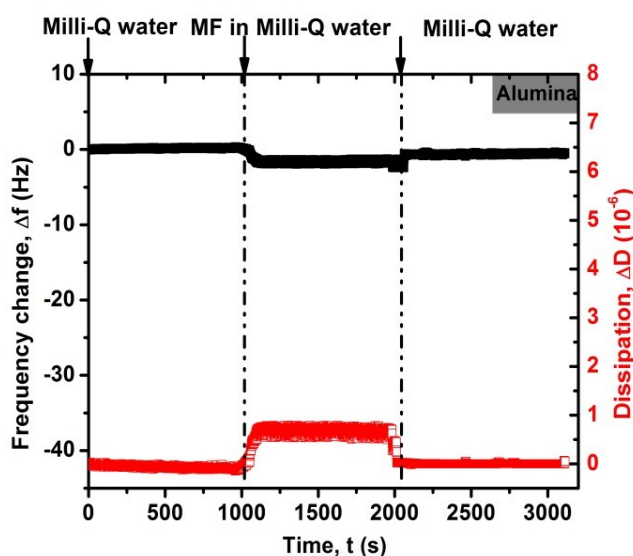


Figure 3.14. Time course of Δf and ΔD for the MF adsorption on alumina sensor in Milli-Q water.

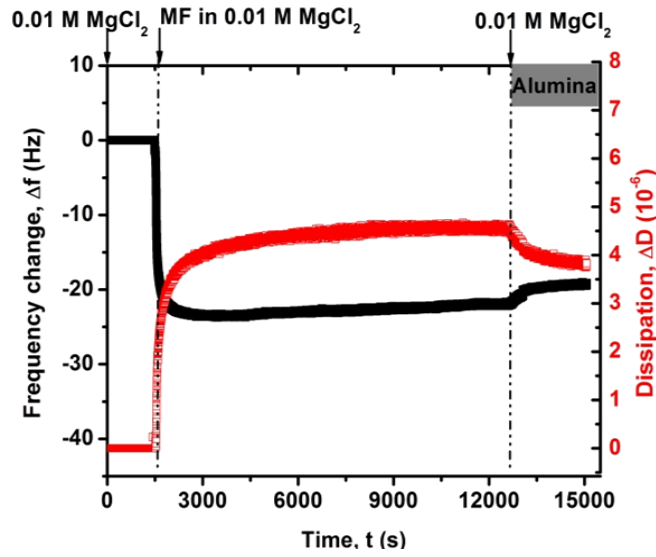


Figure 3.15. Time course of Δf and ΔD for the MF adsorption on alumina sensor in 0.01 M MgCl_2 .

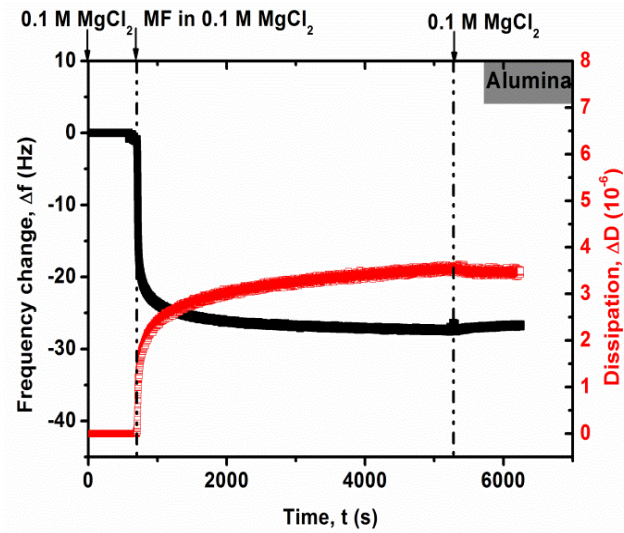
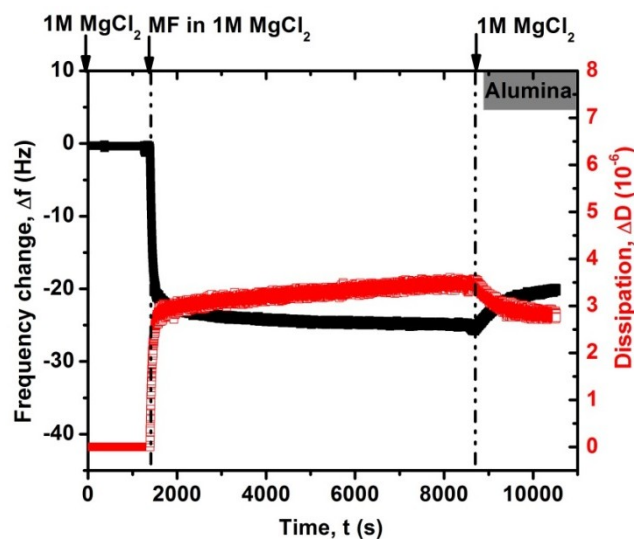


Figure 3.16. Time course of Δf and ΔD for the MF adsorption on alumina sensor in 0.1 M MgCl_2 .



(d)

Figure 3.17. Time course of Δf and ΔD for the MF adsorption on alumina sensor in 1 M MgCl_2 .

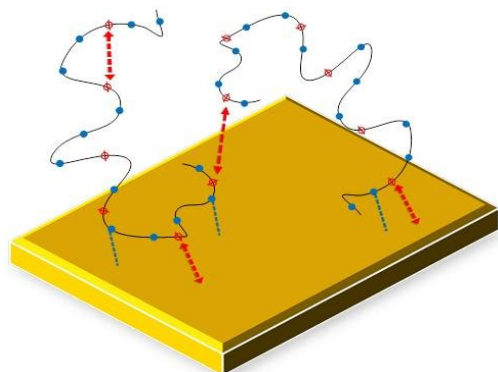
3.3.5 The mechanism of interactions between MF and model clay particle (surface)

Based on all the results obtained above, the interactions between MF and kaolinite surfaces in various Mg^{2+} concentrations are proposed. The isoelectric points for silica and alumina are 1.7-3.5⁸⁷ and 8-9⁸⁸ respectively. Thus, at pH 7.5, silica and alumina surfaces carry opposite charges. The charge difference of these two surfaces makes great influence on flocculant-particle surface interactions. In Milli-Q water, MF chain structures on both silica surface and alumina surface are shown in Figure 3.18 (a) and (b). On the silica surface, without adding MgCl_2 , the MF chain was stretched out due to the inter-segment electrostatic repulsion and chain-chain steric repulsion, which could explain the repulsive forces detected during both approaching and separation in the SFA test (Figure 3.7(a)). The QCM-D results also indicated there was no adsorption of MF on the silica surface in Milli-Q water. As MgCl_2 added into the system, electrostatic-layers around charged particles and MF chains were compressed. Mg^{2+} could combine

carboxylate groups to form metal complex, which helped reduce inter-segment repulsion and compressed the polymer chains as shown in Figure 3.18(c). Hence, on silica surface, as Mg^{2+} concentration increased, the adhesion force of SFA increased and confined polymer thickness decreased. Interestingly, QCM-D results showed that it took long time for MF adsorption on the silica surface in Mg^{2+} to reach equilibrium (Figure 3.11, Figure 3.12 and Figure 3.13). We attribute this to the stable complexation of acrylate-Mg-acrylate and it is supposed that the exchanging between dissociative acrylate groups and bonded acrylate groups took place in a much slow way.

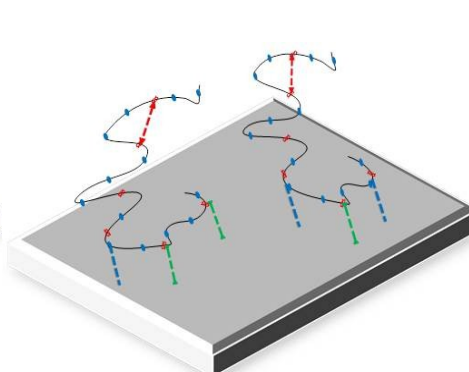
However, for the alumina surface, in Milli-Q water, the measured attraction force (Figure 3.8(a)) came from the electrostatic attraction and hydrogen bonding between alumina surface and amide groups, acrylate groups. When compressing the two alumina surfaces in the SFA test, the unbonded acrylate groups could attach on both alumina surfaces by electrostatic attraction and hydrogen bonding (Figure 3.18 (b)), which led to more compressed MF chains and larger adhesive forces on the surfaces. However, in $MgCl_2$ solutions, there existed an electrostatic-attraction competition between alumina-acrylate bonding and Mg-acrylate bonding. In saline polymer stock solution, acrylate segments were surrounded by Mg^{2+} and formed acrylate-Mg-acrylate complex. As introducing MF stock solution to alumina surfaces, some acrylate groups adsorbed on the alumina surfaces, the others, bonded with Mg^{2+} , might generate electrostatic repulsion against the alumina surface, which inhibited electrostatic attraction between alumina surfaces and led to a decreasing tendency on adhesion forces (Figure 3.8(b), (c), (d)). As Mg^{2+} concentration increased, polymer chains was further compressed and large quantity

Mg^{2+} increased the stability of acrylate-Mg-acrylate complex, leaving less unbonded acrylate groups adsorbing on alumina.



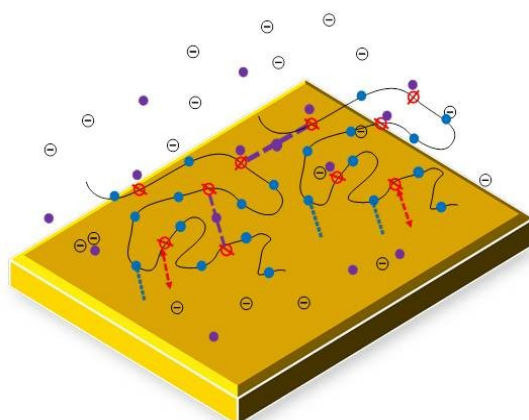
In Milli-Q water

(a)



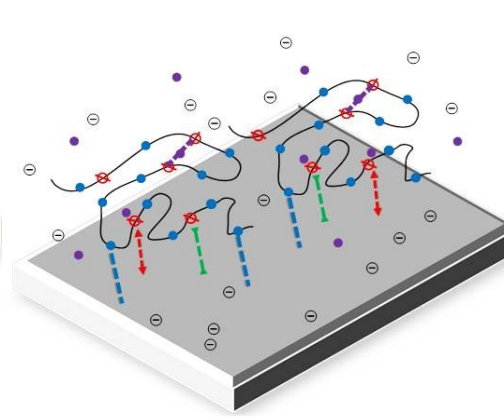
In Milli-Q water

(b)



In $MgCl_2/CaCl_2$

(c)



In $MgCl_2/CaCl_2$

(d)

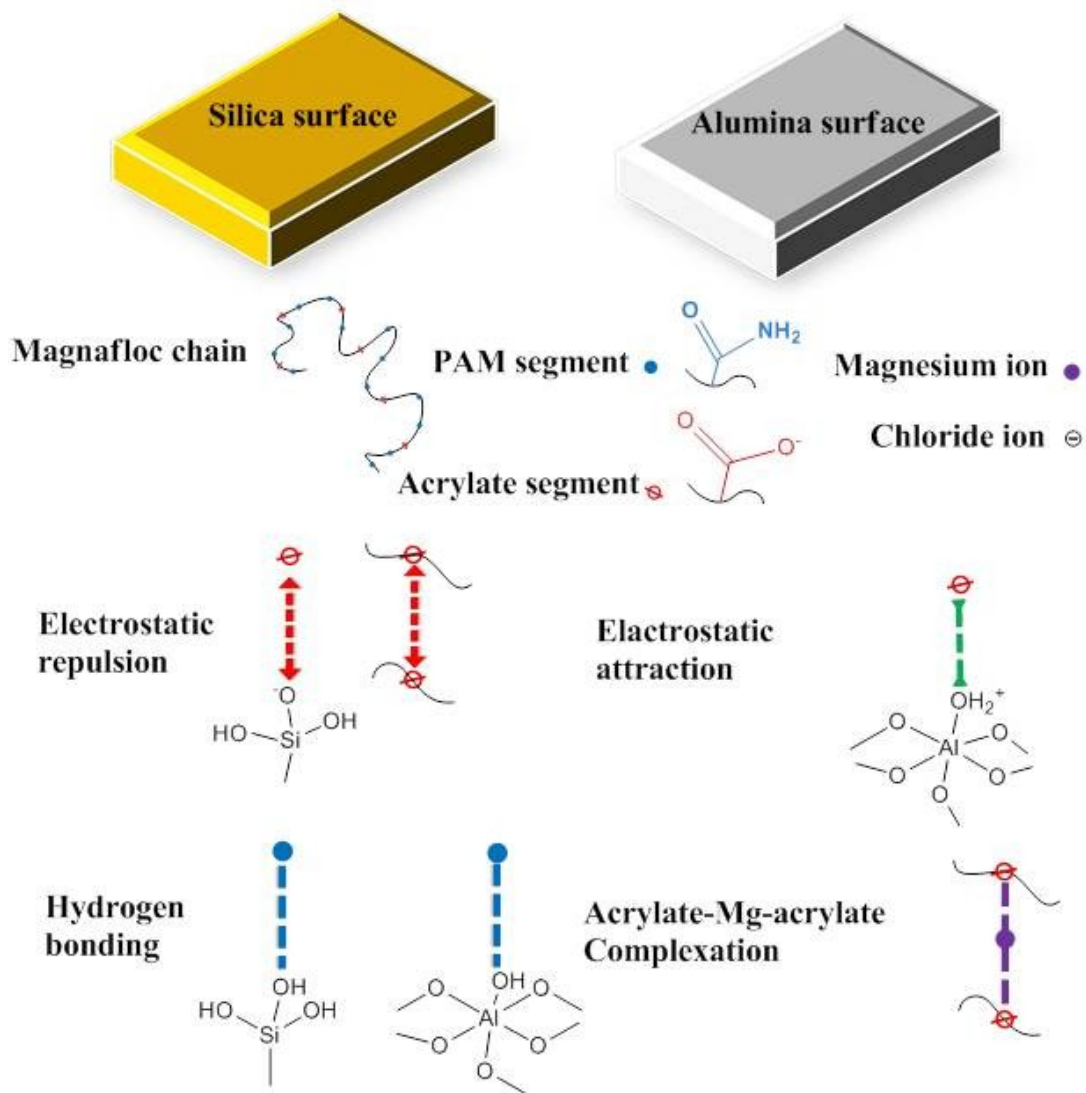


Figure 3.18. Schematic of the interaction of MF with silica and alumina surfaces in Milli-Q and MgCl_2 solution.

3.4 Conclusion

In this study, the influence of MgCl_2 on the settling performance of the kaolinite suspension treated by MF has been elucidated by typical settling characterization methods (ISR, turbidity) and state-of-the-art techniques (SFA, QCM-D and Zeta Nano Sizer). Interactions between MF chains and different faces of model clay surfaces have

been exclusively investigated on both silica/mica and alumina surfaces. Settling rate was strongly related to MgCl_2 concentration and MF dosage. In MgCl_2 solution, the electrostatic-double layers of charged particles have been heavily compressed and the structure of electrolytes was also affected, facilitating the formation of acrylate-Mg-acrylate complex and hydrogen bonding, which enhanced the kaolinite suspension settling. By investigating the adsorption behavior and the interactions of MF on silica/mica and alumina surfaces, the differences on the adsorption and adhesions were mainly due to MgCl_2 concentration, polymer structure and the surface charge properties.

Chapter 4 Molecular and Surface Interactions between Chitosan-g-Polyacrylamide Polymer Flocculant and Kaolinite Particles: Impact of Salinity¹

4.1 Introduction

Interactions between polymer chains and colloidal particles have attracted much attention over the past three decades which lead to a broad range of applications of polymers, colloids or their mixtures. Among these applications, flocculation by polymer flocculants^{13, 16} has been continuously exerting its profound impact on recycling water from mineral⁸⁹ and oil sands tailings⁹⁰ water treatment. Much efforts have been dedicated to the optimization of flocculation performance and settling of various tailings or colloidal suspensions using polymer flocculants, particularly on the effects of polymer type^{91, 92}, molecular weight⁹³, ionization degree⁹⁴ of the flocculant, pH^{65, 95} and chemical composition⁹⁶ of the tailings. Due to a wide variety of ions and possible organic wastes accumulated during mineral or oil processing and water reclamation, the water chemistry

¹ A version of this chapter has been submitted for publication. S. Wang, L. Zhang, B. Yan, H. Xu, Q. Liu, H. Zeng, 2014, Water Research. (Submitted)

and solution properties (e.g. salinity) are normally extremely complex in these industrial tailings suspensions⁸⁴, which significantly influences surface properties of solid particles (e.g. surface charges) and molecular behaviours (e.g. conformation) of polymers⁹⁷. It is of both fundamental and practical importance to investigate how solution salinity affects the interactions between polymer flocculants and solid colloids and the flocculation performance.

Recently, chitosan, as the second abundant natural polysaccharide⁹⁸, has attracted considerable attention in water treatments because of its outstanding biodegradability⁹⁹,¹⁰⁰ and excellent coagulation/flocculation abilities¹⁰¹ to various effluents such as wastewater from milk processing plant¹⁰², bacterial suspensions^{103, 104}, olive oil wastewater^{105, 106}, and raw drinking water¹⁰⁷. However, because of the intermolecular and intramolecular hydrogen bonding, chitosan can only be soluble under acidic conditions¹⁰⁸, which greatly limits its applications in tailings water treatment. To improve the solubility of chitosan and extend its application to tailings water treatment, polyacrylamide (PAM), a widely used commercial flocculant,¹⁵ was grafted to chitosan (chitosan-g-PAM or chi-g-PAM)¹⁰⁹. The flocculation behaviors of chi-g-PAM based flocculant were tested on various types of solid suspensions such as kaolin, iron ore, silica and bentonite, and the

effects of pH and grafting percentage of PAM were also investigated,¹¹⁰⁻¹¹² which show that chi-g-PAM is an excellent polymer flocculant on these solid suspensions. No systematic study has been reported how solution salinity affects the flocculation performance of chi-g-PAM and the basic intermolecular and surface interaction mechanism between chi-g-PAM polymer and solid particles, which is of both fundamental and practical importance due to the complex salinity properties of industrial tailings.

In this work, chi-g-PAM was synthesized and the effect of salinity (i.e. addition of NaCl and CaCl₂) on the flocculation performance of chi-g-PAM on kaolinite suspension was investigated via the initial settling rate (ISR) and turbidity measurements. The molecular interactions and adsorption of chi-g-PAM on model solid particles and surfaces were investigated by zeta potential measurements, quartz crystal microbalance with dissipation (QCM-D), surface forces apparatus (SFA) and atomic force microscope (AFM).

4.2 Materials and Methods

4.2.1 Materials

Chitosan with molecular weight 600,000 – 800,000 g/mol and acrylamide (AM) were purchased from Acros Organics and used as received. Ammonium Cerium Nitrate (Ce (IV)) obtained from Acros Organics was used as the initiator. Kaolinite of high-purity (Acros Organics) was used for the preparation of model clay suspension or so-called model tailings with particle size range ~ 1.45 to $22.9 \mu\text{m}$, $\rho \sim 2.60 \text{ kg/dm}^3$, $D_{50} \sim 5.75 \mu\text{m}$ (D_{50} indicates 50 wt% of the particles with size below the corresponding diameter). Polyacrylamide (Sigma-Aldrich) was used for comparison experiment. NaCl and CaCl_2 (Certified ACS, Fisher Scientific) were used for the preparation of the salt solutions in model tailings. Acetic acid (Certified ACS, Fisher Scientific), hydrochloric acid (Certified ACS, Fisher Scientific) and Milli-Q water (resistivity = $18.2 \text{ M}\Omega\cdot\text{cm}$) were used for sample preparation and chemical dissolving as needed. NaOH and HCl (Certified ACS, Fisher Scientific) were used as the pH modifiers. All reagents were analytical grade and used as received. Silica surface and alumina surface sensors were purchased from Q-sense (Q-sense, Swedish).

4.2.2 Synthesis of chi-g-PAM

The graft copolymerization of PAM onto chitosan was carried out in a 250 mL three necked round bottom flask. The flask was fixed on a thermo-stirring device for controlling mixing and reaction temperature (i.e. 50 °C). Desired amount of chitosan was first dissolved in 1 wt% acetic acid at room temperature with continuously stirring. The whole system was purged with Argon for 30 min to remove the dissolved oxygen. Then freshly prepared Ce (IV)/water solution was injected into the above solution to generate primary radicals on chitosan backbone for further PAM grafting. After 15 min reaction, acrylamide was then added into the above solution to start the polymerization. The reaction was allowed to continue for 3 hours. Eventually, polymerization was stopped and the products were purified three times in acetone and dried in a vacuum vessel for 48 hours.

4.2.3 Polymer characterization

The Fourier transform infrared (FTIR) spectra of chi-g-PAM were obtained using Nicolet iS50 FT-IR (Thermo Scientific). The molecular weight of the chi-g-PAM was determined using Zetasizer Nano (Malvern Instruments Ltd., UK) by employing Static

Light Scattering (SLS). The effect of pH on solubility of chitosan, PAM and chitosan mixture and as-prepared chi-g-PAM was tested on a pH range of 5 to 11.

4.2.4 Flocculation experiments

The flocculation experiments were conducted based on a standard procedure reported elsewhere^{75, 113}. 5 wt % kaolinite suspensions were prepared in Milli-Q water or aqueous solutions with 0.01, 0.1 and 1 M NaCl or CaCl₂ in a 2 L beaker. The suspensions were kept under stirring overnight to assist the dispersion of the particles. After adjusting the suspension pH ~7.0, 90 mL slurry sample was collected under agitation at 300 rpm and decanted in a 250 mL standard beaker. The mass of the slurry in each beaker was monitored by a balance for polymer dosage calculation. After sampling, the kaolinite suspension was agitated under 600 rpm for 2 mins and then chi-g-PAM was added under agitation at 300 rpm in 1 min. The agitation was stopped immediately and the whole solution was transferred into a 100 mL graduate cylinder (Fisher Class B Mixing Cylinders, Fisher, US) to evaluate the settling performance. The cylinder was inverted five times and the mudline (defined as the interface between suspensions and sediments) and settling time were monitored to obtain the settling curves. The initial settling ratio (ISR) was defined as the initial slope of the settling curve^{75, 113}. After

settling for 18 hrs, supernatant of each sample was collected to measure the turbidity and zeta potential by Micro-100 Turbidity Meter (Fisher, US) and zeta potential analyzer (Zetasizer Nano, Malvern, UK), respectively.

4.2.5 Polymer adsorption test by QCM-D

Polymer adsorption experiments were conducted using a QCM-D E4 system (Q-sense, Sweden). Silica and alumina QCM-D sensors were used as model surfaces to mimic the basal plane and edge (viz. silica tetrahedral face and *alumina* octahedral face) of kaolinite particles.²⁸ The polymer stock solutions were adjusted to pH ~7.0 before the experiments at room temperature. Baseline was established by injecting background solution (pure 0.01, 0.1, or 1 M NaCl or CaCl₂ solution) into the QCM-D chamber where Δf and ΔD were defined as zero. Then the 500 ppm polymer solution was pumped into the QCM-D chamber at flow rate of 150 $\mu\text{L}/\text{min}$. After the Δf and ΔD became stable, the pure background solution was injected into the chamber to remove any unbounded or loosely bounded polymers. In this study, the Voigt viscoelastic model³⁰ of Q-tool software was used to correlate the frequency and dissipation as a function of time to the mass of the adsorbed polymer layer. Based on the Voigt model, for a viscoelastic layer on quartz slide immersed in a bulk Newtonian fluid, Equations 4.1 to 4.3 hold, where Δf

is frequency change, ΔD is dissipation change, ρ is density, h is thickness, η is viscosity, μ is shear modulus and ω is circular frequency.¹¹⁴

$$\Delta f \approx -\frac{1}{2\pi\rho_0 h_0} \left\{ \frac{\eta_2}{\delta_2} + \left[h_1 \rho_1 \omega - 2h_1 \left(\frac{\eta_2}{\delta_2} \right)^2 \frac{\eta_1 \omega^2}{\mu_1^2 + \omega^2 \eta_1^2} \right] \right\} \quad (4.1)$$

$$\Delta D \approx \frac{1}{2\pi f \rho_0 h_0} \left\{ \frac{\eta_2}{\delta_2} + \left[2h_1 \left(\frac{\eta_2}{\delta_2} \right)^2 \frac{\eta_1 \omega^2}{\mu_1^2 + \omega^2 \eta_1^2} \right] \right\} \quad (4.2)$$

$$\delta_2 = \sqrt{\frac{2\eta_2}{\rho_2 \omega}} \quad (4.3)$$

4.2.6 Surface force measurements in aqueous solutions by SFA

SFA has been widely applied for measuring physical forces (e.g. van der Waals interaction, electrostatic interaction) of various materials as a function of absolute separation distance in vapors and liquid media.^{77, 78, 115, 116} SFA was employed in this work to measure the surface interaction between two mica surfaces in chi-g-PAM solutions. The details of SFA setup has been reported elsewhere⁷⁸. Briefly, freshly cleaved mica sheets were first coated with a semi-reflective silver layer for generating fringes of equal chromatic order (FECO) which can be used to determine the surface separation distance D during SFA measurements. The silver-coated mica sheets of the same thickness were then glued on two curved silica disks which were mounted into SFA

chamber in a crossed-cylinder configuration. In a typical normal force measurement, the separation distance $D = 0$ was referred to as the position where the two bare mica surfaces were in contact. 5 ppm of desired chi-g-PAM solution at pH ~ 7.0 was then injected between mica surfaces and incubated for one hour before force measurements.

4.2.7 AFM imaging

The surface morphology of chi-g-PAM adsorbed on mica surfaces under various solution conditions were characterized using an Asylum MFP 3D AFM (Asylum Research Corporate Office, CA, USA). The chi-g-PAM surfaces were prepared by immersing mica substrates in 50 ppm chi-g-PAM stock solutions at pH ~ 7.0 for an adsorption time of ~ 2 hours. Then the surfaces were thoroughly rinsed by Milli-Q water and dried overnight before imaging.

4.3 Results and Discussion

4.3.1 Characterization of chi-g-PAM

The chi-g-PAM (mass ratio 1:5) used in this study was synthesized according to a modified procedure¹¹⁷ as shown in Figure 4.1. To minimize the generation of PAM homopolymer, the initiator, Ce (IV), was introduced first to produce primary radical on

the backbone for 15 min. During this period, Ce (IV) was consumed and further addition of AM monomer was initiated and directly grafted from chitosan backbone. The chemical structure of the polymer was carefully characterized by SLS and FTIR. The SLS measurement shows that the MW of chi-g-PAM significantly increased to 1,840,000 g/mol as compared to the original MW of pure chitosan (with MW of 600,000 – 800,000 g/mol), indicating successful grafting of PAM to chitosan backbones.

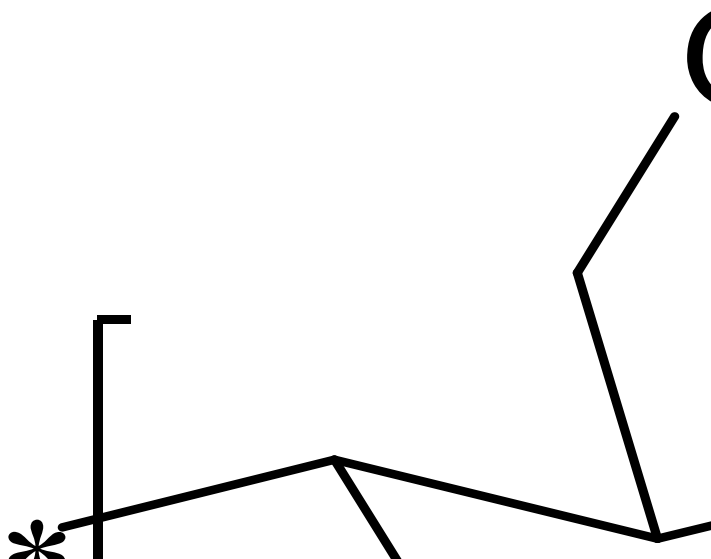


Figure 4.1. The schematic of polymerization process of chi-g-PAM.

The FTIR spectra of chitosan, chi-g-PAM and PAM are shown in Figure 4.2. Figure 4.2 a clearly shows a broad peak at 3363 cm^{-1} , due to the stretching vibrations of O–H and N–H and a small peak at 2850 cm^{-1} assigned to the C–H stretching vibrations from chitosan saccharide groups. Compared to the FTIR spectrum of chitosan, some apparent differences could be observed on the spectrum of chi-g-PAM: a strong absorption peak at 3349 cm^{-1} and a shoulder at around 3200 cm^{-1} attributed to the N–H

stretching vibrations of the primary amide, and two new bands at 1662 and 1619 cm^{-1} due to amide-I and amide-II of PAM (see Figure 4.2 b) ¹¹¹; Meanwhile, the characteristic absorbance bands of polysaccharide at around 1078, 1034 and 1154 cm^{-1} dramatically decreased for the spectrum of chi-g-PAM. Therefore, the above spectrum results confirm the successful synthesis of chi-g-PAM.

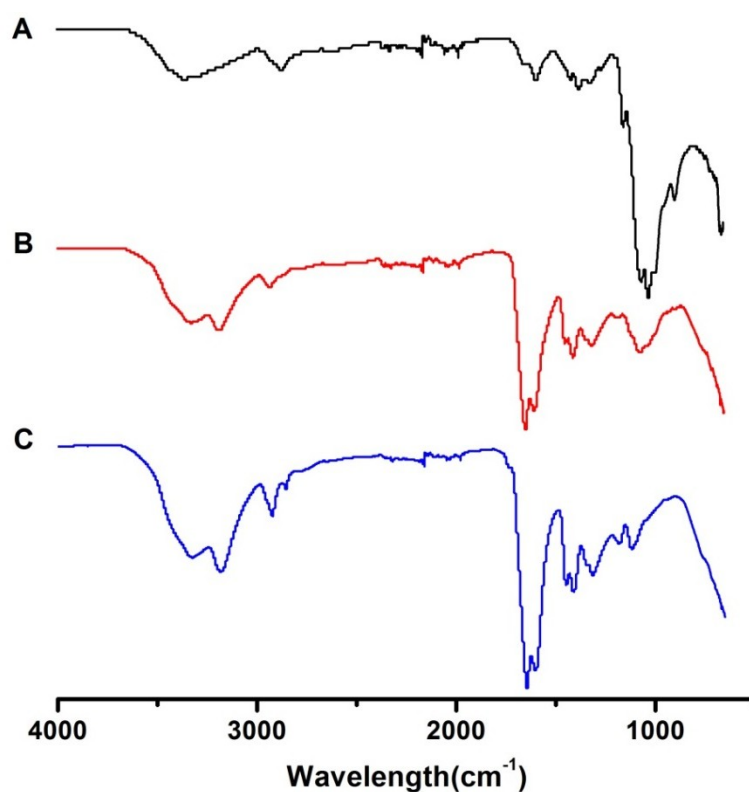
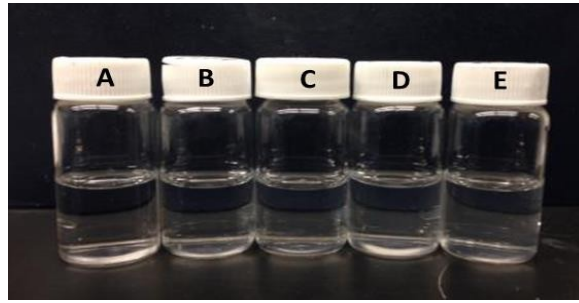


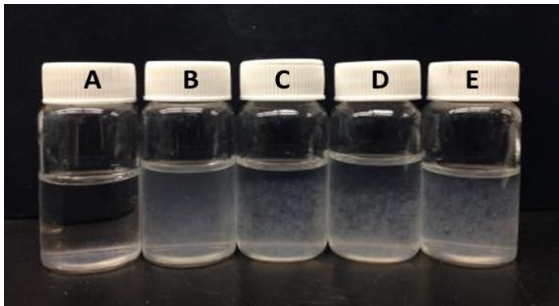
Figure 4.2. FTIR Spectra of (A) chitosan, (B) chi-g-PAM, and (C) PAM.

Significant solubility difference of chitosan, mixture of chitosan and chi-g-PAM, and chi-g-PAM under various pH conditions (shown in Figure 4.3) provides further

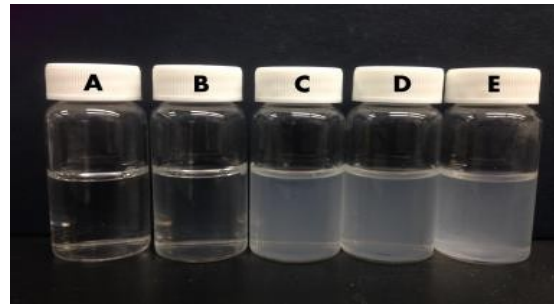
evidence on the successful synthesis of chi-g-PAM. For chitosan, as shown in Figure 4.3 b, it is barely soluble in neutral and basic aqueous solutions: when pH increased from 5 to 7, a turbid solution was observed; when pH further increased to 11, chitosan would totally precipitate out and rapidly settle down. Whereas, for as-prepared chi-g-PAM, it showed excellent solubility in water over the whole pH range tested from pH 5 to 11: a transparent and stable solution was always maintained (Figure 4.3 a). To rule out the possibility that the solubility change observed was due to the interaction of PAM and chitosan, a control experiment was carried out. It was found that the mixture of PAM homopolymer and chitosan showed poor solubility behaviors similar to that of pure chitosan (see Figure 4.3 c). All these results confirm the successful grafting reaction (in Figure 4.1) and indicate that grafting PAM onto chitosan chains could significantly enhance the polymer solubility under a wide pH range. The zeta potential of the synthesized chi-g-PAM at pH ~ 7.0 was measured to be $+0.5 \pm 0.1$ mV, suggesting that chi-g-PAM chains are slightly positively charged which is attributed to the fact that some remaining primary amines on polymer backbones can be ionized at pH ~ 7.0 as the pK_a of chitosan is around 6.3¹¹⁸.



(a) chi-g-PAM



(b) chitosan



(c) chitosan & PAM mixture

Figure 4.3. Pictures on the stability of the solutions of (a) chi-g-PAM, (b) chitosan and (c) chitosan & PAM mixture under various pH conditions: (A) pH 5, (B) pH 7, (C) pH 8, (D) pH 9, and (E) pH 11.

4.3.2 Settling tests using chi-g-PAM

4.3.2.1 Initial settling rate (ISR)

Figure 4.4 shows initial settling rates of 5 wt% kaolinite suspensions in the presence of chi-g-PAM of different dosages in Milli-Q water, NaCl and CaCl₂ solutions at pH ~7.0. The ISR was found to increase with chi-g-PAM dosage from 0 to 100 ppm. Chi-g-PAM exhibited excellent settling ability on kaolinite suspension in Milli-Q water (ISR>120 m/hr at dosage 100 ppm). For the NaCl case, the addition of low concentration

(e.g. 0.01 M) of NaCl could slightly enhance the ISR at low polymer dosage (<50 ppm). In 1 M NaCl solutions, the ISR was found to increase slowly with the polymer dosage and to be much lower than that of the Milli-Q water case, which suggests that high concentration of NaCl could inhibit the flocculation of chi-g-PAM on kaolinite particles. Similar trend was observed for the ISR in CaCl₂ solutions. The ISR in Milli-Q water was higher than that with the addition of 0.01 M to 1 M CaCl₂. It was also found that the ISR for the NaCl case was higher than that of the CaCl₂ case under the same salt concentration and polymer dosage. It is evident from the above results that high concentration of NaCl and CaCl₂ show negative influence on the flocculation behavior of chi-g-PAM settling on kaolinite suspension, while the impact of CaCl₂ is more significant than that of NaCl.

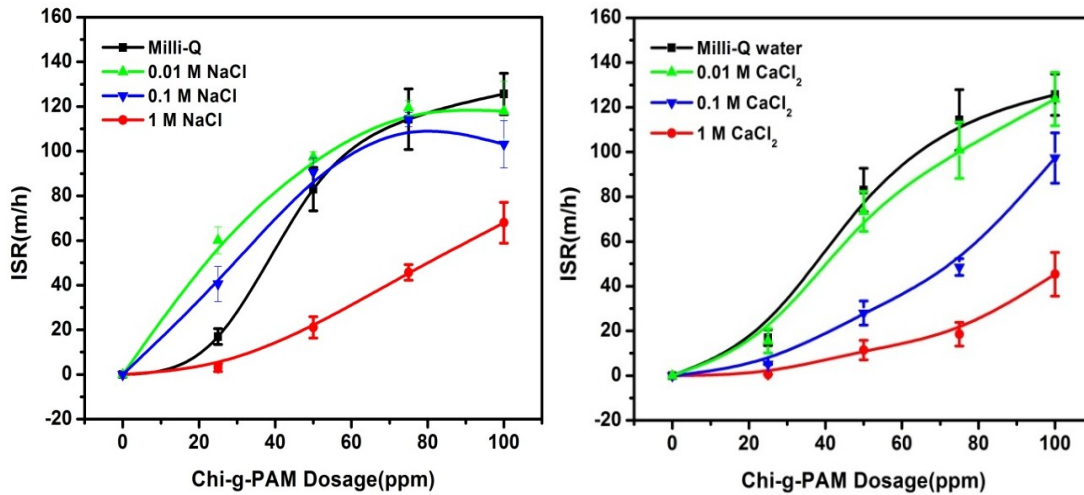


Figure 4.4. ISR for the settling of 5 wt % kaolinite suspension under different dosages of chi-g-PAM in Milli-Q water (■), 0.01 M (▲), 0.1 M (▼) and 1 M (●) of NaCl (left) and CaCl₂ (right) solutions at pH ~7.0

4.3.2.2 Turbidity tests

Figure 4.5 shows the turbidity results of kaolinite supernatant after settling for 18 hours. For the Milli-Q water case, the turbidity of kaolinite suspension without the addition of chi-g-PAM was 370 NTU, and it decreased with increasing the polymer dosage, dropping to 130 NTU at 100 ppm. In the presence of NaCl and CaCl₂, the turbidity of the supernatant was found to be much lower than the Milli-Q water case. As the salt concentration increased from 0.01 to 1 M, the turbidity of supernatant dropped from 30 to 10 NTU for the NaCl case, while it was always <10 NTU for the CaCl₂ case.

CaCl₂ showed a more significant impact on reducing the turbidity of kaolinite supernatant than that of NaCl.

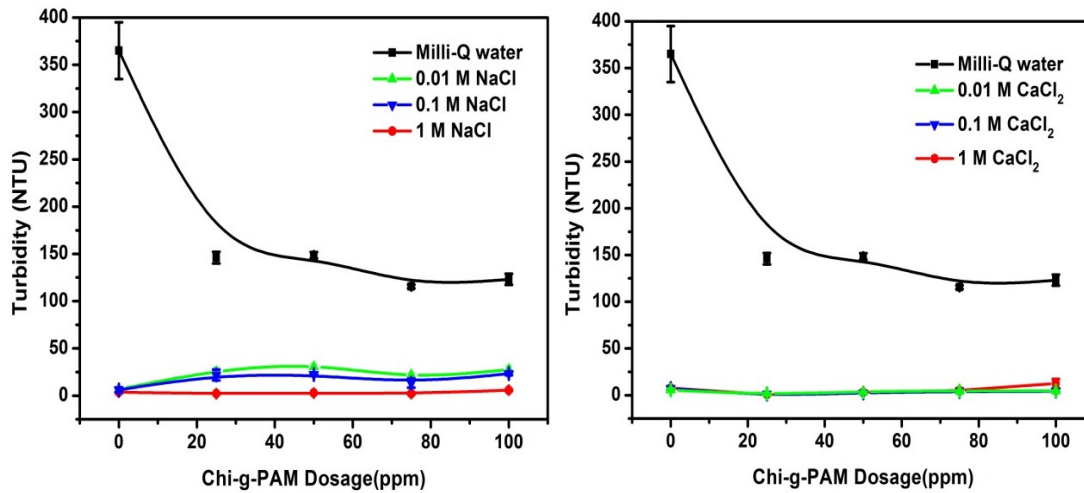


Figure 4.5. Turbidity of kaolinite suspension supernatant after settling 18 hrs at pH ~7.0 in Milli-Q water (■), 0.01 M (▲), 0.1 M (▼) and 1 M (●) NaCl (left) and CaCl₂ (right) solutions.

4.3.3 Zeta potential of kaolinite particles in suspension

The zeta potential of the kaolinite particles left in the supernatant after settling for 18 hours were measured and shown in Figure 4.6. In Milli-Q water, without adding chi-g-PAM, the kaolinite particle was negatively charged with zeta potential around -25 mV. With the addition of chi-g-PAM to Milli-Q water, the zeta potential increased to -3 mV at 75 ppm and to around 0 mV at 100 ppm, suggesting that the positively charged groups on chi-g-PAM backbones could bound to the negatively charged particles. With the addition

of NaCl and CaCl₂, the zeta potential of kaolinite particles became less negative even without the addition of chi-g-PAM, and the influence of CaCl₂ was more pronounced than that of NaCl. It is evident from Figure 4.6 that the addition of a small dosage of chi-g-PAM leads to less negative zeta potential, while further increasing the polymer dosage shows almost negligible impact on the zeta potential which is all close to 0 mV. In 1 M NaCl or CaCl₂ solution, the zeta potential of kaolinite particles even became slightly positive (<5 mV). The above results indicate that the addition of both chi-g-PAM polymer and salts (i.e. NaCl, CaCl₂) can affect the surface charge properties of kaolinite particles.

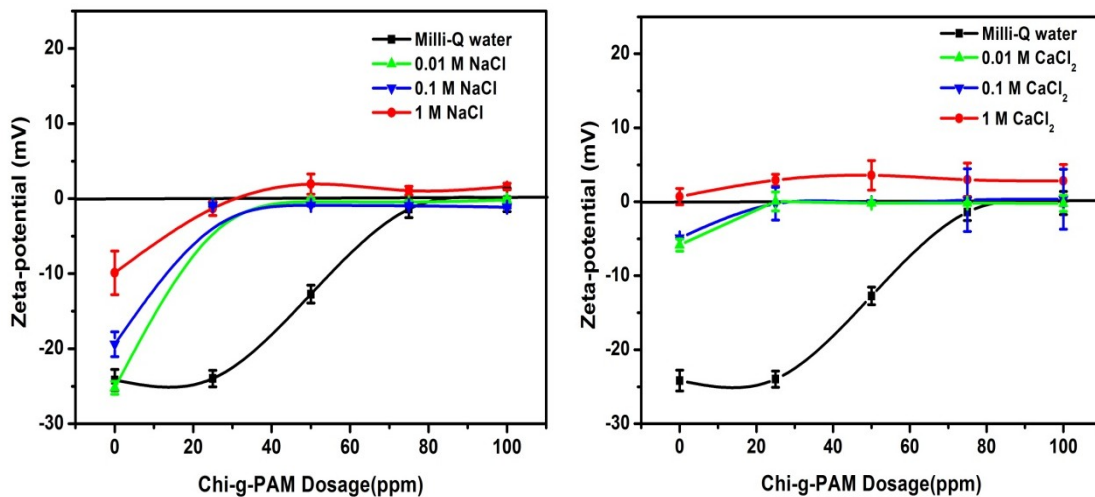


Figure 4.6. Zeta potential of kaolinite particles in the suspension supernatant after settling for 18 hrs at pH ~7.0 in Milli-Q water (■), 0.01 M (▲), 0.1 M (▼) and 1 M (●) NaCl (left) and CaCl₂ (right) solutions.

4.3.4 QCM-D Study on chi-g-PAM adsorption

4.3.4.1 Adsorption of chi-g-PAM on silica sensor surface

The adsorption of chi-g-PAM on silica and alumina surfaces (viz. the two facets of kaolinite) was measured using a QCM-D. The change of frequency and dissipation associated with the adsorption of chi-g-PAM on silica sensor surface in Milli-Q water and saline solutions at pH ~ 7.0 are shown in Figure 4.7 and Figure 4.8. In Milli-Q water (Figure 4.7 a), the change of frequency Δf was -36 Hz indicating that there was strong adsorption of chi-g-PAM on silica sensor surface as compared to the results in 1 M NaCl solutions, which could be mainly due to hydrogen bonding and electrostatic attraction between the cationic amino groups on chi-g-PAM and negatively charged silica surface. Meanwhile, the increment of dissipation in Figure 4.7 a suggests a relatively thick and loose layer of chi-g-PAM adsorbed on the silica sensor surface²⁸. However, when 0.01 M, 0.1 M and 1 M NaCl solutions were introduced into the system, the Δf gradually changed to -30 Hz, -28 Hz and -20 Hz, respectively. For the case of CaCl₂ solutions, Δf changed from -34 Hz in 0.01 M CaCl₂ to -15 Hz in 1 M CaCl₂ as shown in Figure 4.8 a to Figure 4.8 c. The changes of dissipation in Figure 4.7 d and Figure 4.8 c indicate that the adsorbed polymer layer show a more compact conformation under higher salinity

condition. It is evident from the results in Figure 4.7 and Figure 4.8 that the presence of high concentrations of NaCl and CaCl₂ could inhibit the adsorption of chi-g-PAM on silica surfaces as well as influence the conformation of the adsorbed polymers, while the impact of CaCl₂ is more significant than that of NaCl, which could further affect their settling performance of kaolinite particles.

By analyzing the QCM-D data with the Voigt model, the total mass of the polymer film on silica surface is shown in Figure 4.8 d. The mass of adsorbed polymer layer on silica surface decreased from 20.6 ± 2.4 ng/cm² in Milli-Q water to 18.8 ± 2.0 ng/cm² in 0.01 M NaCl solution. Further increasing the NaCl concentration to 1 M, the adsorbed mass decreases to 15.9 ± 1.1 ng/cm². As shown in Figure 4.8 d, the adsorbed polymer mass in CaCl₂ solution is always lower than that in NaCl solution of the same concentration and drops to 10.7 ± 0.2 ng/cm² in 1M CaCl₂. Assuming the density of the adsorbed polymer film to be around 1 g/cm³, the adsorbed polymer layer thickness on silica sensor can be estimated as about 21, 16 and 11 nm in Milli-Q water, 1 M NaCl and 1 M CaCl₂ solutions, respectively.

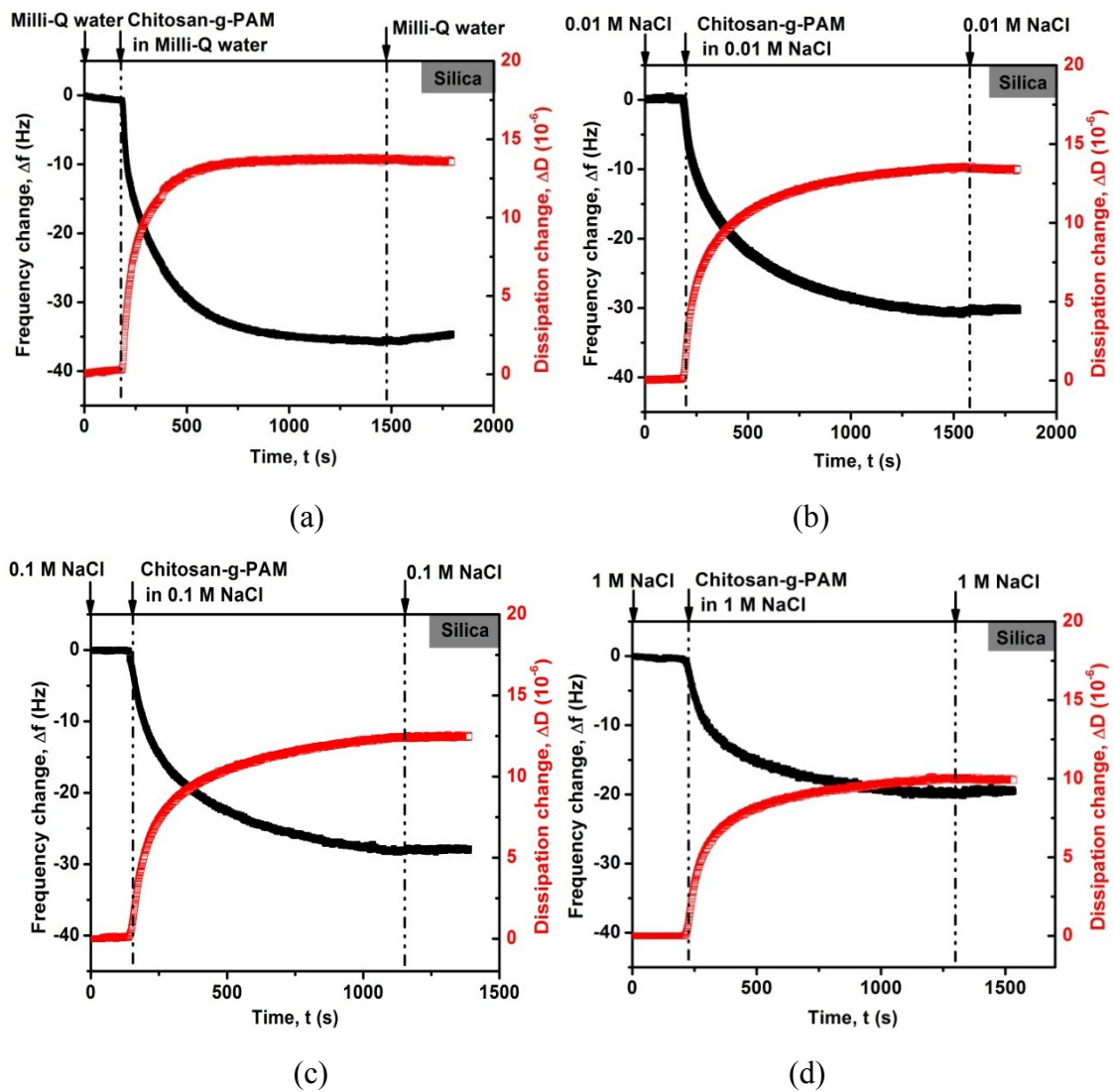


Figure 4.7. Change of frequency Δf and dissipation ΔD associated with the adsorption of chi-g-PAM on QCM-D silica sensors in Milli-Q water and saline solutions at pH ~ 7.0 : (a) Milli-Q water, (b) 0.01 M NaCl, (c) 0.1 M NaCl and (d) 1 M NaCl.

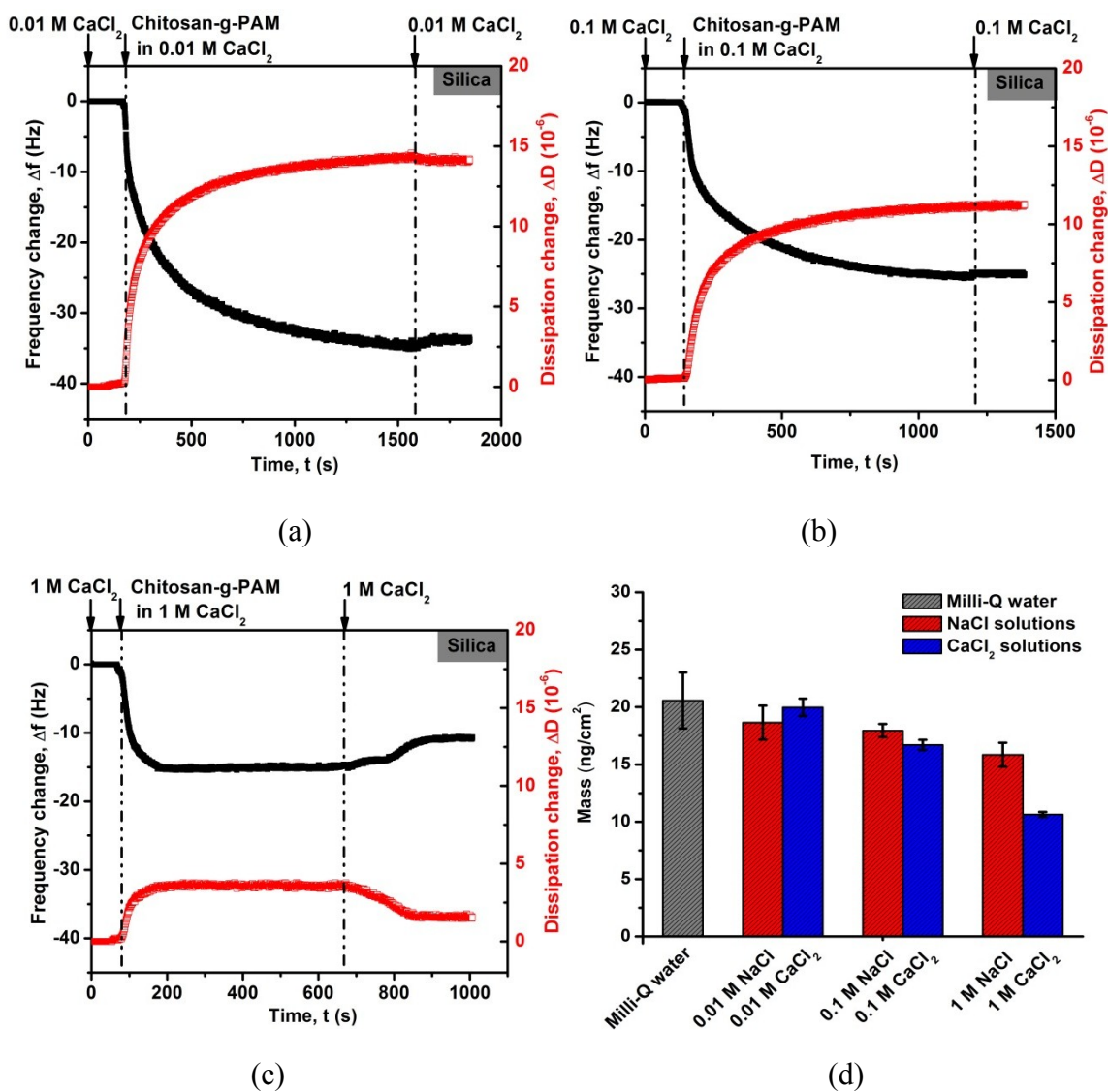


Figure 4.8. Change of frequency Δf and dissipation ΔD associated with the adsorption of chi-g-PAM on QCM-D silica sensors in saline solutions at pH ~ 7.0 : (a) 0.01 M CaCl₂, (b) 0.1 M CaCl₂, (c) 1 M CaCl₂. (d) Mass of polymer layer adsorbed on silica sensors under various solution conditions.

4.3.4.2 Adsorption of chi-g-PAM on alumina sensor surface

The frequency and dissipation change associated with the adsorption of chi-g-PAM adsorption on alumina sensor surfaces in Milli-Q water and saline solutions at pH ~7.0 are shown in Figure 4.9 and Figure 4.10. In Milli-Q water, the frequency drop Δf was -28 Hz on alumina surface (Figure 4.9 a) as compared to the frequency drop of -36 Hz on silica sensor surface (Figure 4.8 a). At pH 7.0, electrostatic repulsion was present between positively charged alumina surface (the pKa of alumina surface is about 8~9)⁸⁷ and cationic groups on chi-g-PAM chains which would weaken the polymer adsorption on alumina surface as compared to the silica surface. Therefore, hydrogen bonding is considered as the main driving force for the chi-g-PAM adsorption on alumina surface²⁸. Similar effects of solution salinity (i.e. NaCl, CaCl₂) on the adsorption of chi-g-PAM on alumina were observed as that on silica, as shown in Figure 4.9 and Figure 4.10. With increasing the salt concentration from 0 to 1 M, Δf changed gradually from -28 Hz to -14 Hz for the NaCl case (Figure 4.9), and from -28 Hz to -7 Hz for the CaCl₂ case (Figure 4.10), respectively. The changes of dissipation in Figure 4.9 and Figure 4.10 suggest that the adsorbed polymer layer have a more compact conformation under higher concentrations of NaCl and CaCl₂. Similar to the silica case, the results in Figure 4.9 and

Figure 4.10 demonstrate that the presence of high concentrations of NaCl and CaCl₂ could inhibit the adsorption of chi-g-PAM on alumina surfaces as well as influence the conformation of the adsorbed polymers, and the impact of CaCl₂ is more significant than that of NaCl.

The mass of the polymer film adsorbed on alumina sensor was calculated using the Voigt model and shown in Figure 4.10 d. It was found that the mass of the adsorbed polymer layer was about 17.4 ± 1.7 ng/cm² on alumina sensor in Milli-Q water. As NaCl concentration increases from 0.01 M to 1 M the mass decreases from 14.4 ± 0.8 ng/cm² to 9.5 ± 0.9 ng/cm². While the adsorbed polymer mass decreases from 6.6 ± 0.5 ng/cm² to 6.2 ± 0.2 ng/cm² as the CaCl₂ concentration increases from 0.01 M to 1 M. The thicknesses of the chi-g-PAM layer on alumina sensors were estimated to be about 17, 10 and 6 nm in Milli-Q water, 1 M NaCl and 1 M CaCl₂, respectively.

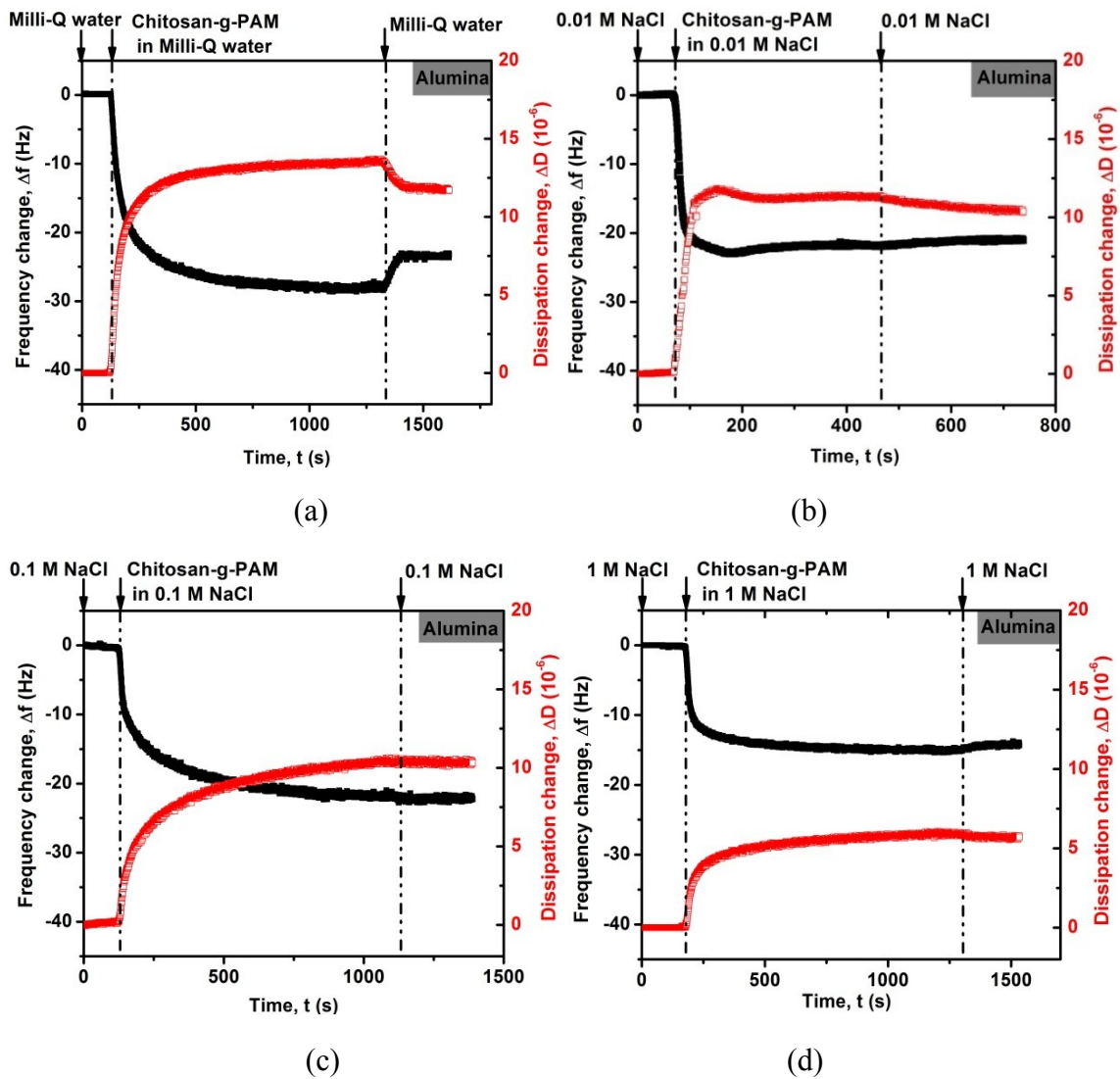


Figure 4.9. Change of frequency Δf and dissipation ΔD associated with the adsorption of chi-g-PAM on QCM-D silica sensors in Milli-Q water and saline solutions at pH ~ 7.0 : (a) Milli-Q water, (b) 0.01 M NaCl, (c) 0.1 M NaCl and (d) 1 M NaCl.

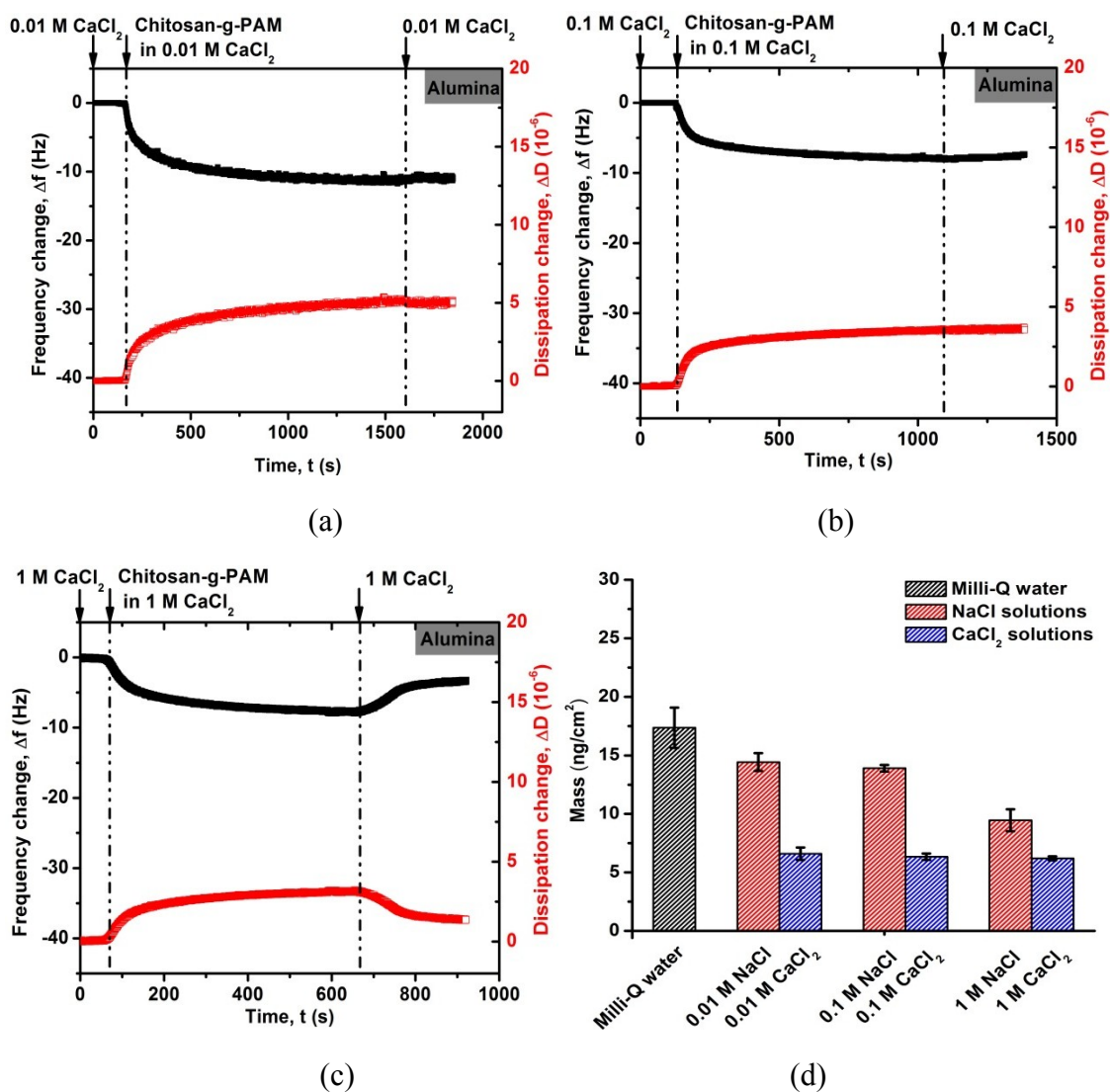


Figure 4.10. Change of frequency Δf and dissipation ΔD associated with the adsorption of chi-g-PAM on QCM-D alumina sensors in saline solutions at pH ~ 7.0 : (a) 0.01 M CaCl_2 , (b) 0.1 M CaCl_2 , (c) 1 M CaCl_2 . (d) Mass of polymer layer adsorbed on alumina sensors under various solution conditions.

4.3.5 Surface force measurements

To probe the interaction forces of chi-g-PAM and kaolinite particles, surface force measurements were carried out between model clay surfaces (i.e. mica, which has similar

surface composition as kaolinite) in chi-g-PAM solutions using an SFA. The typical force-distance profiles between two mica surfaces in 5 ppm chi-g-PAM solutions with different salt concentrations are shown in Figure 4.11. Repulsion was detected during the approach of two mica surfaces for all the three cases, as shown in Figure 4.11 a, b and c for Milli-Q water, 1 M NaCl and 1 M CaCl₂, respectively. The range of the repulsion was decreased from ~39 nm in Milli-Q water, to ~32 nm in 1 M NaCl and further to ~21 nm in 1 M CaCl₂. The repulsion force range in SFA measurements was found to be correlated very well with the polymer thickness adsorbed on silica sensors estimated from QCM-D measurements, viz. the repulsion starts at a separation distance that roughly doubled the polymer thickness (which is about 21, 16 and 11 for one polymer layer on silica sensor in Milli-Q water, 1M NaCl and 1 M CaCl₂ solutions, respectively, as determined from the QCM-D measurements in Figure 4.7 and Figure 4.8). The repulsion was mainly due to the steric interaction of the adsorbed polymer layers on the opposing mica substrates; while the shortened range of repulsion was consistent with the more compact conformation based on the dissipation change from the QCM-D measurements. Adhesion was measured during separation for all the three cases, the adhesion results were summarized in Figure 4.11 d. Strong adhesion $F_{ad}/R \sim -38$ mN/m

was measured in Milli-Q water, which was mainly due to the bridging attraction of adsorbed chi-g-PAM on the two mica surfaces. While the adhesion drastically dropped to $F_{ad}/R \sim -2$ mN/m in 1 M NaCl and CaCl₂, which indicates a significantly weakened bridging interaction and is consistent with the poor flocculation behavior of chi-g-PAM polymer on kaolinite suspension under high salinity conditions.

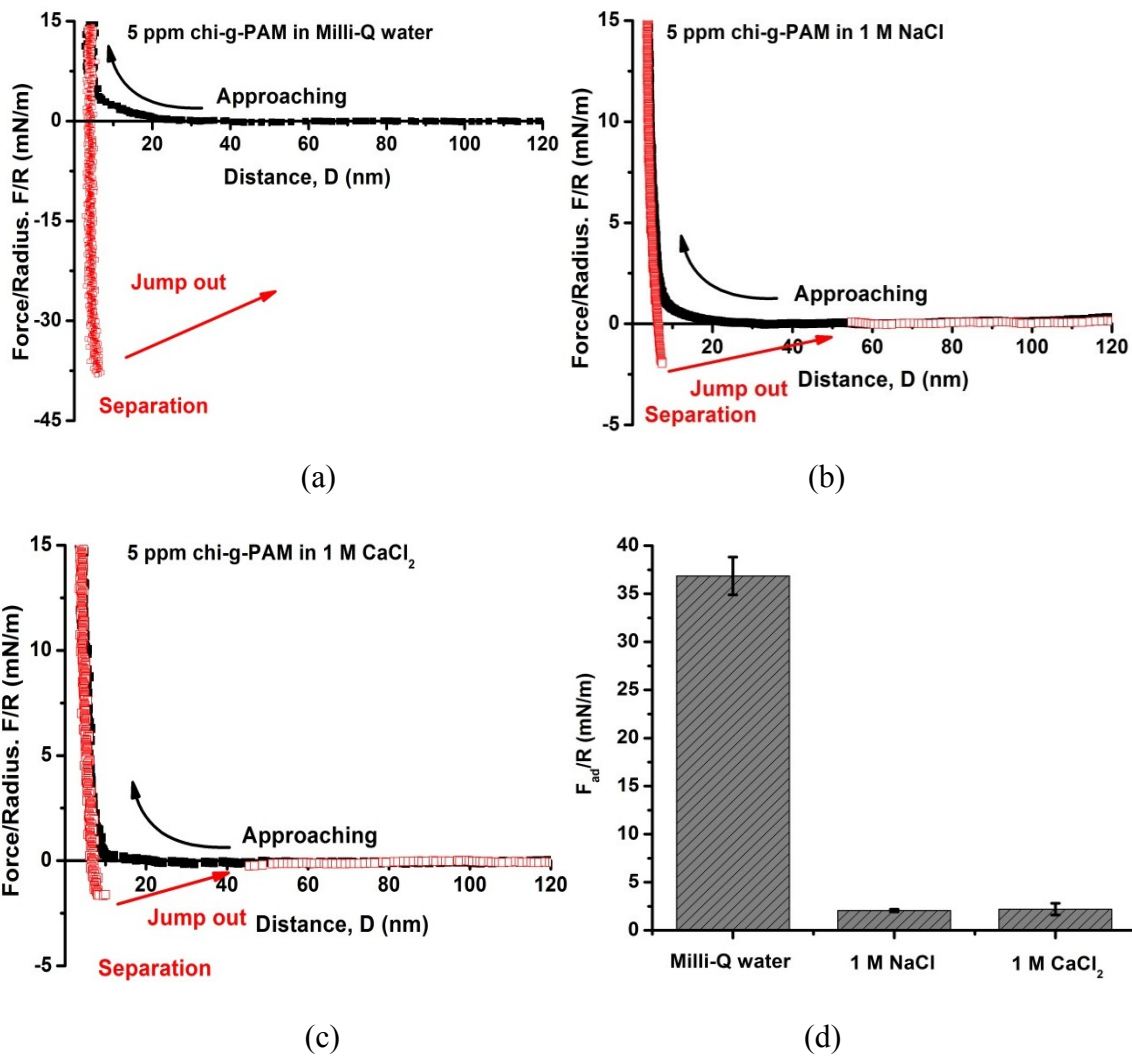
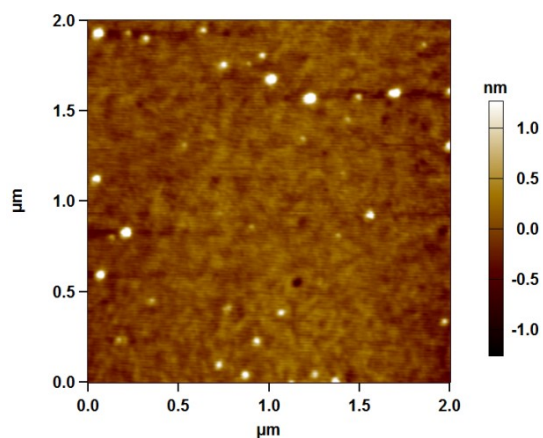


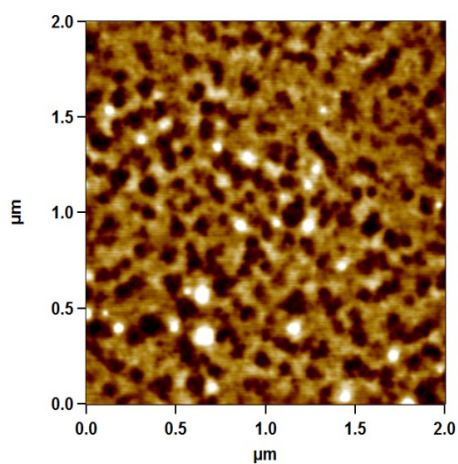
Figure 4.11. Typical force-distance profiles between mica surfaces in 5 ppm chi-g-PAM solutions at pH \sim 7.0 in: (a) Milli-Q water, (b) 1 M NaCl, (c) 1 M CaCl₂ and (d) adhesion force result.

4.3.6 The morphology of chi-g-PAM adsorption on mica

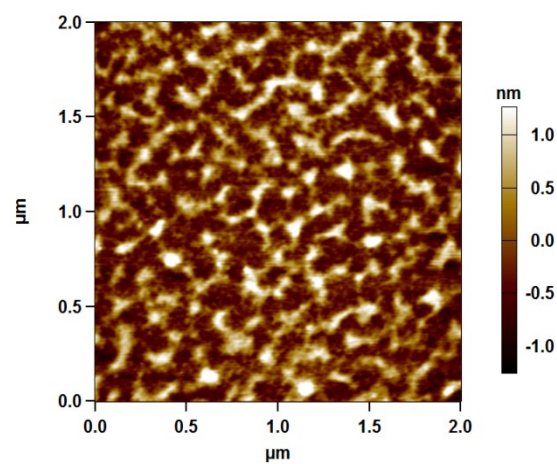
The morphology of chi-g-PAM adsorbed on mica in Milli-Q water, 1 M NaCl and 1 M CaCl₂ was imaged using an AFM and shown in Figure 4.12 a, b and c, respectively. Figure 4.12 a shows that mica surface was uniformly covered by the chi-g-PAM molecules with RMS roughness around 0.2 nm. However, the polymer aggregates became visible on mica in 1 M NaCl (Figure 4.12 b) case, and the aggregates were more significant in 1 M CaCl₂ solution (Figure 4.12 c). The AFM images in Figure 4.12 b and c are consistent with results from the adsorption tests by QCM-D and surface force measurements by SFA, that chi-g-PAM chains show the aggregation of polymer under high salinity conditions which leads to weakened bridging attraction and poor flocculation performance.



(a)



(b)



(c)

Figure 4.12. Topographic AFM images of 50 ppm chi-g-PAM adsorbed on mica substrates in (a) Milli-Q water, (b) 1 M NaCl and (c) 1 M CaCl₂. The images were taken on dried samples in air.

4.3.7 Interaction model between chi-g-PAM and kaolinite particles

In the settling tests, kaolinite suspension treated by chi-g-PAM showed highest ISR in Milli-Q water, whereas high concentrations of NaCl or CaCl₂ decreased the ISR. QCM-D measurements demonstrate that chi-g-PAM shows better adsorption capability

on both silica and alumina sensors in Milli-Q water than that in NaCl and CaCl₂ solutions. The dissipation change in QCM-D measurements indicates the addition of NaCl and CaCl₂ leads to a more compact conformation of the adsorbed polymer chains. Based on the complimentary results from settling tests, measurements by zeta potential analyzer, QCM-D, SFA and AFM, the interaction model between the chi-g-PAM polymer chains and kaolinite particles is proposed as follows.

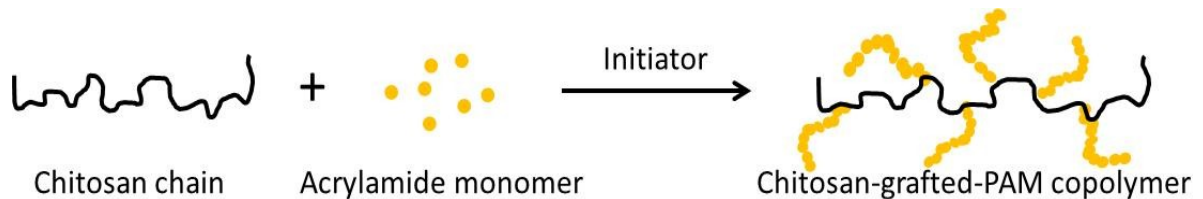


Figure 4.13. Schematic of chi-g-PAM structure after grafting polymerization.

During synthesis, acrylamide monomers polymerized along chitosan backbone chain and formed branched PAM side chains as illustrated in Figure 4.13. Some of the original positively charged sites on the backbone chains could be shielded by the PAM side chains so chi-g-PAM was only weakly positively charged at pH ~7.0. The extended PAM chains facilitated the formation of the hydrogen bonding of the amide groups and surfaces of kaolinite particles, and the (weakly) positively charged ammonium sites on

chitosan backbones could further enhance polymer adsorption onto kaolinite surfaces via electrostatic attraction with the negatively charged silica face.

In Milli-Q water, due to the intra-molecular electrostatic repulsions and steric repulsion between the hydrated PAM side chains, chi-g-PAM chains exhibit a relatively extended conformation, which could enhance the interactions between polymer chains and kaolinite particles and thus help their adsorption (Figure 4.14 a). After introducing NaCl or CaCl₂, especially with a high concentration, the adsorbed polymer chains switch to a more condensed conformation, which would diminish the occurrence of effective bounding sites between polymer chains and kaolinite particles ^{119,120}. Meanwhile, the electrostatic interactions between the kaolinite particles and between kaolinite surfaces and polymer chains are significantly suppressed under high salinity conditions (Figure 4.14 b). Therefore, a weakened polymer adsorption on kaolinite particles was observed, which in turn plays a detrimental role in the weakened bridging interactions between polymer chain and kaolinite particles and hence results in poor flocculant performance of chi-g-PAM under high salinity conditions.

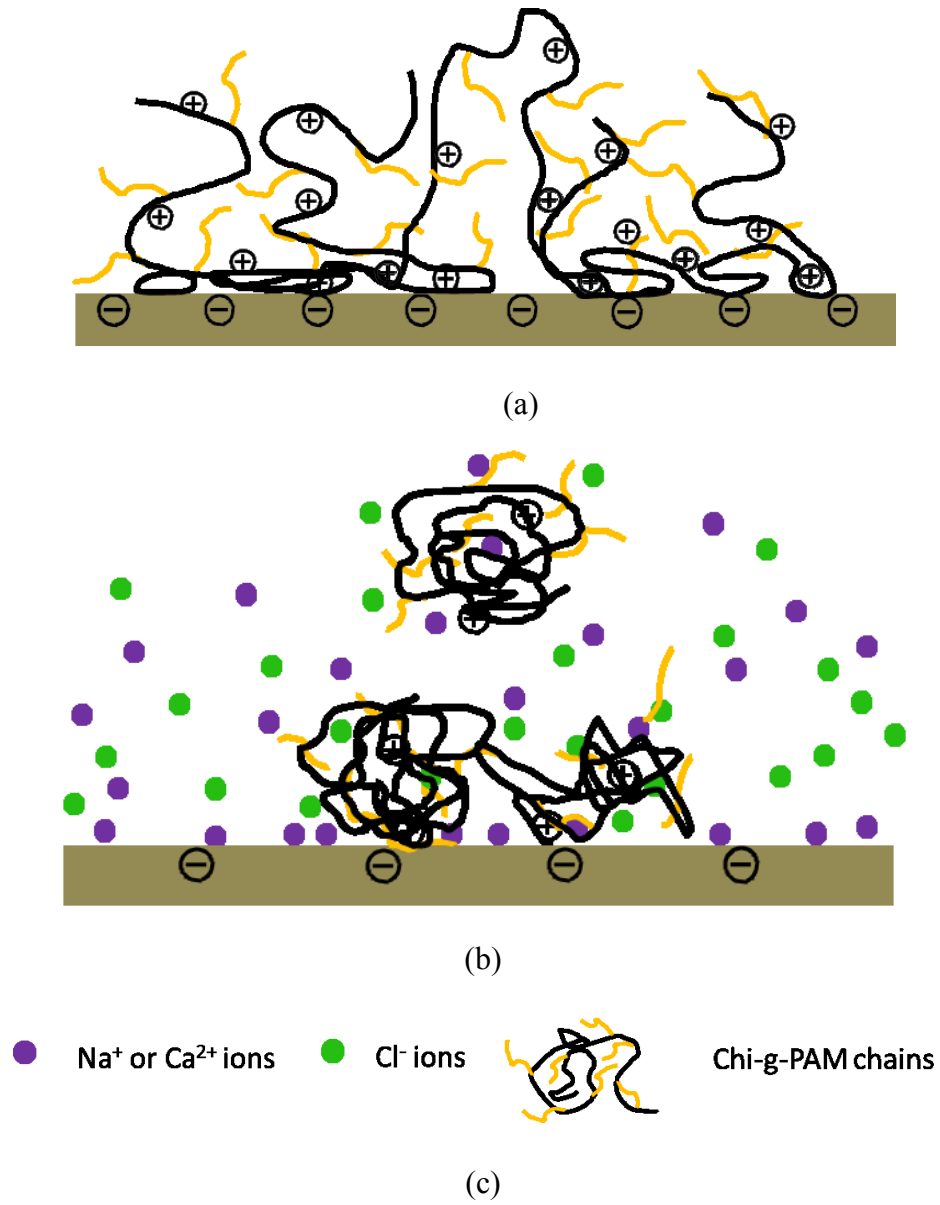


Figure 4.14. Proposed interaction model of chi-g-PAM and negatively charged kaolinite particle surfaces in: (a) Milli-Q water, and (b) salt solutions. (c) Illustration of symbols.

4.4 Conclusions

In this work, chi-g-PAM was synthesized and characterized. The flocculation behaviors of chi-g-PAM on kaolinite suspensions and the impact of solution salinity (viz.

addition of NaCl and CaCl₂) were systematically investigated via several complementary techniques. The ISR was found to be lower in high concentration of NaCl and CaCl₂ solutions than that in Milli-Q water; while the supernatant turbidity was significantly decreased with increasing the solution salinity. QCM-D measurements show that the high concentration of NaCl and CaCl₂ could inhibit the adsorption of chi-g-PAM chains on both the silica and alumina facets of kaolinite. SFA force measurements show that the addition of high concentration of NaCl and CaCl₂ could drastically weaken the bridging interaction of chi-g-PAM. It is evident from the settling tests, zeta potential measurements, adsorption tests using QCM-D, surface force measurements by SFA and AFM imaging that the addition of high concentrations of NaCl and CaCl₂ can significantly impact chi-g-PAM polymer conformation and surface charge properties of kaolinite surfaces, which influence the interactions between the polymer chains and kaolinite particle surfaces, thus resulting in poor flocculation performance under high salinity solution conditions.

Chapter 5 Summary and Future work

5.1 Summary

In this project, the flocculation behaviors of two polymer flocculants, a commercial anionic flocculant Magnafloc 1011 and a lab-synthesized cationic polymer chi-g-PAM, in saline solutions were systematically investigated by various complementary techniques. The major finds and conclusions of this thesis work are summarized as follows:

- a) Introducing MgCl_2 can increase the initial settling rate of MF on kaolinite flocculation. As salt concentration increased from 0.01 M to 1 M, the maximum ISR increased accordingly and the high ISR located in 1 M MgCl_2 at MF dosage 75 ppm.
- b) In MgCl_2 solution, the electrostatic-double layers of charged particles have been heavily compressed and the structure of electrolytes was also affected, facilitating the formation of acrylate-Mg-acrylate complex and hydrogen bonding, which enhanced the kaolinite suspension settling.

- c) Alumina surfaces were the first time to be prepared by coating alumina films over mica surfaces in SFA measurements. However, when $MgCl_2$ concentration increased from 0.01 to 1 M, the adhesive forces changing tendency between mica surfaces were opposite to that between alumina surfaces, which were may due to the different surface charge properties.
- d) By investigating the adsorption behavior of MF on silica and alumina surfaces, the differences on the adsorption and adhesions were mainly due to $MgCl_2$ concentration, polymer structure and the surface charge properties.
- e) The chi-g-PAM was synthesized and its molecular weight was determined by SLS at 1,840,000 g/mol and chi-g-PAM presented better pH stability from acidic to alkaline conditions compared to chitosan.
- f) The ISR in kaolinite flocculation increased as the chi-g-PAM dosages increased. High concentration of NaCl and $CaCl_2$ show negative influence on the flocculation behavior of chi-g-PAM settling on kaolinite suspension, while the impact of $CaCl_2$ is more significant than that of NaCl.
- g) High concentration salt generated clear supernatant which was may due to high concentration electrolytes solutions compressed EDL of the kaolinite particles.

- h) In Milli-Q water, chi-g-PAM molecules extended on the surfaces and coupled lots of water molecules in between, while under the influence of high concentration NaCl or CaCl₂ solutions, polymers preferred to “coil-like” structure or forming aggregations on the surfaces.
- i) By studying chi-g-PAM adsorption and interaction properties on particle surfaces, it was found that high concentration of NaCl and CaCl₂ inhibited the adsorption of chi-g-PAM chains on both the silica and alumina facets of kaolinite and weakened the bridging interaction of chi-g-PAM, thus resulting in poor flocculation performance under high salinity solution conditions.

5.2 Future work

5.2.1 MF 1011 flocculation future study

Although the surface interaction model of MF 1011 in saline solutions can explain the settling mechanism, some problems remain to be answered in the future.

- a) For the QCM-D experiment, it was hard to explain the long equilibrium time for the MF molecules adsorption in Mg²⁺ solutions on silica sensor. The slow adsorption seems not quite agree with the rapid ISR.

- b) MF shows excellent settling performance in model clay suspension (kaolinite suspension). For real saline tailings, its flocculation ability may be further improved by adjusting the settling conditions, e.g., salt concentration, dosage, agitation rate, etc.

5.2.2 Chi-g-PAM flocculation future study

It is the first time that the salinity's influence on chi-g-PAM's flocculation performance was carried out in this study. Based on the previous research, this work provides some surface force study on chi-g-PAM interaction with particles and some details need to be covered in the future.

- a) The chi-g-PAM grafting ratio has not been determined yet. ^1H MR could be one of the powerful techniques to determine this parameter.
- b) Although it showed high settling rate in kaolinite/Milli-Q water suspension, while high salinity (addition of Na^+ and Ca^{2+}) generated clear supernatant but reduced the settling rate. The proper salt concentration which can get both high ISR and low turbidity should be explored.

- c) In the surface force measurement, tests were only done between mica-mica surfaces. The alumina surface coating techniques can also be applied in this project to further understand chi-g-PAM surface force between clay surfaces.

References

- [1] Gleick, P. H., *Water Resources. In Encyclopaedia of Climate and Weather*. Oxford University Press: New York, **1996**; Vol. 2.
- [2] Greenlee, L. F.; Lawler, D. F.; Freeman, B. D.; Marrot, B.; Moulin, P., Reverse osmosis desalination: Water sources, technology, and today's challenges. *Water research* **2009**, 43, (9), 2317-2348.
- [3] Randall, D. G.; Nathoo, J.; Lewis, A. E., A case study for treating a reverse osmosis brine using Eutectic Freeze Crystallization—Approaching a zero waste process. *Desalination* **2011**, 266, (1–3), 256-262.
- [4] Lee, K. P.; Arnot, T. C.; Mattia, D., A review of reverse osmosis membrane materials for desalination—Development to date and future potential. *Journal of Membrane Science* **2011**, 370, (1–2), 1-22.
- [5] Castro, S.; Venegas, I.; Landero, A.; Laskowski, J. In *Frothing in seawater flotation systems*, XXV International Mineral Processing Congress 2010, IMPC 2010, 2010; 2010; pp 4039-4047.
- [6] Klassen, V. I. M. V. A., *An introduction to the theory of flotation*. Butterworths: London, **1963**.
- [7] *Design and Evaluation of Tailings Dams: Technical Report*. U.S. Environmental Protection Agency, Office of Solid Waste: **1994**.
- [8] Sabah, E.; Cengiz, I., An evaluation procedure for flocculation of coal preparation plant tailings. *Water research* **2004**, 38, (6), 1542-1549.

- [9] Kaminsky, H.; Etsell, T. O. M.; Ivey, D. G.; Omotoso, O., Fundamental Particle Size of Clay Minerals in Athabasca Oil Sands Tailings(Clays and Environment,Proceedings of the 13th International Clay Conference). *Clay science* **2006**, 12, (2), 217-222.
- [10] Sivamohan, R., The problem of recovering very fine particles in mineral processing — A review. *International journal of mineral processing* **1990**, 28, (3–4), 247-288.
- [11] Tripathy, T.; De, B. R., Flocculation: a new way to treat the waste water. *Journal of Physical Sciences* **2006**, 10, 93-127.
- [12] Sharma, B. R.; Dhuldhoya, N. C.; Merchant, U. C., Flocculants—an Ecofriendly Approach. *Journal of Polymers and the Environment* **2006**, 14, (2), 195-202.
- [13] Bratby, J., *Coagulation and Flocculation in Water and Wastewater Treatment*. IWA Publishing: **2006**.
- [14] Ji, Y.; Lu, Q.; Liu, Q.; Zeng, H., Effect of solution salinity on settling of mineral tailings by polymer flocculants. *Colloids and Surfaces A: Physicochemical and Engineering Aspects* **2013**, 430, (0), 29-38.
- [15] Wong, S. S.; Teng, T. T.; Ahmad, A. L.; Zuhairi, A.; Najafpour, G., Treatment of pulp and paper mill wastewater by polyacrylamide (PAM) in polymer induced flocculation. *Journal of Hazardous Materials* **2006**, 135, (1–3), 378-388.
- [16] Gregory, J.; Barany, S., Adsorption and flocculation by polymers and polymer mixtures. *Advances in Colloid and Interface Science* **2011**, 169, (1), 1-12.
- [17] Finch, C. A., *Industrial water soluble polymers*. Royal Society of Chemistry,: **1996**; p 62.

- [18] Vincent, B., The effect of adsorbed polymers on dispersion stability. *Advances in Colloid and Interface Science* **1974**, 4, (2–3), 193-277.
- [19] Jeffrey, G. A., *An Introduction to Hydrogen Bonding*. Oxford University Press: **1997**.
- [20] Haschke, H.; Miles, M. J.; Sheppard, S., Adsorption of Individual Polyacrylamide Molecules Studied by Atomic Force Microscopy. *Single Molecules* **2002**, 3, (2-3), 171-172.
- [21] Allan McNaught, A. W., *The Compendium of Chemical Terminology*. 2nd ed.; IUPAC: **1997**.
- [22] Winterton, R. H. S., Van der Waals forces. *Contemporary Physics* **1970**, 11, (6), 559-574.
- [23] Zhou, Y.; Gan, Y.; Wanless, E. J.; Jameson, G. J.; Franks, G. V., Interaction Forces between Silica Surfaces in Aqueous Solutions of Cationic Polymeric Flocculants: Effect of Polymer Charge. *Langmuir* **2008**, 24, (19), 10920-10928.
- [24] Dahlgren, M. A. G., Effect of Counterion Valency and Ionic Strength on Polyelectrolyte Adsorption. *Langmuir* **1994**, 10, (5), 1580-1583.
- [25] Masliyah, J. H.; Xu, Z.; Czarnecki, J. A., *Handbook on Theory and Practice of Bitumen Recovery from Athabasca Oil Sands*. Kingsley Publishing Services: **2011**.
- [26] Coleman, M. M., *Fundamentals of Polymer Science: An Introductory Text*. Second Edition ed.; CRC Press: **1998**.
- [27] Patel, S. S.; Tirrell, M., Measurement of forces between surfaces in polymer fluids. *Annual Review of Physical Chemistry* **1989**, 40, (1), 597-635.

- [28] Alagha, L.; Wang, S.; Xu, Z.; Masliyah, J., Adsorption Kinetics of a Novel Organic–Inorganic Hybrid Polymer on Silica and Alumina Studied by Quartz Crystal Microbalance. *The Journal of Physical Chemistry C* **2011**, 115, (31), 15390-15402.
- [29] Sauerbrey, G., Verwendung von Schwingquarzen zur Wägung dünner Schichten und zur Mikrowägung. *Zeitschrift für Physik* **1959**, 155, (2), 206-222.
- [30] Voinova, M. V.; Rodahl, M.; Jonson, M.; Kasemo, B., Viscoelastic Acoustic Response of Layered Polymer Films at Fluid-Solid Interfaces: Continuum Mechanics Approach. *Physica Scripta* **1999**, 59, (5), 391.
- [31] Parsegian, V. A., Reconciliation of van der Waals force measurements between phosphatidylcholine bilayers in water and between bilayer-coated mica surfaces. *Langmuir* **1993**, 9, (12), 3625-3628.
- [32] Parsegian, V. A.; Rand, R. P.; Fuller, N. L., Direct osmotic stress measurements of hydration and electrostatic double-layer forces between bilayers of double-chained ammonium acetate surfactants. *The Journal of Physical Chemistry* **1991**, 95, (12), 4777-4782.
- [33] Meyer, E. E.; Rosenberg, K. J.; Israelachvili, J., Recent progress in understanding hydrophobic interactions. *Proceedings of the National Academy of Sciences* **2006**, 103, (43), 15739-15746.
- [34] Tsao, Y. H.; Yang, S. X.; Evans, D. F.; Wennerstroem, H., Interactions between hydrophobic surfaces. Dependence on temperature and alkyl chain length. *Langmuir* **1991**, 7, (12), 3154-3159.

- [35] Crassous, J.; Charlaix, E.; Gayvallet, H.; Loubet, J. L., Experimental study of a nanometric liquid bridge with a surface force apparatus. *Langmuir* **1993**, 9, (8), 1995-1998.
- [36] Chapel, J. P., Electrolyte Species Dependent Hydration Forces between Silica Surfaces. *Langmuir* **1994**, 10, (11), 4237-4243.
- [37] Wong, J.; Chilkoti, A.; Moy, V. T., Direct force measurements of the streptavidin–biotin interaction. *Biomolecular Engineering* **1999**, 16, (1–4), 45-55.
- [38] Tabor, D.; Winterton, R. H. S., The Direct Measurement of Normal and Retarded van der Waals Forces. *Proceedings of the Royal Society of London. A. Mathematical and Physical Sciences* **1969**, 312, (1511), 435-450.
- [39] Israelachvili, J. N.; Adams, G. E., Measurement of forces between two mica surfaces in aqueous electrolyte solutions in the range 0–100 nm. *Journal of the Chemical Society, Faraday Transactions 1: Physical Chemistry in Condensed Phases* **1978**, 74, 975-1001.
- [40] Israelachvili, J. N., Techniques for direct measurements of forces between surfaces in liquids at the atomic scale. *Chemtracts Anal. Phys. Chem* **1989**, 1, (1).
- [41] Israelachvili, J. N.; McGuiggan, P. M., Adhesion and short-range forces between surfaces. Part I: New apparatus for surface force measurements. *Journal of Materials Research* **1990**, 5, (10), 2223-2231.
- [42] Israelachvili, J. N., *Intermolecular and Surface Forces: Revised Third Edition*. Elsevier Science: **2011**.

- [43] Lin, Q.; Gourdon, D.; Sun, C.; Holten-Andersen, N.; Anderson, T. H.; Waite, J. H.; Israelachvili, J. N., Adhesion mechanisms of the mussel foot proteins mfp-1 and mfp-3. *Proceedings of the National Academy of Sciences* **2007**, 104, (10), 3782-3786.
- [44] Israelachvili, J. N., Thin film studies using multiple-beam interferometry. *Journal of Colloid and Interface Science* **1973**, 44, (2), 259-272.
- [45] Tolansky, S., *Multiple-beam interferometry of surfaces and films*. Clarendon Press: **1948**.
- [46] Horn, R. G.; Smith, D. T., Analytic solution for the three-layer multiple beam interferometer. *Applied Optics* **1991**, 30, (1), 59-65.
- [47] Israelachvili, J. N., *Intermolecular and surface forces / Jacob N. Israelachvili*. Academic Press: London ; San Diego, **1991**.
- [48] Butt, H.-J.; Cappella, B.; Kappl, M., Force measurements with the atomic force microscope: Technique, interpretation and applications. *Surface Science Reports* **2005**, 59, (1-6), 1-152.
- [49] Rubio, J.; Carissimi, E.; Rosa, J. J., Flotation in water and wastewater treatment and reuse: recent trends in Brazil. *International Journal of Environment and Pollution* **2007**, 30, (2), 197-212.
- [50] Fuerstenau, M. C.; Miller, J. D.; Kuhn, M. C., *Chemistry of flotation*. Society of Mining Engineers of the America Institute of Mining, Metallurgical and Petroleum Engineers, Inc.: New York, **1985**; p v, 177 p.
- [51] Rao, S. R.; Finch, J. A., A review of water re-use in flotation. *Minerals Engineering* **1989**, 2, (1), 65-85.

- [52] Van Olphen, H., *An introduction to clay colloid chemistry: for clay technologists, geologists, and soil scientists*. Interscience Publishers: **1963**.
- [53] O'Shea, J.-P.; Tallón, C., The effect of salt concentration and pH on the solid–liquid separation of silica suspensions with a temperature-responsive flocculant. *Separation and Purification Technology* **2011**, 82, (0), 167-176.
- [54] Lee, B. J.; Schlautman, M. A.; Toorman, E.; Fettweis, M., Competition between kaolinite flocculation and stabilization in divalent cation solutions dosed with anionic polyacrylamides. *Water research* **2012**, 46, (17), 5696-5706.
- [55] Pearse, M. J., An overview of the use of chemical reagents in mineral processing. *Minerals Engineering* **2005**, 18, (2), 139-149.
- [56] Landman, K. A.; White, L. R., Solid/liquid separation of flocculated suspensions. *Advances in Colloid and Interface Science* **1994**, 51, (0), 175-246.
- [57] Tanaka, H.; Ödberg, L.; Wågberg, L.; Lindström, T., Adsorption of cationic polyacrylamides onto monodisperse polystyrene latices and cellulose fiber: Effect of molecular weight and charge density of cationic polyacrylamides. *Journal of Colloid and Interface Science* **1990**, 134, (1), 219-228.
- [58] Bolto, B.; Gregory, J., Organic polyelectrolytes in water treatment. *Water research* **2007**, 41, (11), 2301-2324.
- [59] Subject Index. In *Particle Deposition & Aggregation*, Elimelech, M., et al., Eds. Butterworth-Heinemann: Woburn, **1995**; pp 433-441.

- [60] Mpofu, P.; Addai-Mensah, J.; Ralston, J., Influence of hydrolyzable metal ions on the interfacial chemistry, particle interactions, and dewatering behavior of kaolinite dispersions. *Journal of Colloid and Interface Science* **2003**, 261, (2), 349-359.
- [61] Nasser, M. S.; James, A. E., The effect of polyacrylamide charge density and molecular weight on the flocculation and sedimentation behaviour of kaolinite suspensions. *Separation and purification technology* **2006**, 52, (2), 241-252.
- [62] Taylor, M. L.; Morris, G. E.; Self, P. G.; Smart, R. S., Kinetics of adsorption of high molecular weight anionic polyacrylamide onto kaolinite: The flocculation process. *Journal of Colloid and Interface Science* **2002**, 250, (1), 28-36.
- [63] Nasser, M. S.; James, A. E., Degree of flocculation and viscoelastic behaviour of kaolinite-sodium chloride dispersions. *Colloids and Surfaces a-Physicochemical and Engineering Aspects* **2008**, 315, (1-3), 165-175.
- [64] Zbik, M. S.; Smart, R. S. C.; Morris, G. E., Kaolinite flocculation structure. *Journal of Colloid and Interface Science* **2008**, 328, (1), 73-80.
- [65] Sworska, A.; Laskowski, J.; Cymerman, G., Flocculation of the Syncrude fine tailings: Part I. Effect of pH, polymer dosage and Mg²⁺ and Ca²⁺ cations. *International journal of mineral processing* **2000**, 60, (2), 143-152.
- [66] Stumm, W.; Morgan, J. J., *Aquatic chemistry: chemical equilibria and rates in natural waters*. John Wiley & Sons: **2012**; Vol. 126.
- [67] Ji, Y. Fundamental Understanding of the Flocculation of Mineral Tailings in High Salinity Water. Thesis, University of Alberta, **2013**.

- [68] Haschke, H.; Miles, M. J.; Koutsos, V., Conformation of a Single Polyacrylamide Molecule Adsorbed onto a Mica Surface Studied with Atomic Force Microscopy. *Macromolecules* **2004**, *37*, (10), 3799-3803.
- [69] Long, J.; Xu, Z.; Masliyah, J. H., Adhesion of single polyelectrolyte molecules on silica, mica, and bitumen surfaces. *Langmuir* **2006**, *22*, (4), 1652-1659.
- [70] Alagha, L.; Wang, S.; Yan, L.; Xu, Z.; Masliyah, J., Probing Adsorption of Polyacrylamide-Based Polymers on Anisotropic Basal Planes of Kaolinite Using Quartz Crystal Microbalance. *Langmuir* **2013**, *29*, (12), 3989-3998.
- [71] Das, R.; Ghorai, S.; Pal, S., Flocculation characteristics of polyacrylamide grafted hydroxypropyl methyl cellulose: An efficient biodegradable flocculant. *Chemical Engineering Journal* **2013**, *229*, (0), 144-152.
- [72] Balastre, M.; Li, F.; Schorr, P.; Yang, J.; Mays, J. W.; Tirrell, M. V., A study of polyelectrolyte brushes formed from adsorption of amphiphilic diblock copolymers using the surface forces apparatus. *Macromolecules* **2002**, *35*, (25), 9480-9486.
- [73] Raviv, U.; Giasson, S.; Kampf, N.; Gohy, J.-F.; Jérôme, R.; Klein, J., Normal and frictional forces between surfaces bearing polyelectrolyte brushes. *Langmuir* **2008**, *24*, (16), 8678-8687.
- [74] Theng, B. K. G., *Formation and properties of clay-polymer complexes*. Access Online via Elsevier: **2012**; Vol. 4.
- [75] Wang, X.; Feng, X.; Xu, Z.; Masliyah, J. H., Polymer aids for settling and filtration of oil sands tailings. *The Canadian Journal of Chemical Engineering* **2010**, *88*, (3), 403-410.

- [76] Yazdandoost, F.; Attari, J., *Hydraulics of Dams and River Structures: Proceedings of the International Conference, Tehran, Iran, 26-28 April 2004*. Taylor & Francis: **2004**.
- [77] Israelachvili, J. N., *Intermolecular and surface forces*. Academic Press London: **1991**.
- [78] Israelachvili, J.; Min, Y.; Akbulut, M.; Alig, A.; Carver, G.; Greene, W.; Kristiansen, K.; Meyer, E.; Pesika, N.; Rosenberg, K.; Zeng, H., Recent advances in the surface forces apparatus (SFA) technique. In *Reports on Progress in Physics*, 2010; Vol. 73.
- [79] Wang, J.; van der Tuuk Opedal, N.; Lu, Q.; Xu, Z.; Zeng, H.; Sjöblom, J., Probing Molecular Interactions of an Asphaltene Model Compound in Organic Solvents Using a Surface Forces Apparatus (SFA). *Energy & Fuels* **2011**, 26, (5), 2591-2599.
- [80] Natarajan, A.; Xie, J.; Wang, S.; Liu, Q.; Masliyah, J.; Zeng, H.; Xu, Z., Understanding Molecular Interactions of Asphaltenes in Organic Solvents Using a Surface Force Apparatus. *The Journal of Physical Chemistry C* **2011**, 115, (32), 16043-16051.
- [81] Ducker, W. A.; Xu, Z.; Clarke, D. R.; Israelachvili, J. N., Forces between Alumina Surfaces in Salt Solutions: Non - DLVO Forces and the Implications for Colloidal Processing. *Journal of the American Ceramic Society* **1994**, 77, (2), 437-443.
- [82] Rodahl, M.; Hook, F.; Krozer, A.; Brzezinski, P.; Kasemo, B., Quartz crystal microbalance setup for frequency and Q - factor measurements in gaseous and liquid environments. *Review of Scientific Instruments* **1995**, 66, (7), 3924-3930.
- [83] Höök, F.; Kasemo, B.; Nylander, T.; Fant, C.; Sott, K.; Elwing, H., Variations in coupled water, viscoelastic properties, and film thickness of a Mefp-1 protein film during

adsorption and cross-linking: a quartz crystal microbalance with dissipation monitoring, ellipsometry, and surface plasmon resonance study. *Analytical chemistry* **2001**, 73, (24), 5796-5804.

[84] Peng, F. F.; Di, P., Effect of Multivalent Salts—Calcium and Aluminum on the Flocculation of Kaolin Suspension with Anionic Polyacrylamide. *Journal of Colloid and Interface Science* **1994**, 164, (1), 229-237.

[85] Zeng, H.; Maeda, N.; Chen, N.; Tirrell, M.; Israelachvili, J., Adhesion and Friction of Polystyrene Surfaces around Tg. *Macromolecules* **2006**, 39, (6), 2350-2363.

[86] Zeng, H.; Tirrell, M.; Israelachvili, J., Limit Cycles in Dynamic Adhesion and Friction Processes: A Discussion. *The Journal of Adhesion* **2006**, 82, (9), 933-943.

[87] Kosmulski, M., *Chemical Properties of Material Surfaces*. Taylor & Francis: **2001**.

[88] Baerns, M., *Basic Principles in Applied Catalysis*. Springer: **2004**.

[89] Kitchener, J. A., Flocculation in Mineral Processing. In *The Scientific Basis of Flocculation*, Ives, K., Ed. Springer Netherlands: **1978**; Vol. 27, pp 283-328.

[90] Allen, E. W., Process water treatment in Canada's oil sands industry: II. A review of emerging technologies. *Journal of Environmental Engineering and Science* **2008**, 7, (5), 499-524.

[91] Mpofu, P.; Addai-Mensah, J.; Ralston, J., Investigation of the effect of polymer structure type on flocculation, rheology and dewatering behaviour of kaolinite dispersions. *International journal of mineral processing* **2003**, 71, (1-4), 247-268.

- [92] Mpofu, P.; Addai-Mensah, J.; Ralston, J., Flocculation and dewatering behaviour of smectite dispersions: effect of polymer structure type. *Minerals Engineering* **2004**, 17, (3), 411-423.
- [93] Lindquist, G. M.; Stratton, R. A., The role of polyelectrolyte charge density and molecular weight on the adsorption and flocculation of colloidal silica with polyethylenimine. *Journal of Colloid and Interface Science* **1976**, 55, (1), 45-59.
- [94] Zhu, X.; Tang, F.; Suzuki, T. S.; Sakka, Y., Role of the Initial Degree of Ionization of Polyethylenimine in the Dispersion of Silicon Carbide Nanoparticles. *Journal of the American Ceramic Society* **2003**, 86, (1), 189-191.
- [95] Tadros, T. F., Adsorption of polyvinyl alcohol on silica at various pH values and its effect on the flocculation of the dispersion. *Journal of Colloid and Interface Science* **1978**, 64, (1), 36-47.
- [96] Stewart, G. G.; Goring, T. E., Effect of some monovalent and divalent metal ions on the flocculation of brewers yeast strains. *Journal of the Institute of Brewing* **1976**, 82, (6), 341-342.
- [97] Denoyel, R.; Durand, G.; Lafuma, F.; Audebert, R., Adsorption of cationic polyelectrolytes onto montmorillonite and silica: Microcalorimetric study of their conformation. *Journal of Colloid and Interface Science* **1990**, 139, (1), 281-290.
- [98] Ravi Kumar, M. N. V., A review of chitin and chitosan applications. *Reactive and Functional Polymers* **2000**, 46, (1), 1-27.
- [99] Xu, J.; McCarthy, S. P.; Gross, R. A.; Kaplan, D. L., Chitosan Film Acylation and Effects on Biodegradability. *Macromolecules* **1996**, 29, (10), 3436-3440.

- [100] Kean, T.; Thanou, M., Biodegradation, biodistribution and toxicity of chitosan. *Advanced Drug Delivery Reviews* **2010**, 62, (1), 3-11.
- [101] Wan Ngah, W. S.; Teong, L. C.; Hanafiah, M. A. K. M., Adsorption of dyes and heavy metal ions by chitosan composites: A review. *Carbohydrate Polymers* **2011**, 83, (4), 1446-1456.
- [102] Chi, F.; Cheng, W., Use of Chitosan as Coagulant to Treat Wastewater from Milk Processing Plant. *Journal of Polymers and the Environment* **2006**, 14, (4), 411-417.
- [103] Strand, S. P.; Vandvik, M. S.; Vårum, K. M.; Østgaard, K., Screening of Chitosans and Conditions for Bacterial Flocculation. *Biomacromolecules* **2000**, 2, (1), 126-133.
- [104] Xie, W.; Xu, P.; Wang, W.; Liu, Q., Preparation and antibacterial activity of a water-soluble chitosan derivative. *Carbohydrate Polymers* **2002**, 50, (1), 35-40.
- [105] Ahmad, A. L.; Sumathi, S.; Hameed, B. H., Residual oil and suspended solid removal using natural adsorbents chitosan, bentonite and activated carbon: A comparative study. *Chemical Engineering Journal* **2005**, 108, (1-2), 179-185.
- [106] Meyssami, B.; Kasaeian, A. B., Use of coagulants in treatment of olive oil wastewater model solutions by induced air flotation. *Bioresource Technology* **2005**, 96, (3), 303-307.
- [107] Rizzo, L.; Di Gennaro, A.; Gallo, M.; Belgiorno, V., Coagulation/chlorination of surface water: A comparison between chitosan and metal salts. *Separation and Purification Technology* **2008**, 62, (1), 79-85.
- [108] Kurita, K., Chitin and Chitosan: Functional Biopolymers from Marine Crustaceans. *Marine Biotechnology* **2006**, 8, (3), 203-226.

- [109] Laue, C.; Hunkeler, D., Chitosan-graft-acrylamide polyelectrolytes: Synthesis, flocculation, and modeling. *Journal of Applied Polymer Science* **2006**, 102, (1), 885-896.
- [110] Ali, S. K. A.; Singh, R. P., An investigation of the flocculation characteristics of polyacrylamide-grafted chitosan. *Journal of Applied Polymer Science* **2009**, 114, (4), 2410-2414.
- [111] Wang, J.-P.; Chen, Y.-Z.; Zhang, S.-J.; Yu, H.-Q., A chitosan-based flocculant prepared with gamma-irradiation-induced grafting. *Bioresource Technology* **2008**, 99, (9), 3397-3402.
- [112] Lu, Y.; Shang, Y.; Huang, X.; Chen, A.; Yang, Z.; Jiang, Y.; Cai, J.; Gu, W.; Qian, X.; Yang, H.; Cheng, R., Preparation of Strong Cationic Chitosan-graft-Polyacrylamide Flocculants and Their Flocculating Properties. *Industrial & Engineering Chemistry Research* **2011**, 50, (12), 7141-7149.
- [113] Ji, Y. Fundamental Understanding of the Flocculation of Mineral Tailings in High Salinity Water. University of Alberta, **2013**.
- [114] Binazadeh, M.; Zeng, H.; Unsworth, L. D., Effect of peptide secondary structure on adsorption and adsorbed film properties on end-grafted polyethylene oxide layers. *Acta Biomaterialia* **2014**, 10, (1), 56-66.
- [115] Faghihnejad, A.; Zeng, H., Hydrophobic interactions between polymer surfaces: using polystyrene as a model system. *Soft Matter* **2012**, 8, (9), 2746-2759.
- [116] Zhang, L.; Zeng, H.; Liu, Q., Probing Molecular and Surface Interactions of Comb-Type Polymer Polystyrene-graft-poly(ethylene oxide) (PS-g-PEO) with an SFA. *The Journal of Physical Chemistry C* **2012**, 116, (33), 17554-17562.

- [117] Joshi, J. M.; Sinha, V. K., Ceric ammonium nitrate induced grafting of polyacrylamide onto carboxymethyl chitosan. *Carbohydrate Polymers* **2007**, 67, (3), 427-435.
- [118] Renault, F.; Sancey, B.; Badot, P. M.; Crini, G., Chitosan for coagulation/flocculation processes – An eco-friendly approach. *European Polymer Journal* **2009**, 45, (5), 1337-1348.
- [119] Pelton, R. H.; Allen, L. H., The effects of some electrolytes on flocculation with a cationic polyacrylamide. *Colloid and Polymer Science* **1983**, 261, (6), 485-492.
- [120] Shubin, V., Adsorption of Cationic Polymer onto Negatively Charged Surfaces in the Presence of Anionic Surfactant. *Langmuir* **1994**, 10, (4), 1093-1100.